Petroleum Science 23 (2026) 1860–1889

Contents lists available at ScienceDirect

Petroleum Science

journal homepage: www.keaipublishing.com/en/journals/petroleum-science

Original Paper

Finite-difference heterogeneous multiscale method for elastic Helmholtz equation in isotropic media

Wei Jiang [a,b], Xue-Hua Chen [a,b,*], Cong Wang [b]

[a] *State Key Laboratory of Oil & Gas Reservoir Geology and Exploitation, Chengdu University of Technology, Chengdu, 610059, Sichuan, China*
[b] *Key Laboratory of Earth Exploration & Information Techniques of Ministry of Education, Chengdu University of Technology, Chengdu, 610059, Sichuan, China*

ARTICLE INFO

Article history:
Received 16 June 2025
Received in revised form
20 October 2025
Accepted 15 December 2025
Available online 18 December 2025

Edited by Meng-Jiao Zhou

Keywords:
Elastic Helmholtz equation
Finite-difference
Heterogeneous multiscale method
Isotropic media

ABSTRACT

The elastic Helmholtz equation is capable of readily simulating attenuation and dispersion behaviors of the elastic wave and performing full-wavefield modeling in wave-equation-based elastic inversions and migrations. However, solving the elastic Helmholtz equation using a finite-difference frequency-domain (FDFD) method is computationally prohibitive especially in heterogeneous media with fine-scale heterogeneities. The FDFD method usually leads to a large discrete linear system of the elastic Helmholtz equation. We develop a multiscale method of FDFD to solve the elastic Helmholtz equation in isotropic media based on the general framework of heterogeneous multiscale method (HMM). The HMM framework decomposes the elastic Helmholtz problem into a series of microscale problems and a macroscale problem. The idea of multiscale basis functions is introduced to decouple the coupled microscale and macroscale problems and to capture fine-scale heterogeneity in medium properties. A reconstruction-based downscaling coupling and a flux-based upscaling coupling are used to convey the fine-scale medium heterogeneity to a coarse scale. The dimension of the resulting linear system is much smaller than those of linear systems generated with the conventional FDFD methods. We use a homogeneous model and a heterogeneous model to investigate the effects of the size of local sampling domains and the coarse-element number per S-wave wavelength on the accuracy of our new method, and employ two highly heterogeneous models to demonstrate the superiority in terms of the efficiency and memory consumption of our method based on the optimal local sampling-domain size and stable coarse-mesh discretization. The results demonstrate that our new method can approximate the fine-scale reference FDFD solutions with a significant decrease in computational complexity.

1. Introduction

Seismic wave modeling relates geological structures to seismic responses and thus is a powerful tool for wave propagation investigation and wave-modeling-based inversions and migrations (e.g., Köhn et al., 2015; Zhou et al., 2022; Wu et al., 2023; Chen et al., 2024). The essence of seismic wave modeling is to solve the time-domain wave equation or its frequency-domain counterpart. Time-domain methods (e.g., He et al., 2023; Xu and Liu, 2024) produce straightforward wavefield solutions, whereas frequency-domain methods (e.g., Min et al., 2000; Chen and Cao, 2016) have advantages on the attenuation, dispersion, and multi-shot simulations as well as the parallelization for multiple frequency components (Gosselin-Cliche and Giroux, 2014; Fan et al., 2018). Among these methods, finite-difference (FD) methods based on the structured mesh (e.g., Pratt, 1990; Štekl and Pratt, 1998; Min et al., 2000; Chen and Cao, 2016; Yang and Mao, 2017) and finite-element (FE) methods based on the unstructured mesh (e.g., Thompson and Pinsky, 1995; El Kacimi and Laghrouche, 2009; Zhao et al., 2017) receive much attention due to their well-known trade-off between the accuracy and efficiency (Fu et al., 2019). However, these methods encounter a major challenge when they conduct wave modeling in highly heterogeneous media. In these media, a sufficiently fine mesh discretization is

---

* Corresponding author.
E-mail address: chen_xuehua@163.com (X.-H. Chen).
Peer review under the responsibility of China University of Petroleum (Beijing).

https://doi.org/10.1016/j.petsci.2025.12.025

necessary to capture fine-scale heterogeneities, and eventually leads to huge discrete linear systems with millions or even billions of degrees of freedom in the two- and three-dimensional scenarios from the Helmholtz equation. Due to more displacement components in the elastic case than that in the acoustic case, the issue concerning the computational cost of solving the elastic Helmholtz equation is relatively more severe.

The limitation of the computational cost attributes mainly to the linear system solver. The main drawbacks of existing dominant direct and iterative linear system solvers are the high memory requirement related to the lower–upper (LU) factorization and low efficiency associated with the convergence rate, respectively (Gosselin-Cliche and Giroux, 2014; Li et al., 2015). Several methods and techniques, such as the multifrontal method (e.g., Wang et al., 2010, 2011, 2012), the block low-rank technique (e.g., Amestoy et al., 2015), and the hierarchically semi-separable technique (e.g., Xia et al., 2010), have been explored to achieve an improvement in the memory consumption of the direct solvers. These improved direct solvers depend on the impedance matrix structure in the linear system and complicated parallelization strategies to alleviate the memory burden (Fu and Gao, 2017). Whereas, efforts of improving the iterative solvers primarily focus on the preconditioners whose role is to accelerate the convergence of an iterative algorithm. Dominant preconditioners include multigrid-based preconditioners (e.g., Erlangga et al., 2004, 2006) and sweeping preconditioners (e.g., Engquist and Ying, 2011; Poulson et al., 2013). The multigrid method is still the leading approach for iteratively solving the Helmholtz equation (Fu and Gao, 2017). In addition, the parallel strategy is introduced by some studies to achieve a parallelization of preconditioners or iterative solvers for further improvement in the efficiency (e.g., Poulson et al., 2013; Li et al., 2015).

Another adverse factor associated with the high computational costs is high degrees of freedom. The adaptive methods exploit a space-adaptive grid scheme to generate linear systems with a low degree of freedom. The space-adaptive methods use meshes with different sizes to discretize model zones with different velocity variations (Fan et al., 2018), which avoids redundant grids in the model zones with small velocity contrasts and high velocity and thus decreases degrees of freedom of the linear systems. Nevertheless, highly complex heterogeneous media fail effective applications of the space-adaptive methods. Barring the adaptive methods, the numerical homogenization methods (e.g., Capdeville and Marigo, 2007; Gao et al., 2015) provide an alternative approach to achieve a reduction of the computational cost. These numerical homogenization methods upscale the fine-scale heterogeneous media to produce the coarse-scale effective media. Wave modeling is finally performed using the effective model on the coarse level instead of the original model on the fine level. However, a condition of long-wavelength assumption is required for the numerical homogenization methods.

Multiscale methods provide another important means to reduce the computational complexity of solving the Helmholtz equation. The goal of the multiscale methods is to construct reduced discrete linear systems from the Helmholtz equation without loss of the fine-scale medium heterogeneity impact. The relevant multiscale methods in wave propagation investigation mainly include the multiscale finite-element method (MsFEM) (Hou and Wu, 1997) and heterogeneous multiscale method (HMM) (E and Engquist, 2003). Some researchers (Efendiev et al., 2013; Gao et al., 2018; Fu et al., 2019; Zhang et al., 2010a, 2010b) have further developed the improved versions of MsFEM, such as the generalized, high-order, and extended MsFEMs. The philosophy of these MsFEMs of different versions is to perform a fine-to-coarse projection of discrete Helmholtz equation systems before solving them. By contrast, the HMM is only a general framework with which a specific multiscale algorithm can be designed, and can be combined with the FD and FE methods (Chen, 2009). However, most of HMM-based multiscale methods for transient (parabolic) and steady (elliptic) problems use the FE methods as microscale and macroscale solvers. Because the FD methods are widely applied, Abdulle and E (2003) proposed a FD-HMM for the transient problems. Later, the FD-HMM has been applied to solve the transient wave equation in the time domain (Engquist et al., 2011; Arjmand and Runborg, 2017), and extended to develop an FDFD-HMM for the steady acoustic Helmholtz equation in the frequency domain (Jiang et al., 2021, 2022).

In this paper, we further develop an evolutionary elastic version of FDFD-HMM for the elastic Helmholtz equation with coupled displacement components in isotropic media. Different from the acoustic case, it is necessary to consider the effect of the coupling between different displacement components on the reconstruction and flux estimation in the elastic case. Following existing HMM-based multiscale methods (e.g., Abdulle and E, 2003; Chen and Ren, 2008; Chen, 2009; Engquist et al., 2011; Arjmand and Runborg, 2017), the acoustic FDFD-HMM (Jiang et al., 2021, 2022) employs a linear medium-independent reconstruction operator. Nevertheless, this reconstruction operator is inaccurate in the elastic case. We design a medium-dependent reconstruction operator to improve the accuracy in the elastic FDFD-HMM. To further improve the accuracy in the elastic case, we develop an eight-flux-based 21-point FD stencil to discrete the macroscale problem for constructing the reduced coarse-scale linear system due to the insufficient accuracy of a 9-point stencil used in the existing HMM-based FD and FDFD methods (e.g., Abdulle and E, 2003; Chen and Ren, 2008; Chen, 2009; Arjmand and Runborg, 2017; Jiang et al., 2021, 2022).

2. Elastic Helmholtz equation

The elastic Helmholtz equation is formulated as (Fu et al., 2019)

$$\begin{aligned}&\nabla\cdot\boldsymbol{\sigma}(\mathbf{U})+\rho\omega^2\mathbf{U}=-\mathbf{F},\\&\boldsymbol{\sigma}(\mathbf{U})=\mathbf{C}:\mathbf{e}(\mathbf{U}),\\&\mathbf{e}(\mathbf{U})=\frac{1}{2}\left[\nabla\mathbf{U}+(\nabla\mathbf{U})^{\mathrm{T}}\right],\end{aligned}\tag{1}$$

where $\boldsymbol{\sigma}(\mathbf{U})=\boldsymbol{\sigma}(\mathbf{x},\omega)$ is the second-order stress tensor, $\mathbf{e}(\mathbf{U})=\mathbf{e}(\mathbf{x},\omega)$ is the second-order strain tensor, $\mathbf{C}=\mathbf{C}(\mathbf{x},\omega)$ is the fourth-order stiffness tensor, $\mathbf{U}=\mathbf{U}(\mathbf{x},\omega)$ is the displacement vector, $\rho=\rho(\mathbf{x})$ is the medium density, $\mathbf{F}=\mathbf{F}(\mathbf{x},\omega)$ is the external force vector, $\mathbf{x}$ denotes the Cartesian coordinate, and $\omega=2\pi f$ represents the angular frequency of the frequency f.

With the Voigt notation (Mavko et al., 2009), the stiffness tensor of fourth order in isotropic media is abbreviated to a second-order form:

$$\mathbf{C}=\begin{pmatrix}C_{11}&C_{12}&C_{13}&&&\\C_{12}&C_{22}&C_{23}&&&\\C_{13}&C_{23}&C_{33}&&&\\&&&C_{44}&&\\&&&&C_{55}&\\&&&&&C_{66}\end{pmatrix},\tag{2}$$

with

$$C_{11}=C_{22}=C_{33},C_{44}=C_{55}=C_{66},C_{12}=C_{13}=C_{23}.\tag{3}$$

We only consider a two-dimensional scenario in the x-z plane in this paper. In this case, the stiffness tensor in Eq. (2) is reduced to

$$\mathbf{C}=\begin{pmatrix} C_{11} & C_{13} & 0 \\ C_{13} & C_{33} & 0 \\ 0 & 0 & C_{55} \end{pmatrix}, \tag{4}$$

wherein nonzero entries are related to the velocities and density by

$$C_{11}=C_{33}=\rho v_{\mathrm{p}}^2, C_{13}=\rho\left(v_{\mathrm{p}}^2-2v_{\mathrm{s}}^2\right), C_{55}=\rho v_{\mathrm{s}}^2, \tag{5}$$

in which v_{p} and v_{s} are the P- and S-wave velocities, respectively.

Substituting Eq. (4) into Eq. (1) yields an explicit formulation of the elastic Helmholtz equation in two-dimensional heterogeneous isotropic media (Pratt, 1990; Štekl and Pratt, 1998):

$$\begin{cases} \dfrac{\partial}{\partial x}\left(C_{11}\dfrac{\partial U_x}{\partial x}+C_{13}\dfrac{\partial U_z}{\partial z}\right)+\dfrac{\partial}{\partial z}\left(C_{55}\dfrac{\partial U_x}{\partial z}+C_{55}\dfrac{\partial U_z}{\partial x}\right)+\rho\omega^2 U_x=-F_x, \\ \dfrac{\partial}{\partial x}\left(C_{55}\dfrac{\partial U_x}{\partial z}+C_{55}\dfrac{\partial U_z}{\partial x}\right)+\dfrac{\partial}{\partial z}\left(C_{13}\dfrac{\partial U_x}{\partial x}+C_{33}\dfrac{\partial U_z}{\partial z}\right)+\rho\omega^2 U_z=-F_z, \end{cases} \tag{6}$$

where $(U_x, U_z)^{\mathrm{T}}=\mathbf{U}$, $(F_x, F_z)^{\mathrm{T}}=\mathbf{F}$, and $(x, z)=\mathbf{x}$.

3. Finite-difference heterogeneous multiscale method in the frequency domain

In the following theory development, we focus on formulating our FDFD-HMM for the elastic Helmholtz equation in the two-dimensional isotropic media.

The theory development includes four parts: (1) the numerical construction of multiscale basis functions from local elastic Helmholtz problems; (2) the analytical formulation of a medium-dependent reconstruction operator for a downscaling coupling of the microscale and macroscale problems; (3) the coupled semi-analytical solutions of the microscale problems; (4) the FD assembly of a coarse-scale linear system from the upscaling-flux-based macroscale problem (Fig. 1). A unique composite mesh with multiscale partitioning is designed to accommodate this algorithm framework before the elaboration of these four parts.

3.1. Multiscale composite mesh

To accommodate the HMM framework, the computational domain is partitioned with a multiscale composite mesh that includes a coarse mesh for discretizing the macroscale problem, a global fine mesh for medium discretization, local sampling domains for the missing macroscale flux estimation, and two local fine meshes for discretizing the microscale problems.

We use a coarse mesh indicated by $\mathrm{Q_H}$ that contains $N_x^{\mathrm{H}}\times N_z^{\mathrm{H}}$ coarse elements to partition the computational domain, where N_x^{H} and N_z^{H} are the x- and z-direction numbers of coarse elements, respectively. The coarse elements are supports of the coarse-scale displacement and force vectors in the macroscale problem, namely, these coarse-scale quantities are defined at the center points of their supports. The neighboring four coarse-element center points constitute four vertices of a rectangular region called H-cell (I^{H} in Fig. 2). We specify an H-cell by its center point. Unlike the acoustic FDFD-HMM (Jiang et al., 2021, 2022), this elasticity extension designs additional H-cells to capture the fine-scale heterogeneity outside the local sampling domains (I^{ε} in Fig. 2) for constructing the medium-dependent reconstruction operator.

Each coarse element in $\mathrm{Q_H}$ is further partitioned with finer cells that need to be sufficiently fine to characterize the fine-scale heterogeneities in isotropic media. The fine cell numbers in the x and z directions in a coarse element represent coarsening ratios r_x and r_z in the corresponding directions, respectively. All fine cells in $\mathrm{Q_H}$ compose a global fine mesh indicated by $\mathrm{Q_h}$ with $r_xN_x^{\mathrm{H}}\times r_zN_z^{\mathrm{H}}$ fine elements. The fine-scale medium properties including the stiffness tensor and density are defined at the center points of these fine elements. In addition, as supports of the local microscale problems, each H-cell is similarly partitioned by a local fine mesh $\mathrm{Q_h^H}$ staggered with $\mathrm{Q_h}$. Whereas, we define the fine-scale

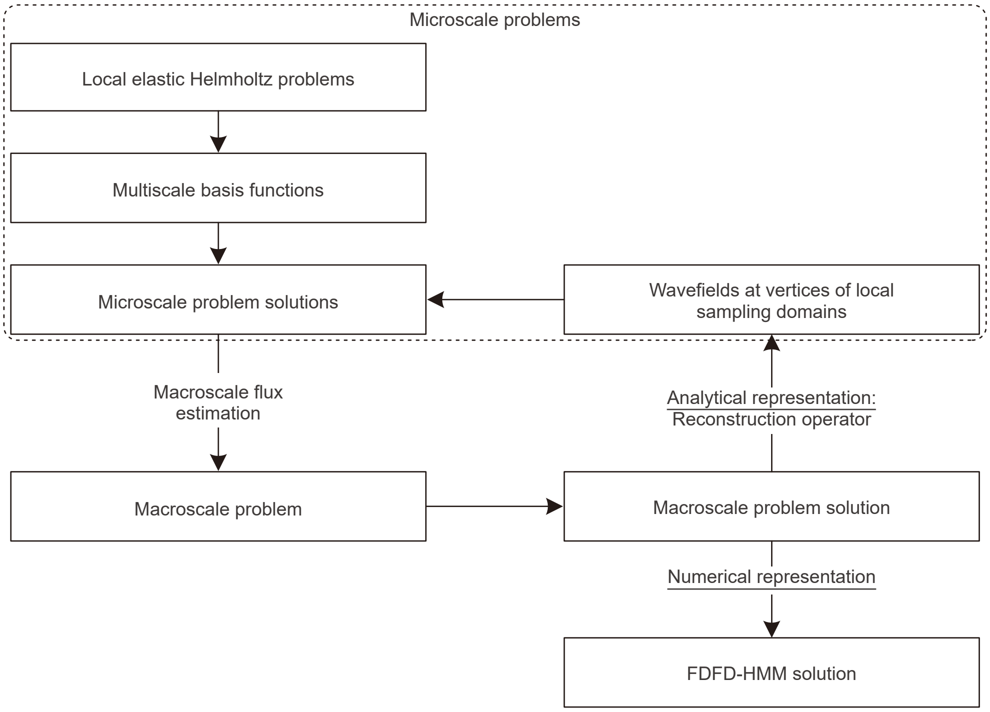

Fig. 1. Framework of FDFD-HMM.

displacement and discrete multiscale basis functions at the vertices instead of center points of fine elements in $\mathrm{Q}_{\mathrm{h}}^{\mathrm{H}}$ to accommodate the definition of coarse-scale displacements.

The local sampling domains are indispensable for fine-scale heterogeneity capture in the HMM framework. For simplicity, we name these local sampling domains as ε-cells. They are centered at the points $(x_{i\pm1/2}, z_j)$ and $(x_i, z_{j\pm1/2})$ ($I^{\varepsilon}_{i\pm1/2,j}$ and $I^{\varepsilon}_{i,j\pm1/2}$ in Fig. 2). Similarly, we specify an ε-cell by its center point. These ε-cells are used as supports for both the local microscale problems and macroscale flux estimation. Each ε-cell is partitioned into a local fine mesh $\mathrm{Q}_{\mathrm{h}}^{\varepsilon}$. The fine elements in $\mathrm{Q}_{\mathrm{h}}^{\varepsilon}$ are supports of the fine-scale displacement vector and discrete multiscale basis functions in the local microscale problems, leading to that these fine-scale parameters are defined at the center points of their supports as in Q_{H}. Moreover, additional ε-cells are necessary to support macroscale fluxes of the mass acceleration term $\rho\omega^2\mathbf{U}$ in Eq. (1). For simplicity, we employ the coarse elements, that is $I_{i,j}$, in Q_{H} to act as these supports.

3.2. Microscale problems

3.2.1. Multiscale basis functions

The multiscale basis functions are vital to our FDFD-HMM because they can decouple the coupled microscale and macroscale problems to simplify the procedure of solving the microscale problems. Another two roles of these multiscale basis functions are to capture the effect of fine-scale medium heterogeneities and to couple the wavefields at two different scales. We construct the multiscale basis functions over the H- and ε-cells.

Because the elastic Helmholtz equation describes a vector problem, the approach that constructs oscillating boundary conditions by decomposing the elastic Helmholtz equation into unidimensional formulations is inapplicable. We thus first use the oversampling technique (Zhang et al., 2010a, 2010b) to generate the oscillating boundary conditions of an original cell from the linear boundary conditions of an oversampled cell.

For each displacement component, we solve the following local elastic Helmholtz problem over each of the oversampled H- and ε-cells ($I^{\mathrm{H}+}$ and $I^{\varepsilon+}$ in Fig. 3) to construct temporary basis functions:

$$\nabla\cdot\boldsymbol{\sigma}\left(\boldsymbol{\psi}_m^+\right)+\rho\omega^2\boldsymbol{\psi}_m^+=0,\ \text{in}\ I^+, \tag{7}$$

where $\boldsymbol{\psi}_m^+=\boldsymbol{\psi}_m^+(\mathbf{x},\omega)=\left(\psi_{x,m}^+,\psi_{z,m}^+\right)^{\mathrm{T}}$ with $m=1,\ldots,8$ are the temporary basis functions to be solved, and I^+ represents one of the oversampled H- and ε-cells. The number of the basis functions for an oversampled cell is determined by $d2^d$, where d denotes the dimensionality (namely the number of displacement components) and 2^d represents the number of coarse-scale boundary nodes. There are $d=2$ displacement components in the two-dimensional case, and an oversampled cell has $2^d=4$ coarse-scale boundary nodes (black-filled squares labeled by h' with $h=1,\ldots,4$ in Fig. 4). To solve the temporary basis functions $\boldsymbol{\psi}_m^+$ associated with the x-component displacement for $m=1,\ldots,4$ and corresponding to the z-component displacement for $m=5,\ldots,8$, we assign the boundary conditions as follows:

$$\boldsymbol{\psi}_m^+=\begin{cases}\left(\mathrm{G}_m,0\right)^{\mathrm{T}},\text{on }\partial I^+, & \text{for } m=1,\cdots,4,\\ \left(0,\mathrm{G}_{m-4}\right)^{\mathrm{T}},\text{on }\partial I^+, & \text{for } m=5,\cdots,8,\end{cases} \tag{8}$$

where G_m represents the linear boundary condition corresponding to the mth coarse-scale boundary node on I^+, and ∂I^+ denotes the boundary of I^+. In detail, G_m is determined by $\mathrm{G}_m\left(\mathbf{x}_h^+\right)=\delta_{mh}$ with $m, h=1, 2, 3, 4$ at the coarse-scale boundary nodes, and varies linearly along the boundaries of I^+, where $\mathbf{x}_h^+$ denotes the hth coarse-scale boundary node on ∂I^+, and δ_{mh} is Kronecker delta function.

Solving the local elastic Helmholtz problem defined in Eqs. (7) and (8), we obtain eight temporary basis functions for each of the oversampled H- and ε-cells. New temporary basis functions $\boldsymbol{\psi}_m$ are then constructed through a linear combination of $\boldsymbol{\psi}_m^+$:

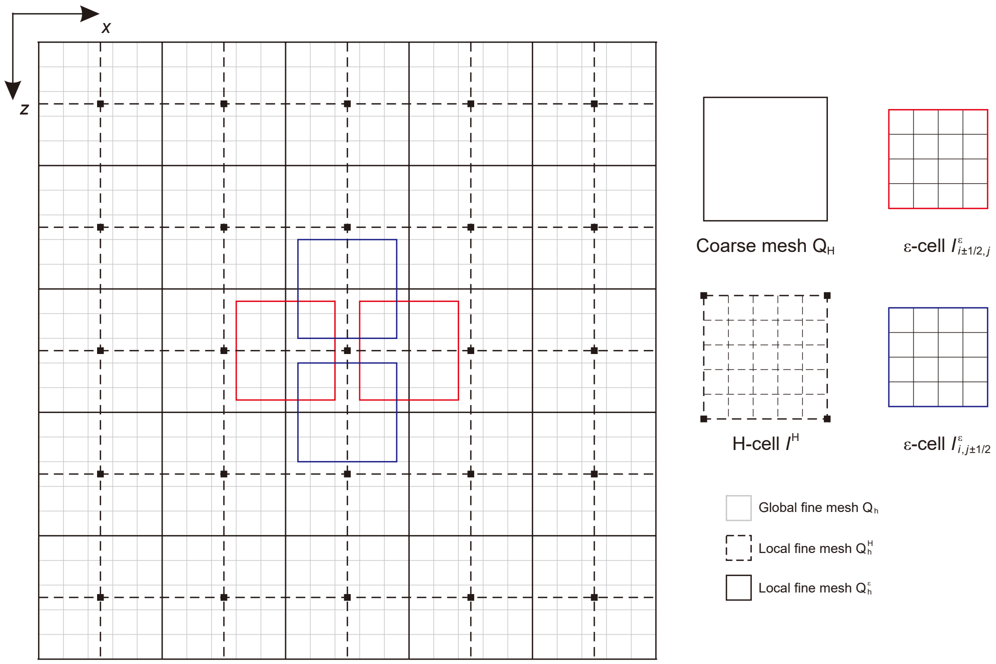

Fig. 2. Illustration of multiscale composite mesh.

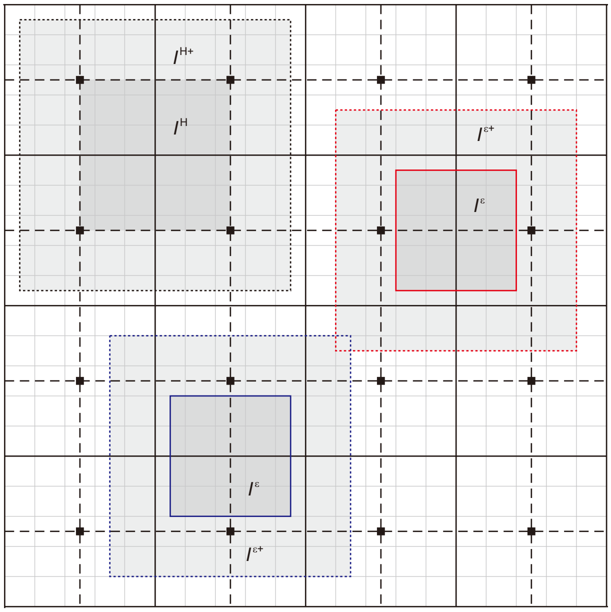

Fig. 3. Illustration of oversampled domains (light-gray-shaded rectangles) of the H-cell and ε-cells (gray-shaded rectangles).

$$\boldsymbol{\psi}_m(\mathbf{x},\omega)=\sum_{n=1}^{8}c_{m,n}\boldsymbol{\psi}_n^{+}(\mathbf{x},\omega), \tag{9}$$

where $c_{m,n}$ with m,n = 1, …, 8 are the combination coefficients determined by $\boldsymbol{\psi}_m(\mathbf{x}_h,\omega)=(\delta_{mh},0)^{\mathrm{T}}$ when m = 1, …, 4 and $\boldsymbol{\psi}_m(\mathbf{x}_h,\omega)=(0,\delta_{(m-4)h})^{\mathrm{T}}$ when $m = 5$, …, 8, in which $\mathbf{x}_h$ with $h = 1$, …, 4 denotes the hth coarse-scale boundary node (black-filled squares labeled by h with $h = 1$, …, 4 in Fig. 4) of an H- or ε-cell. The oversampling technique developed by Zhang et al. (2010a, 2010b) only employs uncoupled components ($\psi_{x,m}^{+}$ with m = 1, …, 4 and $\psi_{z,m}^{+}$ with $m = 5$, …, 8 related to the nonzero x- and z-component displacement boundary conditions, respectively) to determine the new temporary basis functions $\boldsymbol{\psi}_m$, while our method takes the coupled components ($\psi_{x,m}^{+}$ with $m = 5$, …, 8 and $\psi_{z,m}^{+}$ with $m = 1$, …, 4 corresponding to the nonzero z- and x-component displacement boundary conditions, respectively) into account such that all the combination coefficients can be computed simultaneously and the coupling effect of two displacement components is taken into account. Explicitly, the Kronecker delta condition for determining $c_{m,n}$ can be written as a matrix form:

$$\begin{pmatrix} \psi_{x,1}^{+}(\mathbf{x}_1,\omega) & \cdots & \psi_{x,8}^{+}(\mathbf{x}_1,\omega) \\ \vdots & \vdots & \vdots \\ \psi_{x,1}^{+}(\mathbf{x}_4,\omega) & \cdots & \psi_{x,8}^{+}(\mathbf{x}_4,\omega) \\ \psi_{z,1}^{+}(\mathbf{x}_1,\omega) & \cdots & \psi_{z,8}^{+}(\mathbf{x}_1,\omega) \\ \vdots & \vdots & \vdots \\ \psi_{z,1}^{+}(\mathbf{x}_4,\omega) & \cdots & \psi_{z,8}^{+}(\mathbf{x}_4,\omega) \end{pmatrix} \begin{pmatrix} c_{1,1} & \cdots & c_{8,1} \\ \vdots & \vdots & \vdots \\ c_{1,8} & \cdots & c_{8,8} \end{pmatrix} = \begin{pmatrix} 1 & & & & \\ & \ddots & & & \\ & & 1 & & \\ & & & \ddots & \\ & & & & 1 \end{pmatrix}. \tag{10}$$

The temporary basis functions $\boldsymbol{\psi}_m$ with m = 1, …, 8 provide oscillating information on the boundaries of an original H- or ε-cell. With these oscillating values, we next construct the ultimate multiscale basis functions by solving the following elastic Helmholtz problem over each of the H- and ε-cells:

$$\nabla\cdot\boldsymbol{\sigma}(\boldsymbol{\varphi}_m)+\rho\omega^2\boldsymbol{\varphi}_m=\mathbf{0},\ \text{in}\ I, \tag{11}$$

$$\boldsymbol{\varphi}_m=\boldsymbol{\psi}_m|_{\partial I},\ \text{on}\ \partial I, \tag{12}$$

where $\boldsymbol{\varphi}_m=\boldsymbol{\varphi}_m(\mathbf{x},\omega)=(\varphi_{x,m},\varphi_{z,m})^{\mathrm{T}}$ with m = 1, …, 8 are the final multiscale basis functions to be solved, and I represents one of the H- and ε-cells.

The local elastic Helmholtz problems in Eqs. (7), (8), (11) and (12) can be solved numerically by a FDFD method. Due to the limited size and nonzero boundary conditions of the H- and ε-cells, we employ a compact nine-point FDFD method (e.g., Pratt, 1990; Chen and Cao, 2016) to solve these local elastic Helmholtz problems. The obtained multiscale basis functions are medium- and frequency-dependent. Their values contain the effects of fine-scale medium heterogeneities and source frequencies. In consequence, changes in the medium heterogeneity and source frequency require a reconstruction of multiscale basis functions. To give an

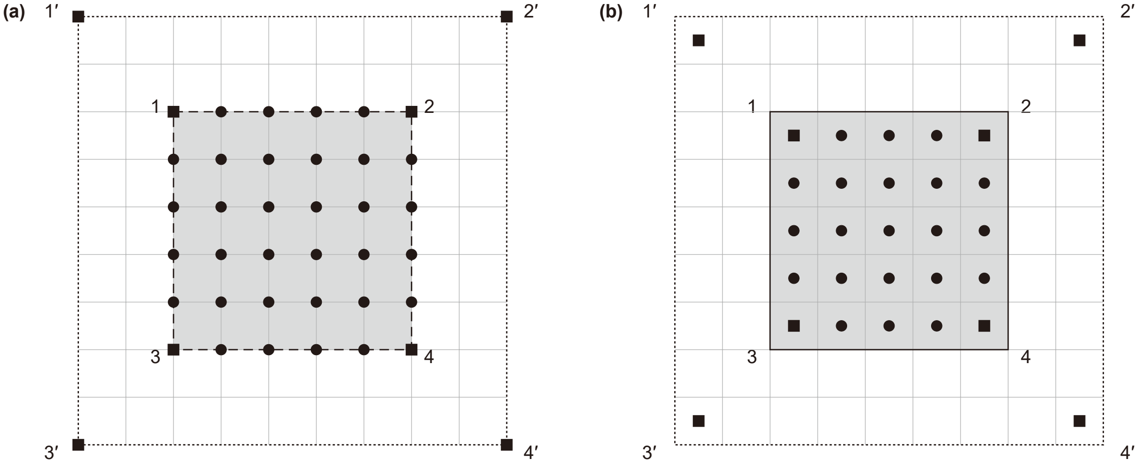

Fig. 4. Coarse- and fine-scale nodes for the **(a)** H-cell and **(b)** ε-cell. The black-filled squares and black dots represent coarse- and fine-scale nodes, respectively.

insight into the shape of constructed multiscale basis functions, we use a heterogeneous cell shown in Fig. 5 to illustrate its multiscale basis functions (Fig. 6). In Fig. 6, the z components of multiscale basis functions for $m = 1, \ldots, 4$ (the second row in Fig. 6(a)) are yielded by the nonzero x-component displacement boundary conditions (Eq. (8)), and the x components of multiscale basis functions for $m = 5, \ldots, 8$ (the first row in Fig. 6(b)) are obtained from the nonzero z-component displacement boundary

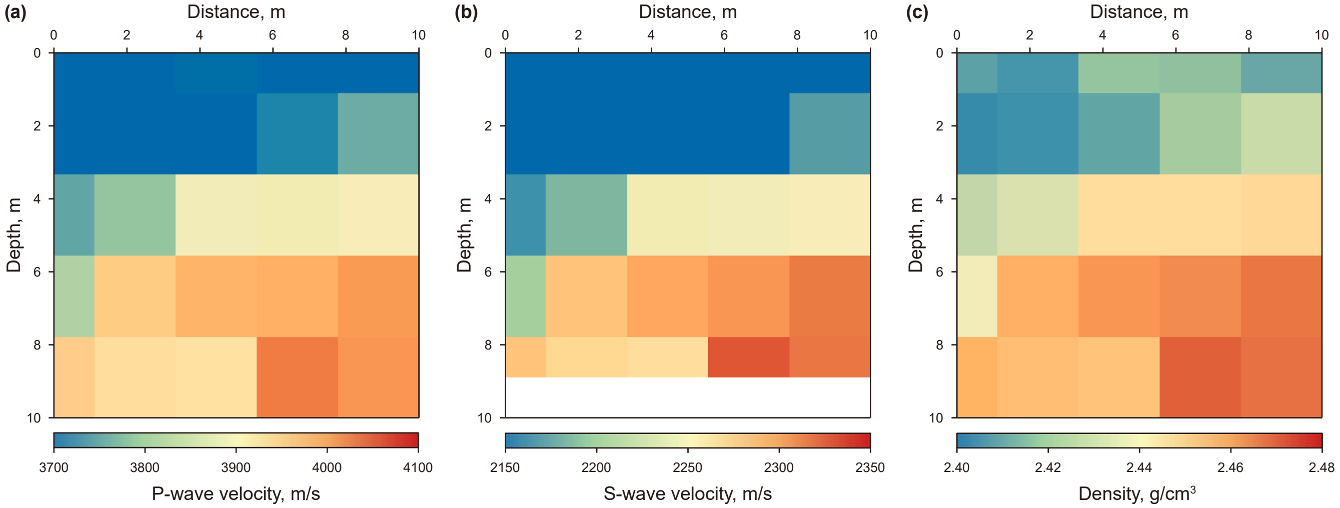

Fig. 5. Example of a cell with fine-scale heterogeneous variations in the **(a)** P-wave velocity, **(b)** S-wave velocity, and **(c)** density.

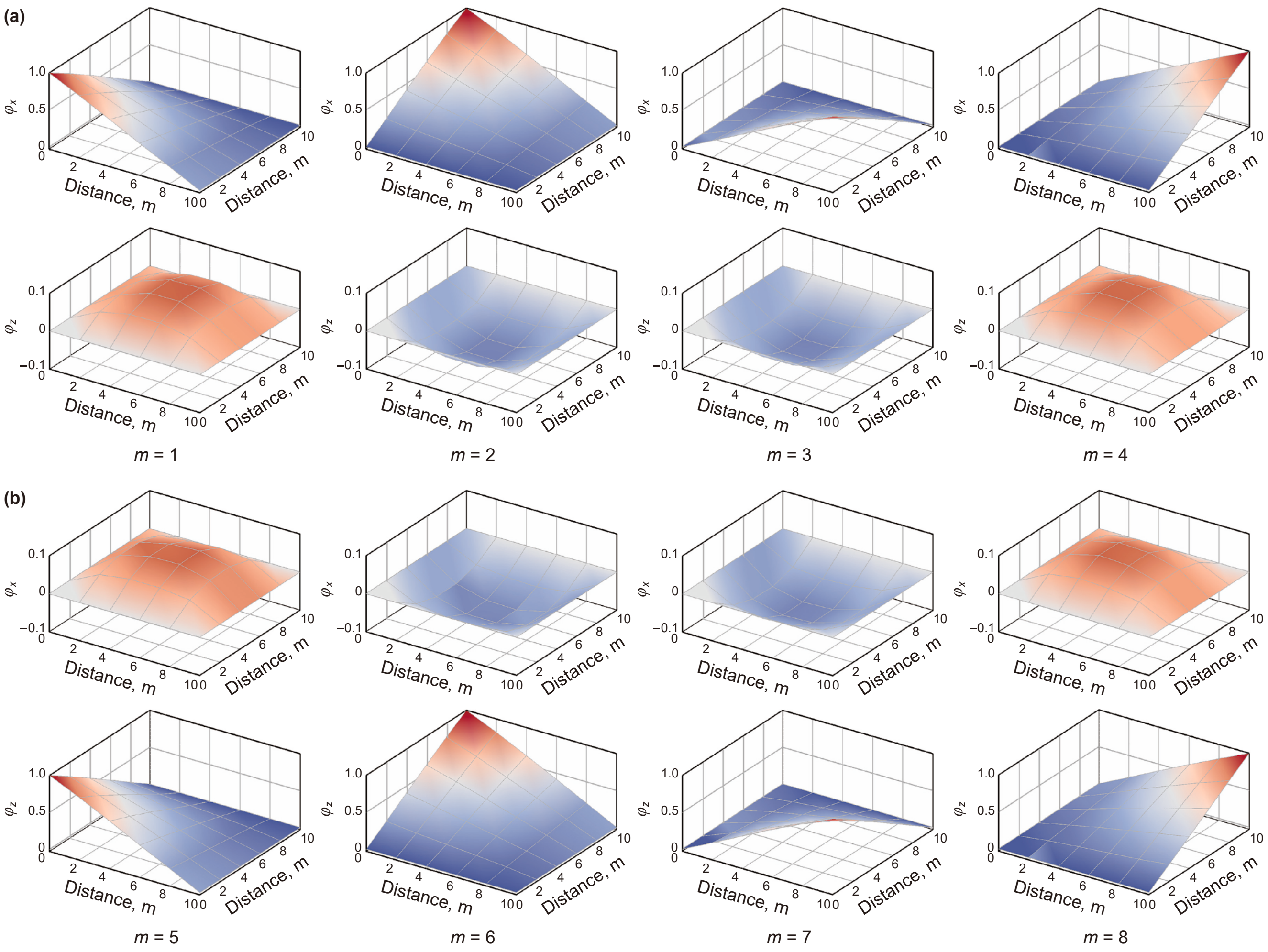

Fig. 6. Multiscale basis functions corresponding to the **(a)** x- and **(b)** z-component displacements at a frequency of 20 Hz. The first and second rows in both **(a)** and **(b)** represent the x and z components of multiscale basis functions, respectively.

conditions (Eq. (8)), which reveal the coupling effect of two displacement components.

3.2.2. Medium-dependent reconstruction operator

The multiscale basis functions within the ε-cell cannot directly couple the fine-scale wavefields on $\mathrm{Q}_{\mathrm{h}}^{\varepsilon}$ with the coarse-scale wavefields on Q_{H}. A reconstruction operator is needed to analytically project the coarse-scale wavefields to the coarse-scale boundary nodes of the ε-cells, that is its vertices. We use the multiscale basis functions for the additional H-cells to capture the fine-scale medium property variations outside the ε-cells, and formulate a medium-dependent reconstruction operator.

We first determine the fine-scale wavefields on $\mathrm{Q}_{\mathrm{h}}^{\mathrm{H}}$ (green dots in Fig. 7) in an H-cell from the coarse-scale wavefields located at the vertices (black-filled squares in Fig. 7) of an H-cell. With the multiscale basis functions constructed over the H-cells, the fine-scale wavefield in an H-cell is given by

$$\boldsymbol{\upsilon}(\boldsymbol{\chi},\omega)=\sum_{m=1}^{4}\boldsymbol{\varphi}_m^{\mathrm{H}}(\boldsymbol{\chi},\omega)U_x(\mathbf{x}_m,\omega)+\sum_{m=1}^{4}\boldsymbol{\varphi}_{m+4}^{\mathrm{H}}(\boldsymbol{\chi},\omega)U_z(\mathbf{x}_m,\omega), \tag{13}$$

where $\boldsymbol{\upsilon}=(\upsilon_x,\upsilon_z)^{\mathrm{T}}$ is the wavefield at the fine-scale node $\boldsymbol{\chi}=(\chi,\gamma)$ of $\mathrm{Q}_{\mathrm{h}}^{\mathrm{H}}$, $(U_x,U_z)^{\mathrm{T}}=\mathbf{U}$ is the macroscale problem wavefield solution at the coarse-scale node $\mathbf{x}_m$ of Q_{H}, and the superscript H of $\boldsymbol{\varphi}_m$ denotes that the multiscale basis function is obtained over an H-cell.

We next use the neighboring fine-scale wavefields $\boldsymbol{\upsilon}$ on $\mathrm{Q}_{\mathrm{h}}^{\mathrm{H}}$ (red and blue dots in Fig. 7) to determine the wavefields $\mathbf{U}'$ located at the vertices (red- and blue-filled squares in Fig. 7) of the ε-cells. Considering the flexibility that the HMM allows the ε-cell size to vary, a bilinear interpolation operator within fine elements of $\mathrm{Q}_{\mathrm{h}}^{\mathrm{H}}$ is used to determine the wavefields $\mathbf{U}'=\left(U_x',U_z'\right)^{\mathrm{T}}$ at the four vertices $\boldsymbol{\xi}_h=\left(\xi^{[h]},\eta^{[h]}\right)$ with $h=1,\ldots,4$ of an ε-cell:

$$\begin{aligned}\mathbf{U}'(\boldsymbol{\xi}_h,\omega)=\mathbf{U}'\left(\xi^{[h]},\eta^{[h]},\omega\right)=&\left(1-\frac{\xi^{[h]}-\chi_1^{[h]}}{\Delta\chi}\right)\left(1-\frac{\eta^{[h]}-\gamma_1^{[h]}}{\Delta\gamma}\right)\\&\boldsymbol{\upsilon}\left(\boldsymbol{\chi}_1^{[h]},\omega\right)+\frac{\xi^{[h]}-\chi_1^{[h]}}{\Delta\chi}\,\frac{\eta^{[h]}-\gamma_1^{[h]}}{\Delta\gamma}\boldsymbol{\upsilon}\left(\boldsymbol{\chi}_4^{[h]},\omega\right)+\frac{\xi^{[h]}-\chi_1^{[h]}}{\Delta\chi}\\&\left(1-\frac{\eta^{[h]}-\gamma_1^{[h]}}{\Delta\gamma}\right)\boldsymbol{\upsilon}\left(\boldsymbol{\chi}_2^{[h]},\omega\right)+\left(1-\frac{\xi^{[h]}-\chi_1^{[h]}}{\Delta\chi}\right)\\&\frac{\eta^{[h]}-\gamma_1^{[h]}}{\Delta\gamma}\boldsymbol{\upsilon}\left(\boldsymbol{\chi}_3^{[h]},\omega\right),\end{aligned} \tag{14}$$

where $\boldsymbol{\chi}_1^{[h]}=\left(\chi_1^{[h]},\gamma_1^{[h]}\right)$, $\boldsymbol{\chi}_2^{[h]}=\left(\chi_2^{[h]},\gamma_2^{[h]}\right)$, $\boldsymbol{\chi}_3^{[h]}=\left(\chi_3^{[h]},\gamma_3^{[h]}\right)$, and $\boldsymbol{\chi}_4^{[h]}=\left(\chi_4^{[h]},\gamma_4^{[h]}\right)$ represent four neighboring fine-scale nodes around the vertex $\boldsymbol{\xi}_h$ with $h=1,\ldots,4$ of an ε-cell, and $\Delta\chi$ and $\Delta\gamma$ are the x- and z-direction sizes of fine elements in $\mathrm{Q}_{\mathrm{h}}^{\mathrm{H}}$, respectively. For each of the vertices $\boldsymbol{\xi}_h$ with $h=1,\ldots,4$ of an ε-cell, the bilinear interpolation is carried out within a fine element, the smallest discrete element in the multiscale discrete space, of $\mathrm{Q}_{\mathrm{h}}^{\mathrm{H}}$ rather than within an H-cell.

According to Eqs. (13) and (14), we finally obtain a reconstruction operator of the wavefield $\mathbf{U}'$ located at the vertices of an ε-cell with respect to the coarse-scale wavefield $\mathbf{U}$:

$$\mathbf{U}'=\mathrm{R}(\mathbf{U}). \tag{15}$$

We do not present a specific formulation of this reconstruction operator $\mathrm{R}(\cdot)$ because it is involved in the final expression of the microscale problem solution $\mathbf{u}$ (see Appendix A). Compared with the medium-independent reconstruction operator that directly interpolate the coarse-scale wavefield $\mathbf{U}$ to yield the ε-cell boundary wavefields (Jiang et al., 2021, 2022), $\mathrm{R}(\cdot)$ based on the multiscale basis functions in Eq. (15) captures the effect of fine-scale medium heterogeneities outside the ε-cells ($I_{i\pm1/2,j\pm1/2}^{\mathrm{H}}-I_{i\pm1/2,j}^{\varepsilon}$ and $I_{i\pm1/2,j\pm1/2}^{\mathrm{H}}-I_{i,j\pm1/2}^{\varepsilon}$ in Fig. 7, where $I_{i\pm1/2,j\pm1/2}^{\mathrm{H}}=I_{i-1/2,j-1/2}^{\mathrm{H}}\cup I_{i+1/2,j-1/2}^{\mathrm{H}}\cup I_{i-1/2,j+1/2}^{\mathrm{H}}\cup I_{i+1/2,j+1/2}^{\mathrm{H}}$, $I_{i\pm1/2,j}^{\varepsilon}=I_{i-1/2,j}^{\varepsilon}\cup I_{i+1/2,j}^{\varepsilon}$, and $I_{i,j\pm1/2}^{\varepsilon}=I_{i,j-1/2}^{\varepsilon}\cup I_{i,j+1/2}^{\varepsilon}$). In addition, the multiscale basis functions involved in $\mathrm{R}(\cdot)$ also contain the coupling effect of two displacement components.

3.2.3. Microscale problem solutions within ε-cells

The ε-cells are the target local domains over which the microscale problem wavefield solutions are obtained for the subsequent estimation of the missing macroscale fluxes. With the reconstructed wavefield $\mathbf{U}'$ and the multiscale basis functions for the ε-cells, the fine-scale wavefield in an ε-cell is given by

$$\mathbf{u}(\boldsymbol{\xi},\omega)=\sum_{m=1}^{4}\boldsymbol{\varphi}_m^{\varepsilon}(\boldsymbol{\xi},\omega)U_x'(\boldsymbol{\xi}_m,\omega)+\sum_{m=1}^{4}\boldsymbol{\varphi}_{m+4}^{\varepsilon}(\boldsymbol{\xi},\omega)U_z'(\boldsymbol{\xi}_m,\omega), \tag{16}$$

where $\mathbf{u}=(u_x,u_z)^{\mathrm{T}}$ is the wavefield at the fine-scale node $\boldsymbol{\xi}=(\xi,\eta)$ of $\mathrm{Q}_{\mathrm{h}}^{\varepsilon}$, the superscript ε of $\boldsymbol{\varphi}_m$ denotes that the multiscale basis function is obtained over an ε-cell.

Substituting the reconstruction operator in Eq. (15) into Eq. (16) yields linear coupling expressions of the microscale problem solution $\mathbf{u}$ with the macroscale problem solution $\mathbf{U}$:

$$\mathbf{u}(\boldsymbol{\xi},\omega)=\begin{cases}\displaystyle\sum_{n=1}^{6}\mathbf{c}_n^{\pm}(\boldsymbol{\xi},\omega)\mathbf{U}(\mathbf{x}_n,\omega), & \text{for } I_{i\pm1/2,j}^{\varepsilon},\\ \displaystyle\sum_{n=1}^{6}\mathbf{d}_n^{\pm}(\boldsymbol{\xi},\omega)\mathbf{U}(\mathbf{x}_n,\omega), & \text{for } I_{i,j\pm1/2}^{\varepsilon},\end{cases} \tag{17}$$

where $\mathbf{c}_n^{\pm}(\boldsymbol{\xi},\omega)$ and $\mathbf{d}_n^{\pm}(\boldsymbol{\xi},\omega)$ with $n=1,\ldots,6$ are the coupling coefficient matrices. For each of the ε-cells, its microscale problem solution is only related to the wavefields at six coarse-scale nodes. See Appendix A for more details on these six coarse-scale wavefields and the coupling coefficient matrices.

3.3. Macroscale problem

Accommodating to the HMM framework (E and Engquist, 2003), the elastic Helmholtz equation in Eq. (1) is reformulated as a flux form:

$$\nabla\cdot\overline{\mathbf{P}}+\omega^2\overline{D}\mathbf{U}=-\mathbf{F}, \tag{18}$$

where $\overline{\mathbf{P}}=\left(\overline{P}_x,\overline{P}_z\right)^{\mathrm{T}}$ and $\overline{D}$ are the macroscale fluxes in the local sampling domains.

We follow the FD-HMM (Abdulle and E, 2003; Engquist et al., 2011) to discretize Eq. (18) with a central difference scheme. Considering the insufficient accuracy of the second-order FD scheme based on four fluxes in the existing FD- and FDFD-HMMs (Abdulle and E, 2003; Chen and Ren, 2008; Arjmand and Runborg, 2017; Jiang et al., 2021, 2022), a fourth-order FD scheme involving eight fluxes is applied to the elastic Helmholtz equation of flux form. The FD approximation of Eq. (18) is

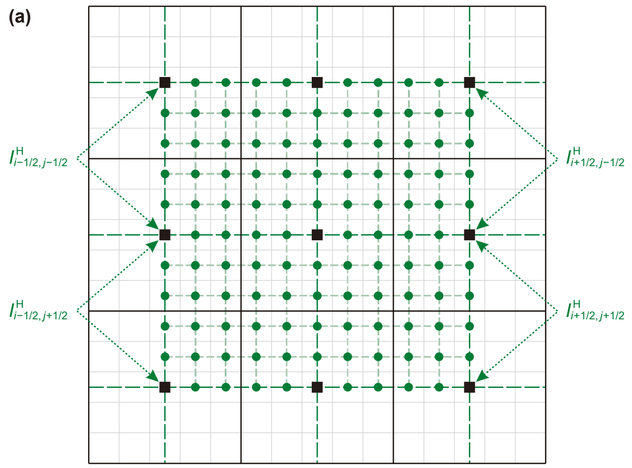

U (■) → υ (●) using multiscale basis functions of H-cells

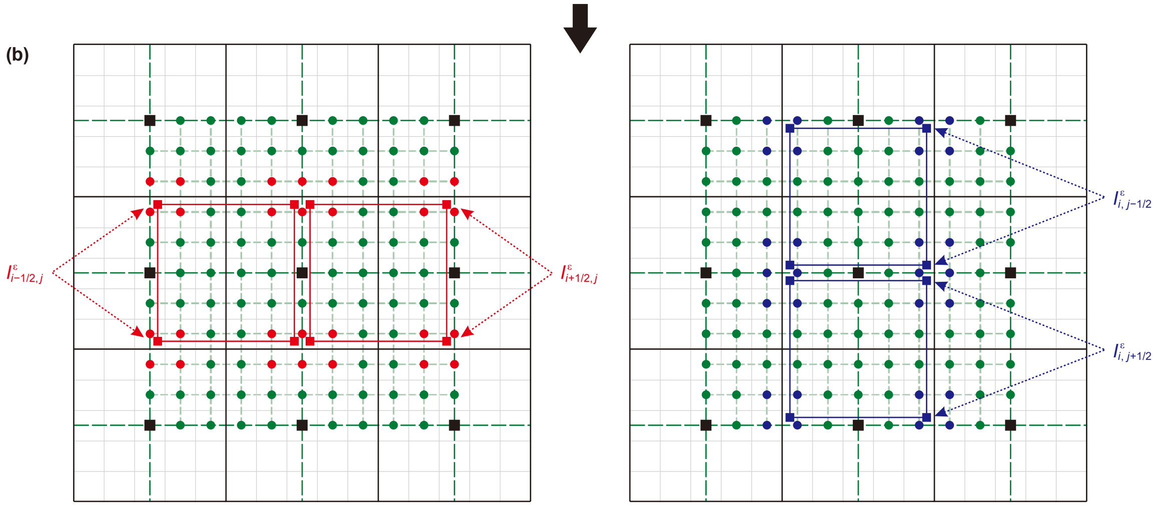

Extracting neighboring υ (● and ●) around ε-cell vertices (■ and ■) from υ (●)

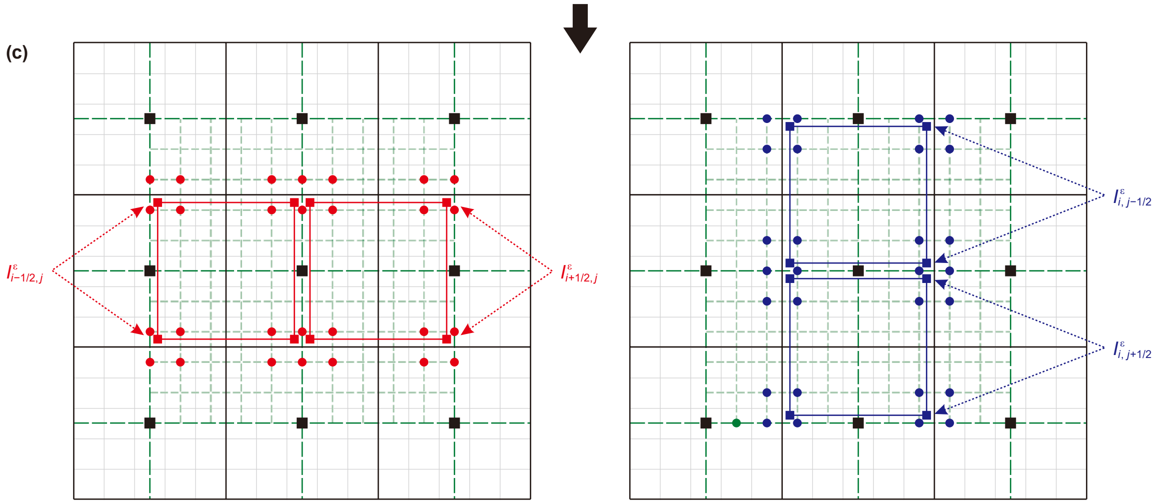

υ (● and ●) → U′ (■ and ■) by a bilinear interpolation

Fig. 7. Illustration of wavefield projection from the coarse-scale nodes (black-filled squares) on Q_H to the vertices (red- and blue-filled squares) of the ε-cells via **(a)** computing fine-scale wavefields (green dots) within the H-cells, **(b)** extracting neighboring fine-scale wavefields (red and blue dots) around the ε-cell vertices, and **(c)** bilinear interpolation to compute wavefields at the ε-cell vertices.

$$\begin{aligned}&\frac{1}{\Delta x}\left[\frac{9}{8}\left(\overline{\mathbf{P}}_{i+1/2,j}-\overline{\mathbf{P}}_{i-1/2,j}\right)-\frac{1}{24}\left(\overline{\mathbf{P}}_{i+3/2,j}-\overline{\mathbf{P}}_{i-3/2,j}\right)\right]\\&+\frac{1}{\Delta z}\left[\frac{9}{8}\left(\overline{\mathbf{P}}_{i,j+1/2}-\overline{\mathbf{P}}_{i,j-1/2}\right)-\frac{1}{24}\left(\overline{\mathbf{P}}_{i,j+3/2}-\overline{\mathbf{P}}_{i,j-3/2}\right)\right]\\&+\omega^2\overline{D}_{i,j}\mathbf{U}_{i,j}=-\mathbf{F}_{i,j},\end{aligned}\tag{19}$$

where 9/8 and −1/24 are the FD coefficients of fourth-order (Levander, 1988; Hustedt et al., 2004). According to the explicit form of the elastic Helmholtz equation in Eq. (6), the macroscale fluxes in Eq. (19) are given by

$$\overline{\mathbf{P}}_{i\pm n/2,j}=\begin{bmatrix}\overline{P}_{x,i\pm n/2,j}\\ \overline{P}_{z,i\pm n/2,j}\end{bmatrix}=\frac{1}{\left|I^{\varepsilon}_{i\pm n/2,j}\right|}\begin{bmatrix}\iint_{I^{\varepsilon}_{i\pm n/2,j}}\left(C_{11}\dfrac{\partial u_x}{\partial x}+C_{13}\dfrac{\partial u_z}{\partial z}\right)\mathrm{d}x\mathrm{d}z\\ \iint_{I^{\varepsilon}_{i\pm n/2,j}}\left(C_{55}\dfrac{\partial u_x}{\partial z}+C_{55}\dfrac{\partial u_z}{\partial x}\right)\mathrm{d}x\mathrm{d}z\end{bmatrix},n=1,3,\tag{20a}$$

$$\overline{\mathbf{P}}_{i,j\pm n/2}=\begin{bmatrix}\overline{P}_{x,i,j\pm n/2}\\ \overline{P}_{z,i,j\pm n/2}\end{bmatrix}=\frac{1}{\left|I^{\varepsilon}_{i,j\pm n/2}\right|}\begin{bmatrix}\iint_{I^{\varepsilon}_{i,j\pm n/2}}\left(C_{55}\dfrac{\partial u_x}{\partial z}+C_{55}\dfrac{\partial u_z}{\partial x}\right)\mathrm{d}x\mathrm{d}z\\ \iint_{I^{\varepsilon}_{i,j\pm n/2}}\left(C_{13}\dfrac{\partial u_x}{\partial x}+C_{33}\dfrac{\partial u_z}{\partial z}\right)\mathrm{d}x\mathrm{d}z\end{bmatrix},n=1,3,\tag{20b}$$

$$\overline{D}_{i,j}=\frac{1}{\left|I_{i,j}\right|}\iint_{I_{i,j}}\rho(\mathbf{x})\mathrm{d}x\mathrm{d}z,\tag{21}$$

where $(u_x, u_z)^{\mathrm{T}}=\mathbf{u}$ is the microscale problem solution, and $I_{i,j}\in Q_{\mathrm{H}}$ represents a coarse element. The partial differential terms in Eq. (20) are calculated using a difference approximation (Abdulle and E, 2003; Jiang et al., 2022).

By substituting the microscale problem wavefield solutions in Eq. (17) into the macroscale fluxes in Eq. (20), Eq. (19) yields a 21-point FD stencil (Fig. 8(a)) of the macroscale problem:

$$\begin{aligned}&\mathbf{A}_1^{i,j}\mathbf{U}_{i-1,j-2}+\mathbf{A}_2^{i,j}\mathbf{U}_{i,j-2}+\mathbf{A}_3^{i,j}\mathbf{U}_{i+1,j-2}+\mathbf{A}_4^{i,j}\mathbf{U}_{i-2,j-1}+\mathbf{A}_5^{i,j}\mathbf{U}_{i-1,j-1}+\mathbf{A}_6^{i,j}\mathbf{U}_{i,j-1}+\mathbf{A}_7^{i,j}\mathbf{U}_{i+1,j-1}\\&+\mathbf{A}_8^{i,j}\mathbf{U}_{i+2,j-1}+\mathbf{A}_9^{i,j}\mathbf{U}_{i-2,j}+\mathbf{A}_{10}^{i,j}\mathbf{U}_{i-1,j}+\mathbf{A}_{11}^{i,j}\mathbf{U}_{i,j}+\mathbf{A}_{12}^{i,j}\mathbf{U}_{i+1,j}+\mathbf{A}_{13}^{i,j}\mathbf{U}_{i+2,j}+\mathbf{A}_{14}^{i,j}\mathbf{U}_{i-2,j+1}\\&+\mathbf{A}_{15}^{i,j}\mathbf{U}_{i-1,j+1}+\mathbf{A}_{16}^{i,j}\mathbf{U}_{i,j+1}+\mathbf{A}_{17}^{i,j}\mathbf{U}_{i+1,j+1}+\mathbf{A}_{18}^{i,j}\mathbf{U}_{i+2,j+1}+\mathbf{A}_{19}^{i,j}\mathbf{U}_{i-1,j+2}+\mathbf{A}_{20}^{i,j}\mathbf{U}_{i,j+2}+\mathbf{A}_{21}^{i,j}\mathbf{U}_{i+1,j+2}=-\mathbf{F}_{i,j},\end{aligned}\tag{22}$$

where $\mathbf{A}_n^{i,j}$ with $n = 1, \ldots, 21$ are the 2×2 coefficient matrices corresponding to the coarse element with a center point of (x_i, z_j). To attenuate the reflected wavefields from artificial boundaries of the bounded computational domain, we employ the perfectly matched layer (PML) (Zeng et al., 2001) in the difference and differential terms in Eqs. (19) and (20). The resulting PML-related coefficient matrices $\mathbf{A}_n^{i,j}$ with $n = 1, \ldots, 21$ are given in detail in Appendix B. The application of PMLs does not change the formulation of the aforementioned local elastic Helmholtz problems.

Involving all the coarse elements, the FD stencil in Eq. (22) leads to a discrete linear system:

$$\tilde{\mathbf{A}}\tilde{\mathbf{U}}=-\tilde{\mathbf{F}},\tag{23}$$

where $\tilde{\mathbf{A}}$ is a sparse square matrix (Fig. 8(b)) referred to as the impedance matrix, and $\tilde{\mathbf{U}}$ and $\tilde{\mathbf{F}}$ are column vectors of the coarse-scale wavefields and the source, respectively. Detailed formulations of the linear system are presented in Appendix C. Solving the linear system in Eq. (23) with a solver (e.g., the LU-decomposition-based solver) ultimately yields the coarse-scale elastic wavefields on Q_{H}.

This method can be extended to the three-dimensional scenario via trivial modifications of the local elastic Helmholtz problems and the macroscale problem discretization, and nontrivial alterations of the reconstruction operator and the macroscale fluxes. In the three-dimensional case, the number of multiscale basis functions that are solved from the local elastic Helmholtz problem over an H- or ε-cell increases to the value of 24. The fourth-order FD discretization of the macroscale problem will involve twelve fluxes (namely ε-cells), which finally leads to an 81-point FD stencil. Different from these trivial extensions, the reconstruction operator and macroscale fluxes cannot be obtained by straightforwardly extending their two-dimensional expressions. The three-dimensional case will yield more complicated reconstruction operator, giving rise to much complex formulations of the coupling coefficients in the microscale problem solution. As for the macroscale fluxes, their three-dimensional forms incorporate the y-direction differential terms that are omitted in the two-dimensional case. We do not give a detailed discussion since the three-dimensional FDFD-HMM is beyond the scope of this paper.

4. Numerical results

For the proposed FDFD-HMM, the H-cell size is constant after the coarse-scale discretization with a coarse mesh, whereas the ε-cell size is flexible. To achieve an optimal trade-off between the efficiency and accuracy, we attempt to use as small ε-cells as possible to produce FDFD-HMM solutions with high accuracy. For this purpose, the effect of the ε-cell size on the accuracy is first investigated in a homogeneous model and a heterogeneous model. Moreover, the effect of the coarse-mesh discretization on the accuracy is simultaneously analyzed to provide a guide for stable FDFD-HMM modeling. We subsequently use two highly heterogeneous medium models to demonstrate the superiority of FDFD-HMM over the FDFD method in terms of the accuracy and computational complexities.

A relative L_2-norm error is defined to quantify the accuracy of FDFD-HMM solutions:

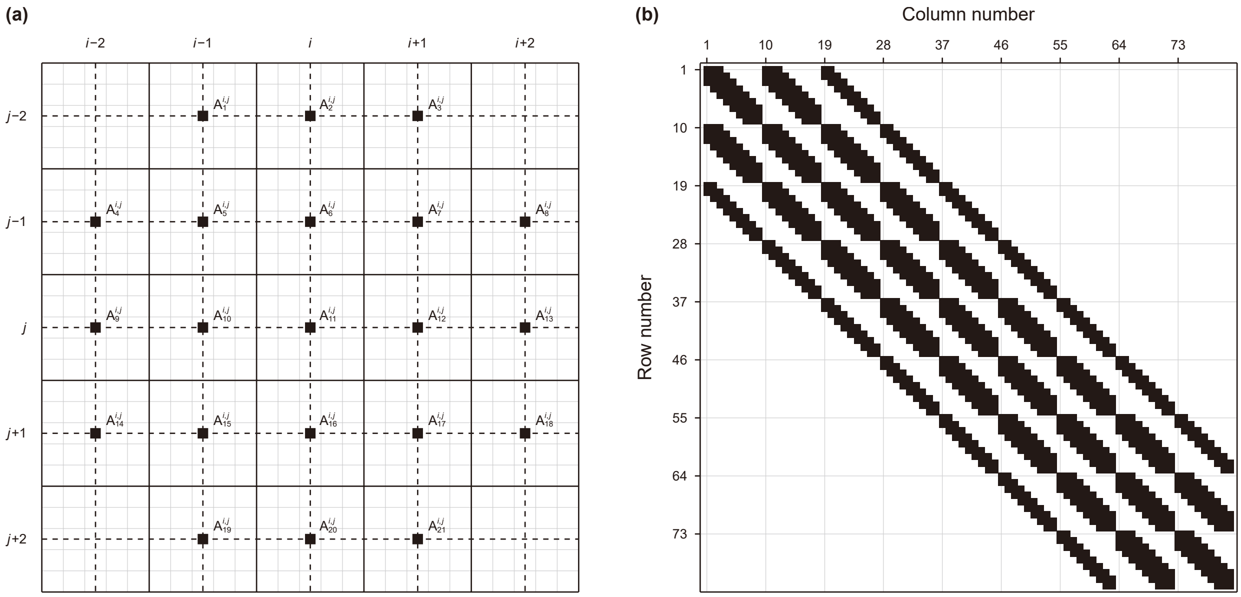

Fig. 8. Illustration of (**a**) the 21-point FD stencil and (**b**) the sparsity pattern of its corresponding impedance matrix for an example of 9 × 9 coarse mesh.

$$\ell = \frac{\left\|\mathbf{U}-\mathbf{U}_{\mathrm{ref}}\right\|_2}{\left\|\mathbf{U}_{\mathrm{ref}}\right\|_2}, \tag{24}$$

where $\mathbf{U}$ denotes the FDFD-HMM solution, and $\mathbf{U}_{\mathrm{ref}}$ denotes the analytic or FDFD solution that serves as the reference solution. To match with the scale of the FDFD-HMM solution, the reference solution computed on $\mathrm{Q_h}$ is projected onto $\mathrm{Q_H}$.

The oversampled H- and ε-cells used to construct the oscillating boundary conditions are slightly larger than the original H- and ε-cells. Generally, two additional layers of fine-mesh elements outside an original H- or ε-cell boundary suffice to provide decent FDFD-HMM solutions. Although larger oversampled cells can yield more accurate FDFD-HMM solutions, the increase in time cost is nontrivial. Because the local elastic Helmholtz problems are strictly independent of each other, we use a parallel strategy (40 threads) to compute multiscale basis functions and obtain an additional speedup.

All the operations associated with matrices and vectors for both the FDFD method and our FDFD-HMM depend on SuperLU (Li, 2005) and Armadillo (Sanderson and Curtin, 2016). Armadillo is used to efficiently generate impedance matrices in the linear systems, and it provides a SuperLU-driven interface for solving linear systems with sparse coefficient matrices.

In all the following examples, the Ricker wavelet is used as a source to generate the source-related column vector $\tilde{\mathbf{F}}$ of the linear system in Eq. (23). The frequency-domain expression of the Ricker wavelet is (Wang, 2015)

$$w(\omega)=\frac{2\omega^2}{\sqrt{\pi}\omega_0^3}\exp\left(-\frac{\omega^2}{\omega_0^2}\right), \tag{25}$$

where $\omega_0 = 2\pi f_0$ is the corresponding angular frequency of the dominant frequency f_0. We employ a vertical point source form to incorporate the Ricker wavelet into $\tilde{\mathbf{F}}$. Namely, only one external force vector $\mathbf{F}$ corresponding to the coarse element where the source is located has a nonzero value of $(0, w(\omega))^{\mathrm{T}}$ in the source-related column vector $\tilde{\mathbf{F}}$ (see Eq. (C.2) in Appendix C).

4.1. Effects of ε-cell size and coarse-mesh discretization

4.1.1. Optimal ε-cell size

A homogeneous model and a heterogeneous model are used to investigate the effect of the ε-cell size on the accuracy of FDFD-HMM. The analytic and FDFD solutions are regarded as the reference solutions in the homogeneous and heterogeneous media, respectively. The analytic reference solution with a vertical point source (Min et al., 2000) is given by

$$\begin{aligned}U_{x,\mathrm{ref}}(\mathbf{x},\omega)=&\frac{i}{4\rho v_{\mathrm{p}}^2}\cos\theta\sin\theta\mathrm{H}_0^{(1)}\left(\frac{R\omega}{v_{\mathrm{p}}}\right)-\frac{i}{4\rho v_{\mathrm{s}}^2}\cos\theta\sin\theta\mathrm{H}_0^{(1)}\left(\frac{R\omega}{v_{\mathrm{s}}}\right)\\&-\frac{i}{2\rho v_{\mathrm{p}}}\frac{\cos\theta\sin\theta}{R\omega}\mathrm{H}_1^{(1)}\left(\frac{R\omega}{v_{\mathrm{p}}}\right)+\frac{i}{2\rho v_{\mathrm{s}}}\frac{\cos\theta\sin\theta}{R\omega}\mathrm{H}_1^{(1)}\left(\frac{R\omega}{v_{\mathrm{s}}}\right),\end{aligned} \tag{26a}$$

$$\begin{aligned}U_{z,\mathrm{ref}}(\mathbf{x},\omega)=&\frac{i}{4\rho v_{\mathrm{p}}^2}\cos^2\theta\mathrm{H}_0^{(1)}\left(\frac{R\omega}{v_{\mathrm{p}}}\right)+\frac{i}{4\rho v_{\mathrm{s}}^2}\sin^2\theta\mathrm{H}_0^{(1)}\left(\frac{R\omega}{v_{\mathrm{s}}}\right)\\&-\frac{i}{4\rho v_{\mathrm{p}}}\frac{\cos^2\theta-\sin^2\theta}{R\omega}\mathrm{H}_1^{(1)}\left(\frac{R\omega}{v_{\mathrm{p}}}\right)-\frac{i}{4\rho v_{\mathrm{s}}}\frac{\sin^2\theta-\cos^2\theta}{R\omega}\mathrm{H}_1^{(1)}\left(\frac{R\omega}{v_{\mathrm{s}}}\right),\end{aligned} \tag{26b}$$

where $i=\sqrt{-1}$ is the imaginary unit, R is the distance from the source $\mathbf{x}_{\mathrm{s}} = (x_{\mathrm{s}}, z_{\mathrm{s}})$ to the receiver $\mathbf{x} = (x, z)$, $\theta = \tan^{-1}[(x - x_{\mathrm{s}})/(z - z_{\mathrm{s}})]$, and $\mathrm{H}_0^{(1)}$ and $\mathrm{H}_1^{(1)}$ are the Hankel functions of first kind with zero and first orders, respectively.

For the homogeneous model, its P- and S-wave velocities, and density are 3800 m/s, 2200 m/s and 2.43 g/cm^3, respectively. We use a global fine mesh $\mathrm{Q_h}$ with 800 fine elements of 2 m in both spatial directions to discretize the model. The coarsening ratio, the fine-element number in a coarse element in a certain direction, is $r_x = r_z = 5$. The ε-cells are partitioned by local fine meshes with a same element size of 2 m × 2 m. We use several different ε-cell sizes for the analysis. Except for the case that the x- and z-direction sizes of the ε-cells are equal, we also investigate the cases that the ε-cell size in the x direction is different from that in the z direction. For the latter, according to the distributions of $I^{\varepsilon}_{i\pm1/2,j}$ and $I^{\varepsilon}_{i,j\pm1/2}$,

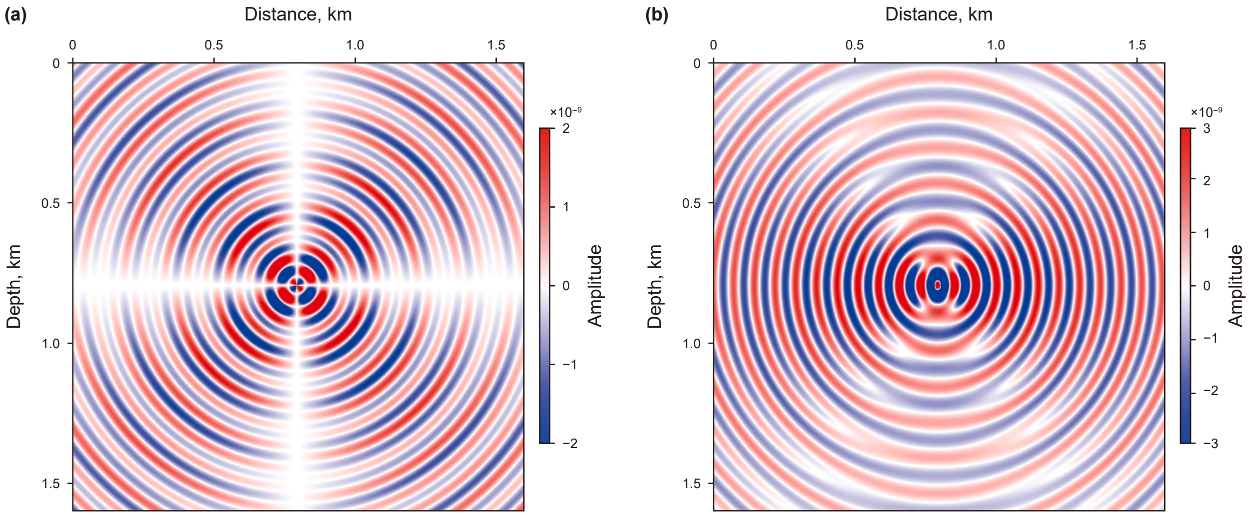

Fig. 9. The **(a)** *x*- and **(b)** *z*-component real-part wavefields of the analytic solution at 30 Hz in the homogeneous model when a vertical point source is imposed.

the size of $I^{\varepsilon}_{i\pm1/2,j}$ in a direction is set to be identical with the size of $I^{\varepsilon}_{i,j\pm1/2}$ in an orthogonal direction. Let the *x*- and *z*-direction numbers of fine elements in a local fine mesh $\mathrm{Q}^{\varepsilon}_{\mathrm{h}}$ to be N^{ε}_{x} and N^{ε}_{z}, respectively, we then define $\left[N^{\varepsilon}_{x}\right]_{I^{\varepsilon}_{i\pm1/2,j}} = \left[N^{\varepsilon}_{z}\right]_{I^{\varepsilon}_{i,j\pm1/2}} = N^{\varepsilon}_{\mathrm{p}}$ and $\left[N^{\varepsilon}_{z}\right]_{I^{\varepsilon}_{i\pm1/2,j}} = \left[N^{\varepsilon}_{x}\right]_{I^{\varepsilon}_{i,j\pm1/2}} = N^{\varepsilon}_{\mathrm{v}}$ for simplicity, where $[\cdot]_{I^{\varepsilon}_{i\pm1/2,j}}$ and $[\cdot]_{I^{\varepsilon}_{i,j\pm1/2}}$ means that variables in the brackets correspond to the ε-cell of $I^{\varepsilon}_{i\pm1/2,j}$ and $I^{\varepsilon}_{i,j\pm1/2}$, respectively. The source has a dominant frequency of 20 Hz and is located at the point of $(x,z) = (795,795)$ m. We test 5 discrete source frequencies: 10, 15, 20, 25, and 30 Hz. The PML applied to four boundaries of the computational domain has a width of 100 m.

We merely present the real parts of the *x*- and *z*-component wavefields for both the analytic and FDFD-HMM solutions at a certain frequency. Fig. 9 shows the *x*- and *z*-component wavefields of the analytic solution at the frequency of 30 Hz. We find that there are amplitude magnitude differences between the analytic solution and the FDFD-HMM solutions. The differences in absolute amplitudes are eliminated by scaling the amplitude magnitudes of the FDFD-HMM solutions to that of the analytic solution in order to facilitate comparisons. After the scaling, we compute the amplitude errors (Figs. 10 and 11) of the FDFD-HMM solutions for four representative ε-cell sizes with respect to the reference analytic solution. The results of FDFD-HMM indicate the significant effect of the ε-cell size on the accuracy. In the cases of $\left(N^{\varepsilon}_{\mathrm{p}}, N^{\varepsilon}_{\mathrm{v}}\right) = (5,5)$ and $\left(N^{\varepsilon}_{\mathrm{p}}, N^{\varepsilon}_{\mathrm{v}}\right) = (3,5)$, the FDFD-HMM solutions have obvious amplitude errors. By contrast, we observe that the amplitude errors reduce when $\left(N^{\varepsilon}_{\mathrm{p}}, N^{\varepsilon}_{\mathrm{v}}\right) = (3,3)$ and $\left(N^{\varepsilon}_{\mathrm{p}}, N^{\varepsilon}_{\mathrm{v}}\right) = (5,3)$. Especially, the ε-cell size of $\left(N^{\varepsilon}_{\mathrm{p}}, N^{\varepsilon}_{\mathrm{v}}\right) = (5,3)$ leads to the smallest amplitude errors compared with the other three ε-cell sizes.

Fig. 12 provides the accuracy evaluation of other FDFD-HMM solutions at the source frequencies of 10, 15, 20, and 25 Hz. Although the FDFD-HMM solutions at 10, 15, and 20 Hz for $\left(N^{\varepsilon}_{\mathrm{p}}, N^{\varepsilon}_{\mathrm{v}}\right) = (5,3)$ lead to slightly larger relative errors than those for $\left(N^{\varepsilon}_{\mathrm{p}}, N^{\varepsilon}_{\mathrm{v}}\right) = (3,3)$, the relative errors associated with $\left(N^{\varepsilon}_{\mathrm{p}}, N^{\varepsilon}_{\mathrm{v}}\right) = (5,3)$ still remain small values at higher frequencies.

The heterogeneous model used to verify the effect of the ε-cell size is a two-dimensional overthrust model whose P-wave velocity heterogeneity is revealed in Fig. 13. Its S-wave velocity and density are generated from the P-wave velocity by $v_{\mathrm{S}} = v_{\mathrm{P}}/\sqrt{3}$ and $\rho = 0.31\left(v_{\mathrm{P}}\right)^{0.25}$, respectively. The model is discretely parameterized by a 1000 × 720 global fine mesh Q_{h} with an element size of 3 m × 3 m. The coarsening ratio of the coarse mesh Q_{H} is set to $r_x = r_z = 5$. The source is located at $(x, z) = (1492.5, 337.5)$ m of the model, and its dominant frequency is 15 Hz. The test source frequencies include 5, 10, 15, 20, and 25 Hz. The PML width is 105 m outside each of the four boundaries. The same four representative ε-cells as in the homogeneous model are investigated.

Fig. 14 exhibits the reference FDFD solution at the test frequency of 20 Hz. An amplitude scaling of the FDFD-HMM solutions is also implemented to eliminate the amplitude magnitude differences between the FDFD-HMM and reference solutions. The wavefield differences between the FDFD-HMM and reference solutions (Figs. 15 and 16) manifest that the ε-cell size of $\left(N^{\varepsilon}_{\mathrm{p}}, N^{\varepsilon}_{\mathrm{v}}\right) = (5,3)$ also yields the most accurate solutions among four representative ε-cell sizes in the heterogeneous case. In addition, we observe obvious wavefield amplitude errors of the FDFD-HMM solutions in local model zones for $\left(N^{\varepsilon}_{\mathrm{p}}, N^{\varepsilon}_{\mathrm{v}}\right) = (3,5)$ in Figs. 15(c) and 16(c). This is due to the distorted FDFD-HMM solutions resulting from the severe numerical dispersion when $\left(N^{\varepsilon}_{\mathrm{p}}, N^{\varepsilon}_{\mathrm{v}}\right) = (3,5)$.

The relative L_2-norm errors in Fig. 17 also indicate that the FDFD-HMM solutions corresponding to $\left(N^{\varepsilon}_{\mathrm{p}}, N^{\varepsilon}_{\mathrm{v}}\right) = (5,3)$ are more accurate than those associated with the other three ε-cell sizes, and the distorted solutions for $\left(N^{\varepsilon}_{\mathrm{p}}, N^{\varepsilon}_{\mathrm{v}}\right) = (3,5)$ have the highest errors. These results in the heterogeneous model are in good agreement with that in the homogeneous model.

According to the previous investigations, we ultimately follow the conclusions implied by Figs. 10–12 and 15–17 to determine the optimal ε-cell size. Because the fine-element size of $\mathrm{Q}^{\varepsilon}_{\mathrm{h}}$ is set to be identical to those of $\mathrm{Q}^{\mathrm{H}}_{\mathrm{h}}$ and Q_{h}, we merely need to determine the fine-element number in $\mathrm{Q}^{\varepsilon}_{\mathrm{h}}$ for determining an ε-cell size. In consequence, the optimal ε-cell size is given by $N^{\varepsilon}_{x} = r_x$ and $N^{\varepsilon}_{z} = 3$ for $I^{\varepsilon}_{i\pm1/2,j}$, while we have $N^{\varepsilon}_{x} = 3$ and $N^{\varepsilon}_{z} = r_z$ for $I^{\varepsilon}_{i,j\pm1/2}$.

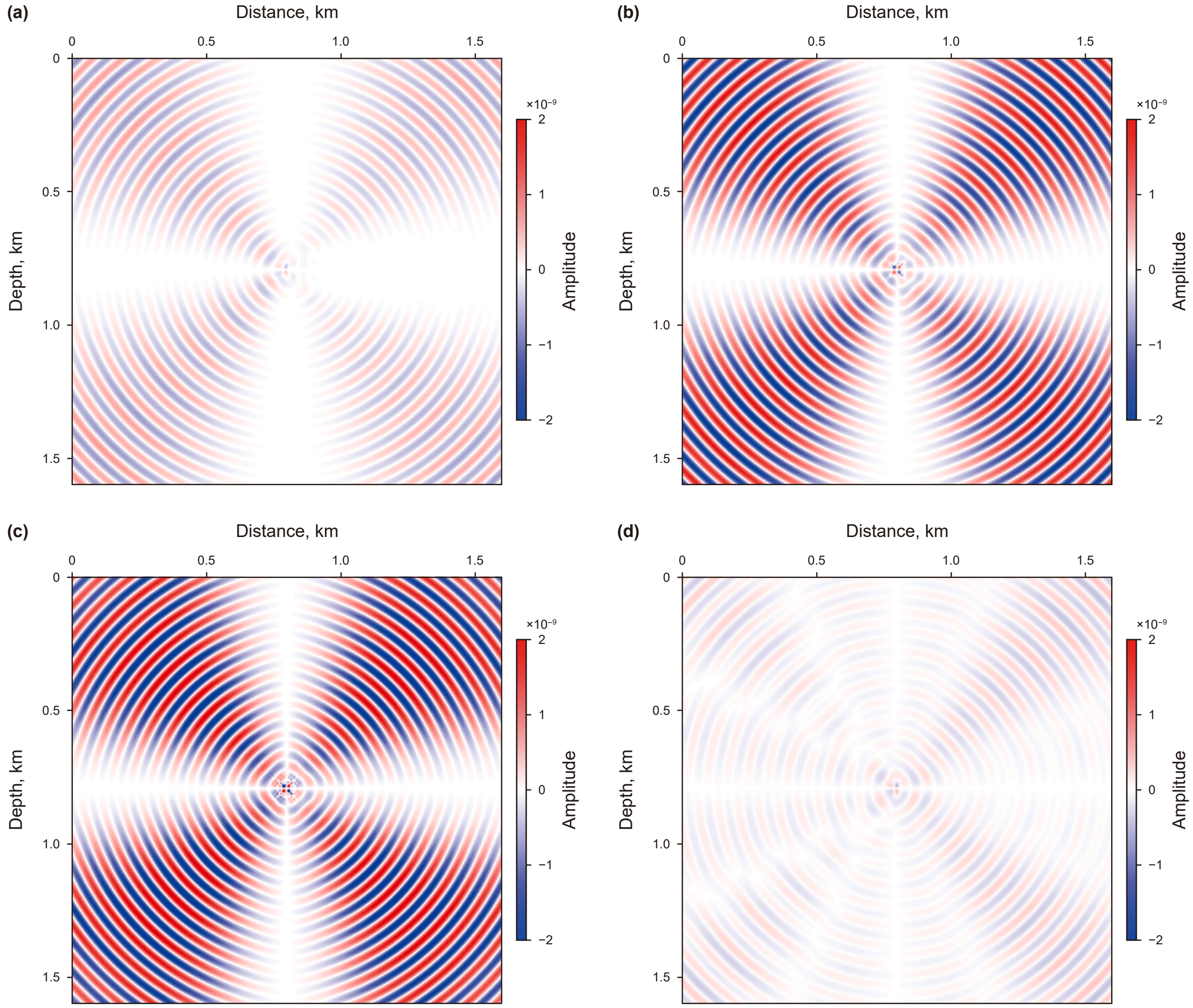

Fig. 10. Amplitude errors of the x-component real-part wavefields of the FDFD-HMM solutions at 30 Hz for the ε-cell sizes of **(a)** $\left(N_{\mathrm{p}}^{\varepsilon}, N_{\mathrm{v}}^{\varepsilon}\right) = (3,3)$, **(b)** $\left(N_{\mathrm{p}}^{\varepsilon}, N_{\mathrm{v}}^{\varepsilon}\right) = (5,5)$, **(c)** $\left(N_{\mathrm{p}}^{\varepsilon}, N_{\mathrm{v}}^{\varepsilon}\right) = (3,5)$, and **(d)** $\left(N_{\mathrm{p}}^{\varepsilon}, N_{\mathrm{v}}^{\varepsilon}\right) = (5,3)$ with respect to the reference analytic solution in the homogeneous model.

4.1.2. Minimum coarse-element number per S-wave wavelength

Figs. 12 and 17 manifest a degraded accuracy with the increase of source frequency for FDFD-HMM. This phenomenon results from the decrease in coarse elements per wavelength as the frequency increases. The numerical dispersion analysis in homogeneous media is a routine approach to estimate the minimum of grid-point number per wavelength for stable FDFD modeling (Jiang et al., 2022). However, the dependence of the coefficient matrices in Eq. (22) on the medium-dependent multiscale basis functions and fine-mesh-dependent bilinear interpolation operator (see Appendices A and B) results in prohibitive application of the numerical dispersion analysis to FDFD-HMM. For this issue, we implement convergence analyses of the FDFD method and our FDFD-HMM in a homogeneous medium to investigate the effect of the coarse-mesh discretization on the accuracy for providing a guide of stable FDFD-HMM modeling. This investigation is performed based on the optimal ε-cell size concluded from the above analyses.

We set the space domain to [0,1] × [0,1]. The P- and S-wave velocities and the density are 3000 m/s, 1800 m/s, and 2.2 g/cm^3, respectively. We solve the elastic Helmholtz equation on the fine grids with fine element sizes of 1/35, 1/70, 1/140, 1/280, and 1/560 for the FDFD method and on the coarse grids with coarse element sizes of 1/7, 1/14, 1/28, 1/56, and 1/112 for FDFD-HMM under four source frequencies of 9, 10, 12, 17 kHz.

Fig. 18 shows the relative errors of the FDFD and FDFD-HMM solutions with respect to the exact analytic solutions given by Eq. (26). These solutions become more accurate as the number of grid elements increases (element size equivalently decreases). At the frequency of 17 kHz, the grid with fine element size of 1/35 leads to the minimum number of fine grid elements per S-wave wavelength in all the cases (Table 1). This value of 3.7 is close to the minimum number of required grid points per S-wave wavelength for the phase velocity error of approximate 2% in the FDFD method, meaning a decent accuracy of all the FDFD solutions. Therefore, provided the relative errors of the FDFD-HMM solutions are close to or even lower than those of the FDFD solutions, we can consider that FDFD-HMM has a comparable accuracy to the FDFD method with a phase velocity error of less than 2%. We use the relative errors of the FDFD solution corresponding to the fine element size of 1/35 and the frequency of 17 kHz (Fig. 18(d)) as a threshold (blue dashed lines in Fig. 18). For the FDFD-HMM solutions whose

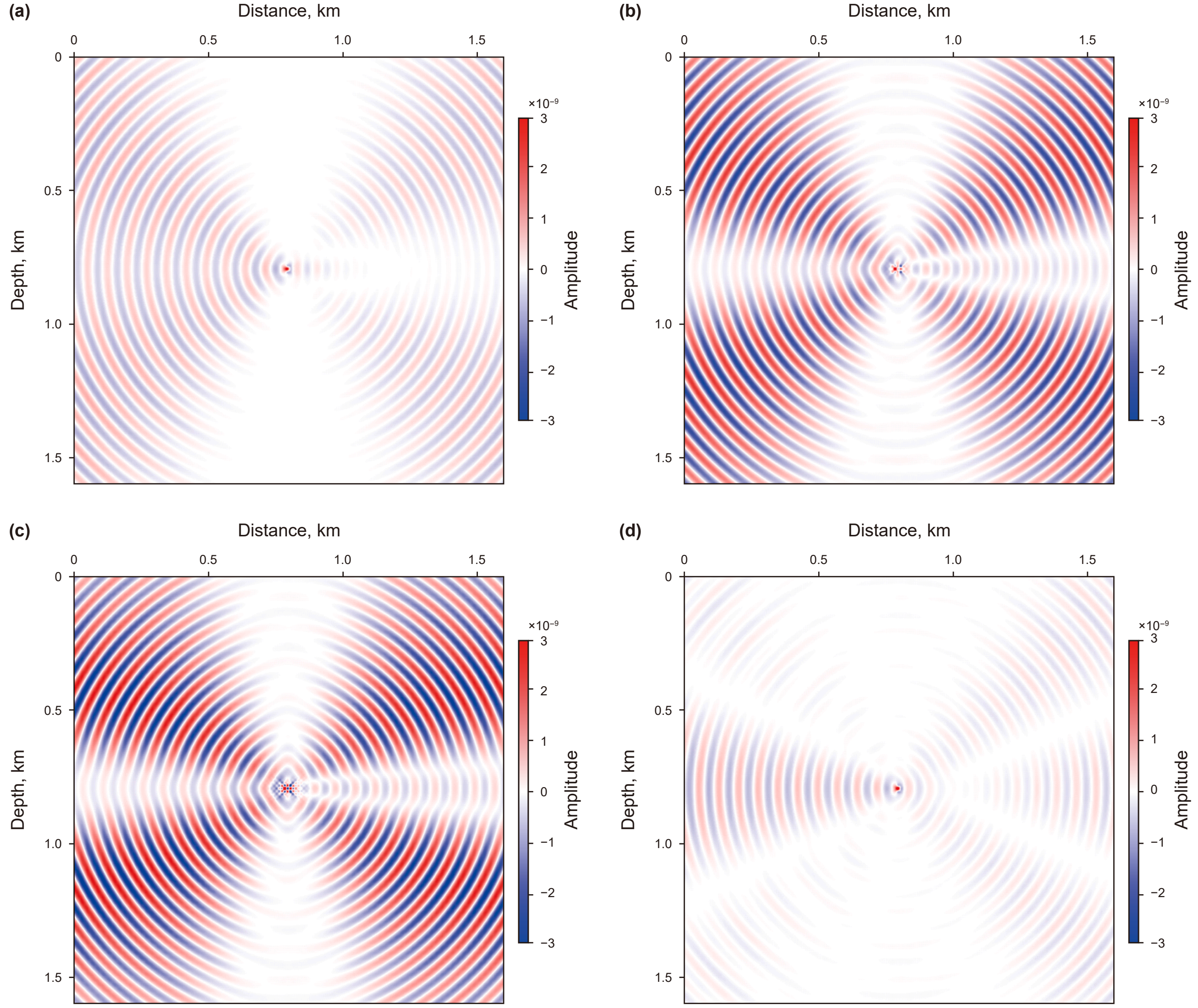

Fig. 11. Amplitude errors of the *z*-component real-part wavefields of the FDFD-HMM solutions at 30 Hz for the ε-cell sizes of **(a)** $\left(N_{\mathrm{p}}^{\varepsilon}, N_{\mathrm{v}}^{\varepsilon}\right) = (3,3)$, **(b)** $\left(N_{\mathrm{p}}^{\varepsilon}, N_{\mathrm{v}}^{\varepsilon}\right) = (5,5)$, **(c)** $\left(N_{\mathrm{p}}^{\varepsilon}, N_{\mathrm{v}}^{\varepsilon}\right) = (3,5)$, and **(d)** $\left(N_{\mathrm{p}}^{\varepsilon}, N_{\mathrm{v}}^{\varepsilon}\right) = (5,3)$ with respect to the reference analytic solution in the homogeneous model.

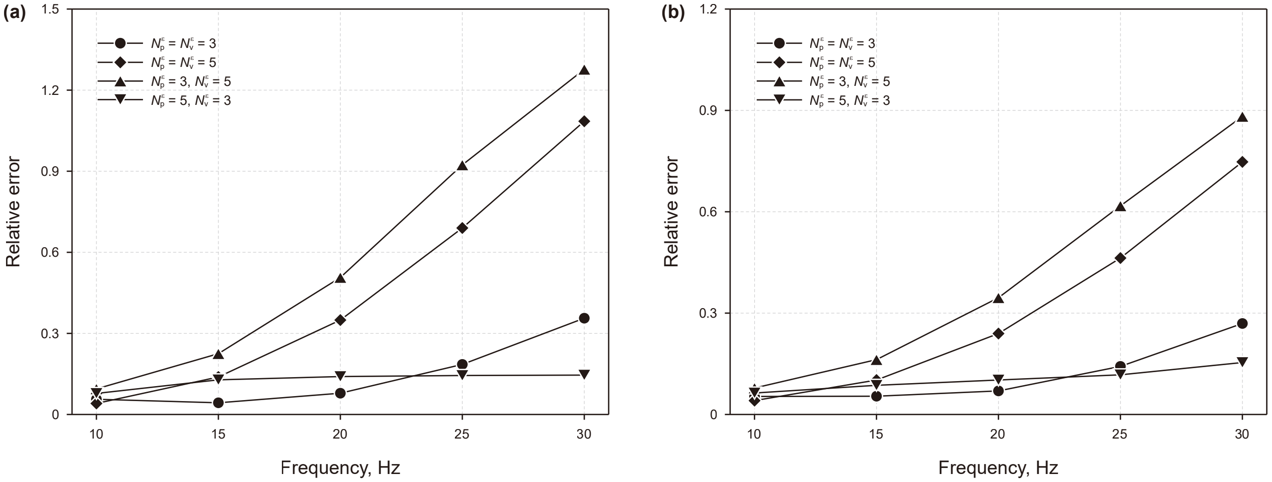

Fig. 12. Relative L$_2$-norm errors of the **(a)** *x*- and **(b)** *z*-component real-part wavefields of the FDFD-HMM solutions for different ε-cell sizes and source frequencies in the homogeneous model.

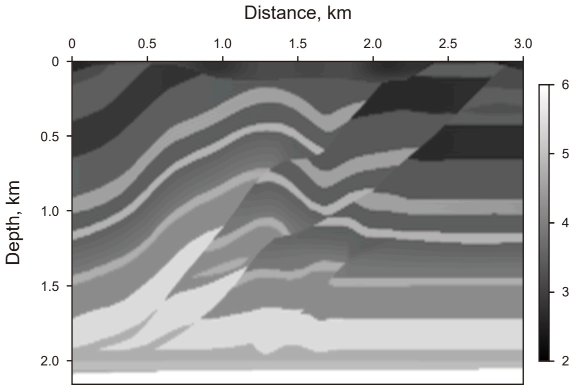

Fig. 13. Overthrust P-wave velocity model.

relative errors are lower than this threshold, they can be regarded as decent solutions. Combining Fig. 18 with Table 1, we find that at least five coarse elements per S-wave wavelength are required to generate a decent FDFD-HMM solution.

Based on the aforementioned investigations, we thus recommend the fewest coarse elements of 5 per S-wave wavelength for stable FDFD-HMM modeling with the optimal ε-cell size. Nevertheless, this recommended value can be moderately reduced due to the local structure of low S-wave velocity in actual heterogeneous media.

4.2. Performance analysis

Two highly heterogeneous examples are used to validate the superior performance in terms of the computational complexities

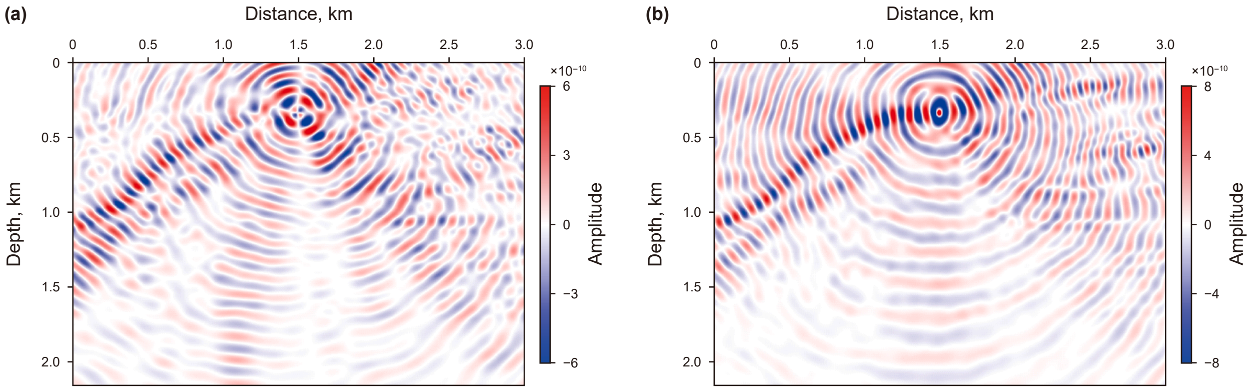

Fig. 14. The **(a)** *x*- and **(b)** *z*-component real-part wavefields of the reference FDFD solution at 20 Hz in the heterogeneous overthrust model when a vertical point source is imposed.

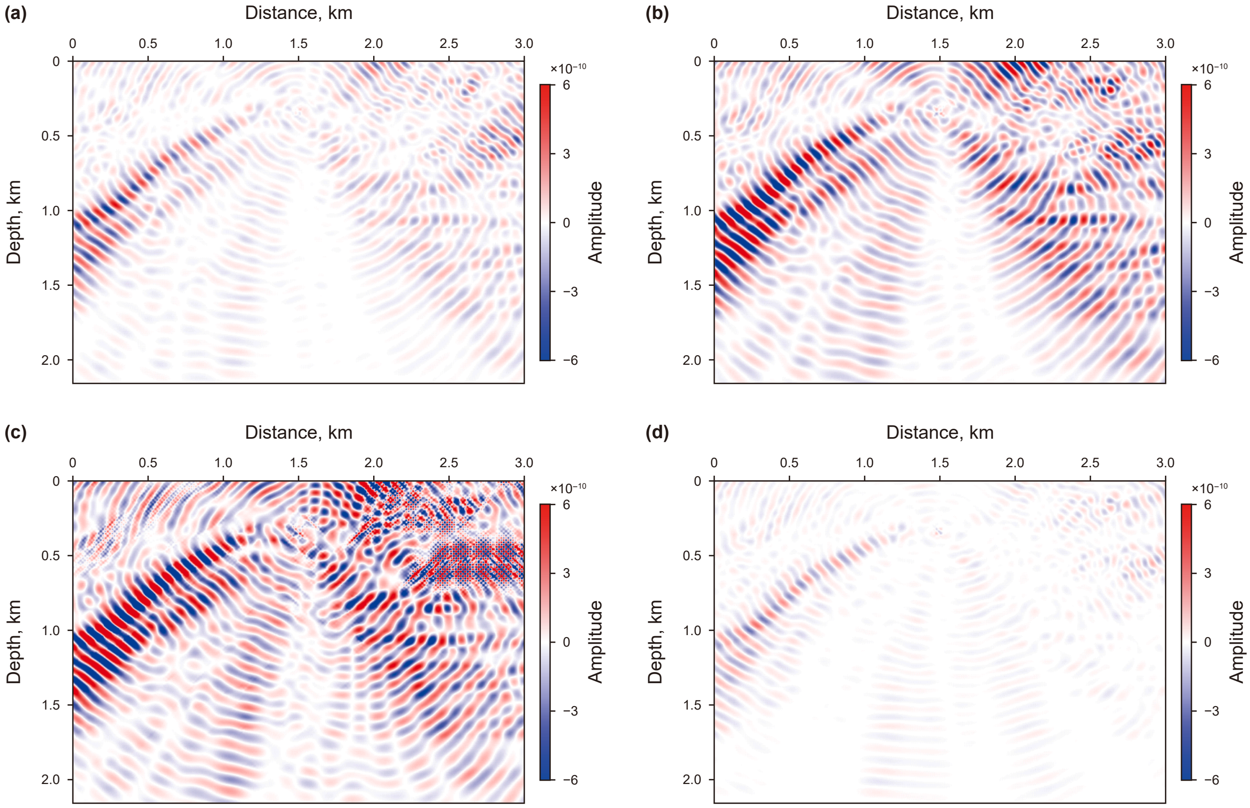

Fig. 15. Amplitude errors of the *x*-component real-part wavefields of the FDFD-HMM solutions at 20 Hz for the ε-cell sizes of **(a)** $\left(N_{\mathrm{p}}^{\varepsilon}, N_{\mathrm{v}}^{\varepsilon}\right) = (3,3)$, **(b)** $\left(N_{\mathrm{p}}^{\varepsilon}, N_{\mathrm{v}}^{\varepsilon}\right) = (5,5)$, **(c)** $\left(N_{\mathrm{p}}^{\varepsilon}, N_{\mathrm{v}}^{\varepsilon}\right) = (3,5)$, and **(d)** $\left(N_{\mathrm{p}}^{\varepsilon}, N_{\mathrm{v}}^{\varepsilon}\right) = (5,3)$ with respect to the reference FDFD solution in the heterogeneous overthrust model.

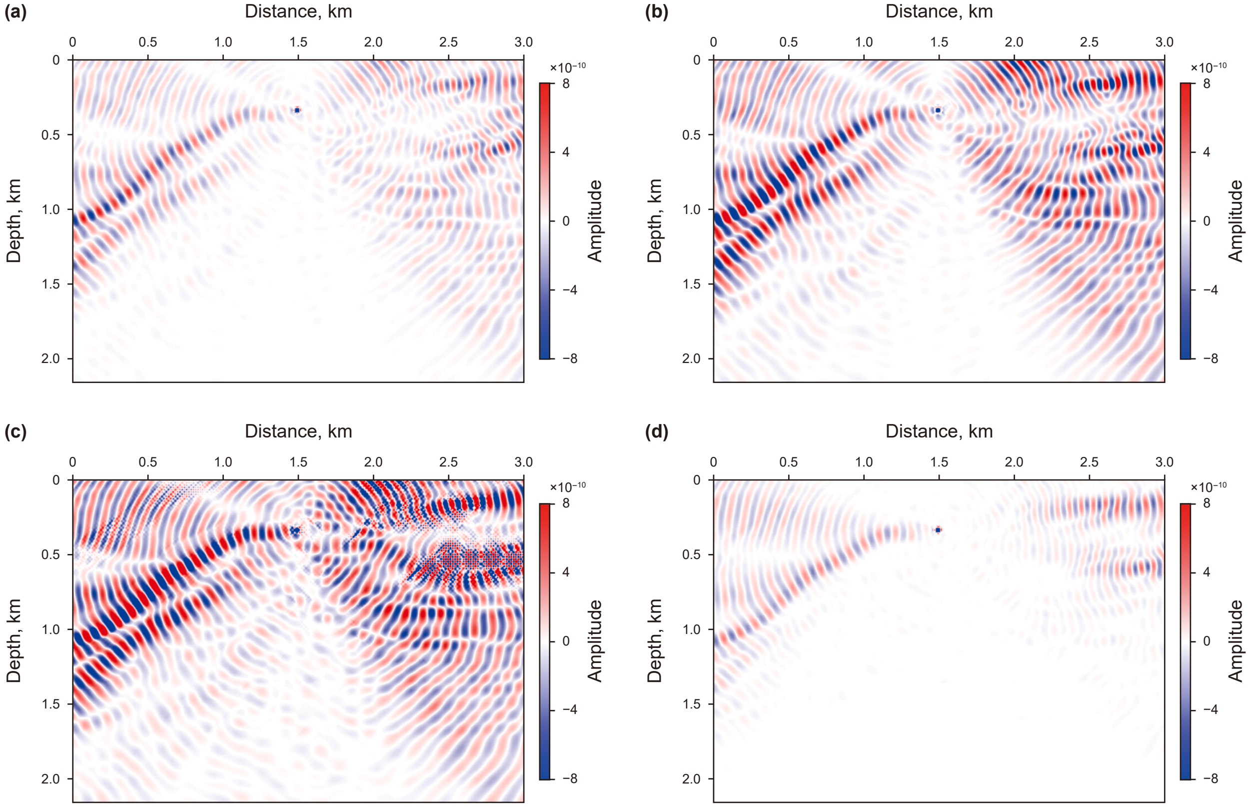

Fig. 16. Amplitude errors of the *z*-component real-part wavefields of the FDFD-HMM solutions at 20 Hz for the ε-cell sizes of **(a)** $\left(N_{\mathrm{p}}^{\varepsilon}, N_{\mathrm{v}}^{\varepsilon}\right) = (3,3)$, **(b)** $\left(N_{\mathrm{p}}^{\varepsilon}, N_{\mathrm{v}}^{\varepsilon}\right) = (5,5)$, **(c)** $\left(N_{\mathrm{p}}^{\varepsilon}, N_{\mathrm{v}}^{\varepsilon}\right) = (3,5)$, and **(d)** $\left(N_{\mathrm{p}}^{\varepsilon}, N_{\mathrm{v}}^{\varepsilon}\right) = (5,3)$ with respect to the reference FDFD solution in the heterogeneous overthrust model.

of FDFD-HMM while maintaining a comparable accuracy to the conventional FDFD method. We refer to the runtime of assembling impedance matrix for the FDFD method and the total runtime of constructing multiscale basis functions and assembling impedance matrix for FDFD-HMM as "offline time". A corresponding terminology "online time" refers to the elapsed time of solving a linear system. The runtime and memory consumption in the following two examples are measured on a computer with Intel i7-14700 CPU.

4.2.1. Periodical medium model

We first design a highly heterogeneous model with periodical heterogeneities to verify FDFD-HMM. The P-wave velocity model of this periodical medium is determined by

$$v_{\mathrm{p}}(x,z) = \left[\frac{10+\sin(2\pi x/70)}{10+\cos(2\pi z/70)} + \frac{10+\sin(2\pi z/70)}{10+\cos(2\pi x/70)}\right] \times 1750. \qquad (27)$$

Fig. 19 presents part of the periodical P-wave velocity model. We use $v_{\mathrm{s}} = v_{\mathrm{p}}/\sqrt{3}$ and $\rho = 0.31\left(v_{\mathrm{p}}\right)^{0.25}$ to generate the S-wave

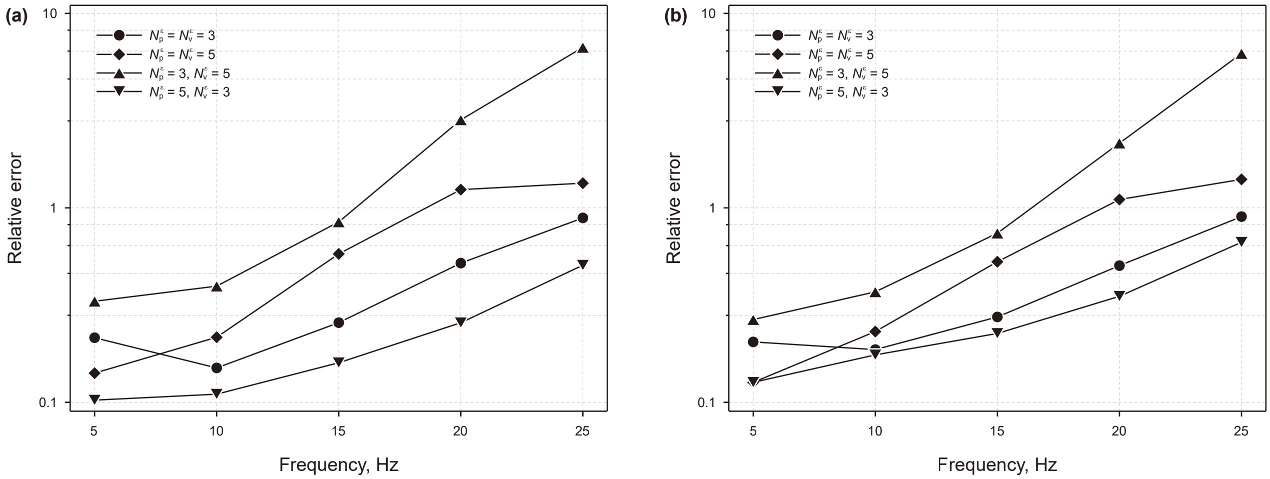

Fig. 17. Relative L_2-norm errors of the **(a)** *x*- and **(b)** *z*-component real-part wavefields of the FDFD-HMM solutions for different ε-cell sizes and source frequencies in the heterogeneous overthrust model.

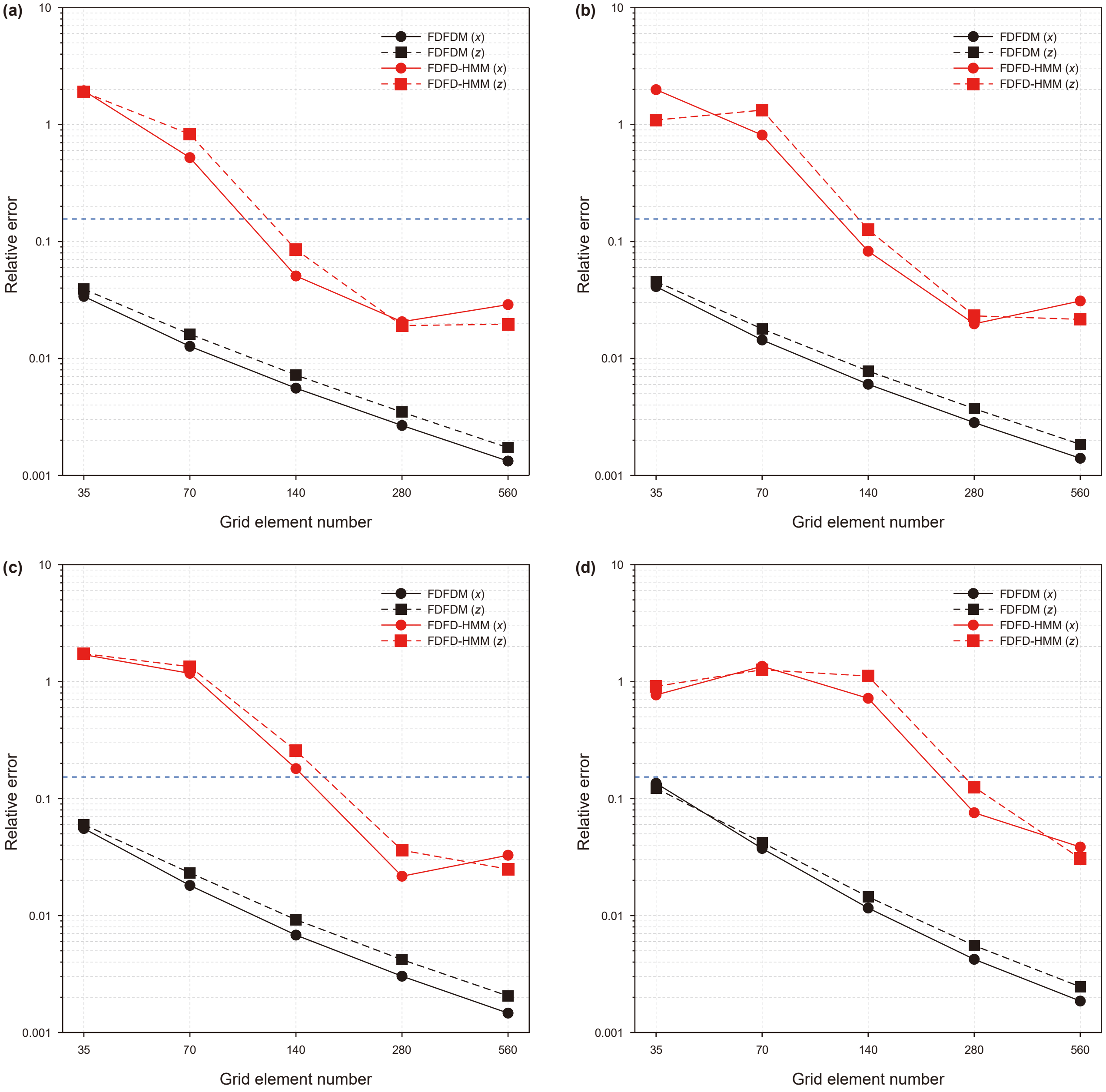

Fig. 18. Convergence benchmark for the two component solutions of the FDFD method and our FDFD-HMM at frequencies of **(a)** 9, **(b)** 10, **(c)** 12, **(d)** 17 kHz. The blue dashed lines indicate a threshold below which the FDFD solutions have phase velocity errors of less than 2%.

velocity and density, respectively. These property models are parameterized by a global fine mesh Q_h containing 1000 × 800 fine elements with an element size of 2 m in both spatial directions. We set the coarse-element size of Q_H to be 10 m in both directions, which means $r_x = r_z = 5$. Based on the conclusion regarding the optimal ε-cell size, the sizes of $I^{\varepsilon}_{i\pm1/2,j}$ and $I^{\varepsilon}_{i,j\pm1/2}$ are set to 10 m × 6 m and 6 m × 10 m, respectively. The PML applied to each domain boundary includes 50 fine elements or 10 coarse elements. As a result, the number of mesh elements including the PMLs is 1100 × 900 in Q_h and 220 × 180 in Q_H. We locate the source with a dominant frequency of 15 Hz at $(x, z) = (995, 205)$ m of the model.

In Fig. 20, we show the reference FDFD solution (Fig. 20(a) and (b)) computed on Q_h, and the multiscale solution (Fig. 20(c) and (d)) computed using FDFD-HMM on Q_H. An amplitude scaling of the FDFD-HMM solutions is also performed. Although the heterogeneities complicate the wavefields because its comparable size to half of the S-wave wavelength results in non-negligible elastic scattering, FDFD-HMM can yield similar wavefield characteristics to the FDFD method. To give an insight into the accuracy of

Table 1
Number of coarse elements per S-wave wavelength for different grids and frequencies.

Fine element size	$1/G_h$				$1/G_H$			
	9 kHz	10 kHz	12 kHz	17 kHz	9 kHz	10 kHz	12 kHz	17 kHz
1/35	7.00	6.30	5.25	3.70	1.40	1.26	1.05	0.74
1/70	14.00	12.60	10.50	7.41	2.80	2.52	2.10	1.48
1/140	28.00	25.20	21.00	14.82	5.60	5.04	4.20	2.96
1/280	56.00	50.40	42.00	29.64	11.20	10.08	8.40	5.92
1/560	112.00	100.80	84.00	59.29	22.40	20.16	16.80	11.85

$1/G_h$ and $1/G_H$ represent the minimum numbers of fine and coarse elements per S-wave wavelength, respectively.

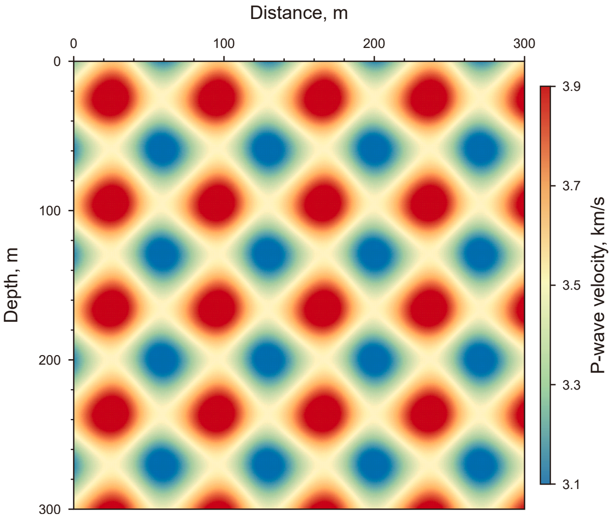

Fig. 19. Part P-wave velocity model of the periodical medium. The other zones of the periodical medium model possess the same heterogeneity structure.

the multiscale solution, we present its amplitude differences with respect to the reference solution in Fig. 21. The corresponding relative L$_2$-norm errors of the multiscale solution are 0.167 and 0.155 (columns of ℓ_{20} in Table 2) for the x and z components, respectively. In order to further validate the accuracy of FDFD-HMM, we compute FDFD and FDFD-HMM solutions with a frequency interval of 0.5 Hz in 0–40 Hz to produce time-domain seismograms (Fig. 22). For FDFD-HMM, the average number of coarse elements per S-wave wavelength is 5.1 at 40 Hz, satisfying the recommended coarse-element number for stable FDFD-HMM modeling. The seismograms are obtained by receivers located at $z = 0$ m and with a space interval of 20 m. We find a good agreement of the FDFD-HMM seismograms with the reference FDFD seismograms.

We measure the runtime and peak memory shown in Table 2 for implementing FDFD and FDFD-HMM simulations. The offline stage of FDFD-HMM is more time-consuming than that of the FDFD method. This anomaly results from the additional time cost of the multiscale basis function construction (column T_{basis} in Table 2) and the increased time cost of the impedance matrix assembly (column T_{A} in Table 2). The increase in T_{A} for FDFD-HMM is caused by a large amount of summation operations for the macroscale flux estimation. Whereas, the online runtime measured from FDFD-HMM account for merely 0.62% of that for the FDFD method (column T_{online} in Table 2). In consequence, FDFD-HMM contributes to a substantial time reduction of 94.2% for modeling the time-domain seismogram (column T_{total} in Table 2). Besides the time reduction, FDFD-HMM contributes to a significant saving in memory requirement. Compared with the FDFD method, FDFD-HMM reduces the memory cost by 45.2% (column M_{WSP} in Table 2). It is worth mentioning that our program is designed to be applicable to dynamic frequency-dependent models. The storage of the dynamic models instead of a static frequency-independent model increases memory consumption notably. If we do not consider the memory cost (13190.77 MB)

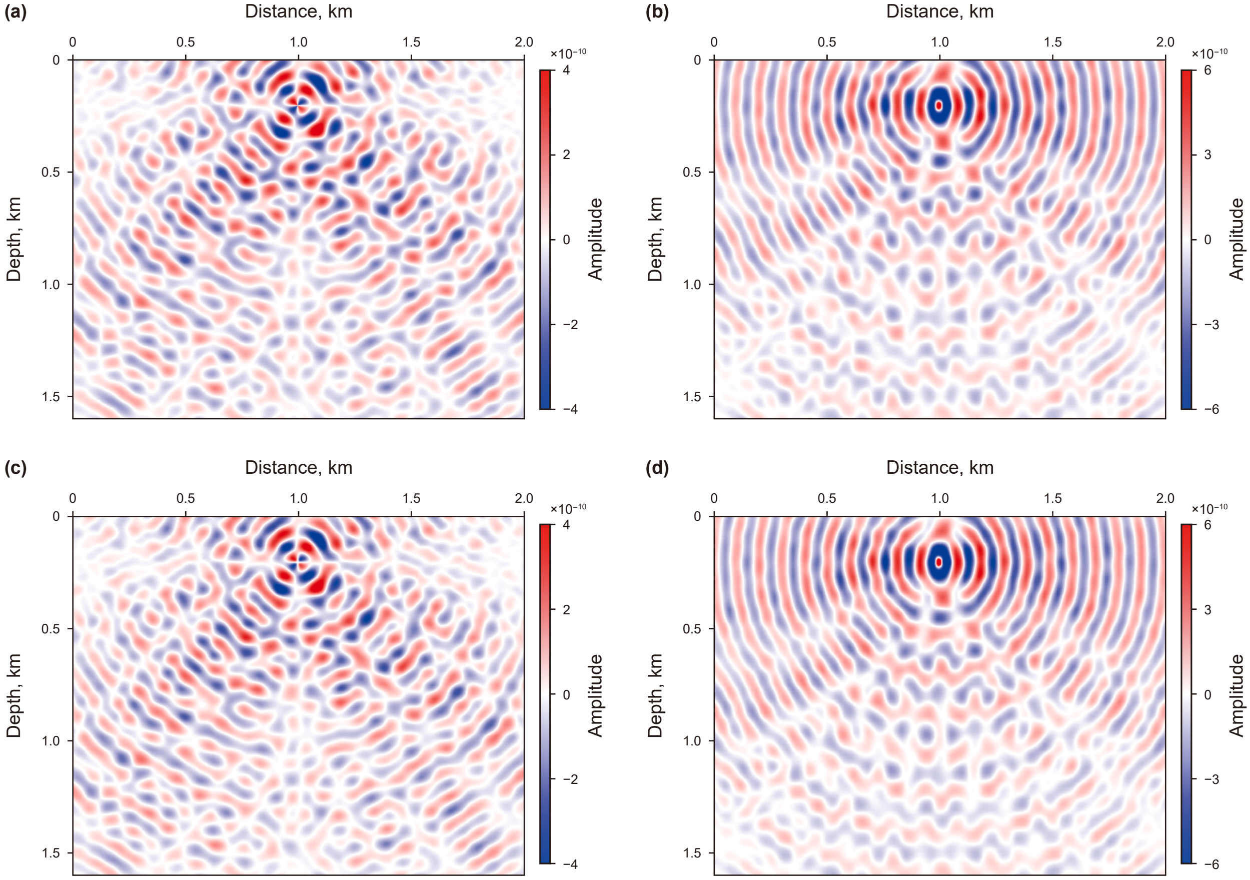

Fig. 20. The (**a** and **c**) x- and (**b** and **d**) z-component real-part wavefields of the (**a** and **b**) reference FDFD solution and (**c** and **d**) FDFD-HMM solution at 20 Hz in the periodical medium model.

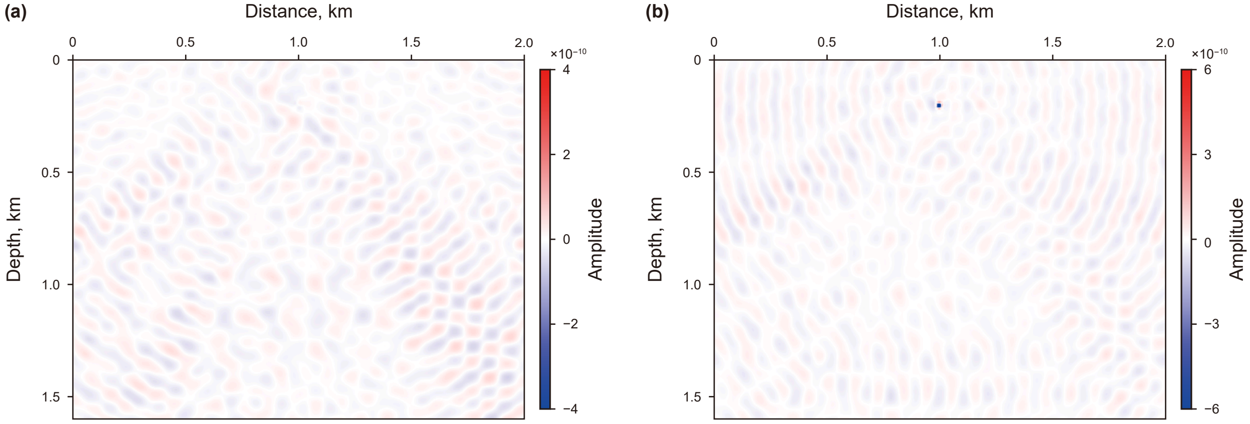

Fig. 21. Amplitude differences of the **(a)** *x*- and **(b)** *z*-component real-part wavefields between the FDFD-HMM solution and the reference FDFD solution in the periodical medium model.

Table 2
Performance comparisons between the FDFD method and FDFD-HMM for the periodical medium model.

Method	(N_x, N_z)	T_{offline}, s		T_{online}, s	T_{total}, s	M_{WSP}, MB	$\mathscr{E}_{20}$	
		T_{basis}	$T_{\mathbf{A}}$				$\Re[U_x]$	$\Re[U_z]$
FDFD	(1100, 900)	–	28.09	5184.69	417012.20	28217.58	–	–
FDFD-HMM	(220, 180)	241.31	82.05	32.18	24261.50	15455.27	0.167	0.155

N_x and N_z represent the *x*- and *z*-direction element numbers in Q_h or Q_H including the PMLs, respectively. T_{offline} and T_{online} are the elapsed times in the offline and online stages, respectively. T_{basis} and T_{A} are the elapsed times of the basis function construction and impedance matrix assembly, respectively. T_{total} denotes the runtime of computing the time-domain seismograms. M_{WSP} denotes peak memory consumption. $\mathscr{E}_{20}$ represents the relative L_2-norm error of the multiscale solution at 20 Hz, and $\Re[U_x]$ and $\Re[U_z]$ are the *x*- and *z*-component real-part wavefields, respectively.

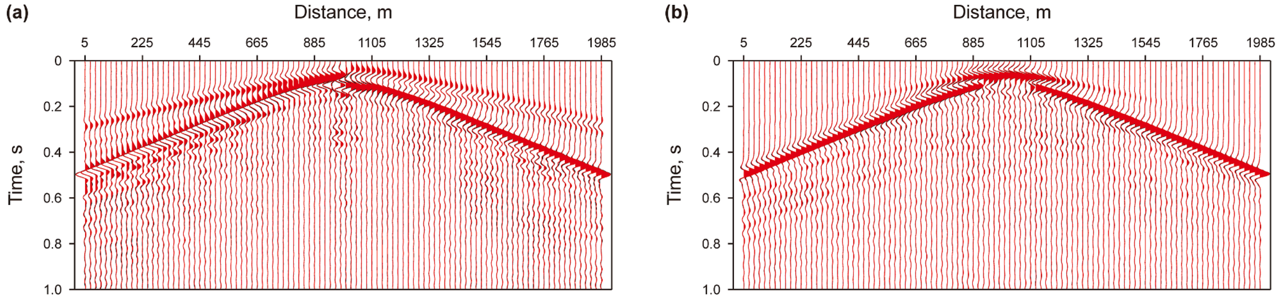

Fig. 22. Comparisons of the **(a)** *x*- and **(b)** *z*-component seismograms between the reference FDFD solution (black line) and FDFD-HMM solution (red line) for the periodical medium model.

attributed to the dynamic model storage, FDFD-HMM can lead to a memory reduction of as high as 84.9%.

4.2.2. Random medium model

We next design a highly heterogeneous random medium model via the von Kármán correlation function (Bohlen, 2002; Klimeš, 2002; Hong and Kennett, 2003). The P-wave velocity model of this random medium is shown in Fig. 23. We use a same means as in the previous case to construct the S-wave velocity and density models. The model is heterogeneous at the scale of global fine mesh Q_h. There are 900 fine elements in both spatial directions and the fine-element size is 2 m × 2 m in Q_h. A coarse mesh Q_H with $r_x = r_z = 5$ is designed for a coarse-scale computational domain discretization. Therefore, there are 180 coarse elements with an element size of 10 m in both directions in Q_H. The chosen sizes of $I^{\varepsilon}_{i\pm1/2,j}$ and $I^{\varepsilon}_{i,j\pm1/2}$ are 10 m × 6 m and 6 m × 10 m, respectively. The application of PML increases a width of 100 m outside each model boundary, which finally leads to 1000 × 1000 fine elements and 200 × 200 coarse elements. The source is imposed at $(x, z) = (855, 225)$ m of the model.

The wavefields in Fig. 24(a), (b) are the *x* and *z* components of the reference FDFD solution, and Fig. 24(c), (d) presents the two-component wavefields of the FDFD-HMM solution. We do not observe distinctly visible wavefield differences between the two solutions. FDFD-HMM only gives rise to weak amplitude errors in its solution with respect to the reference FDFD solution (Fig. 25). The corresponding relative errors are 0.157 and 0.171 (columns of $\mathscr{E}_{20}$ in Table 3) for the *x*- and *z*-component FDFD-HMM solutions, respectively. Similarly, we compute frequency-domain wavefields in 0–40 Hz using the FDFD method and FDFD-HMM to generate their time-domain seismograms. There are on average 6.3 coarse elements per S-wave wavelength at 40 Hz, implying a stable FDFD-

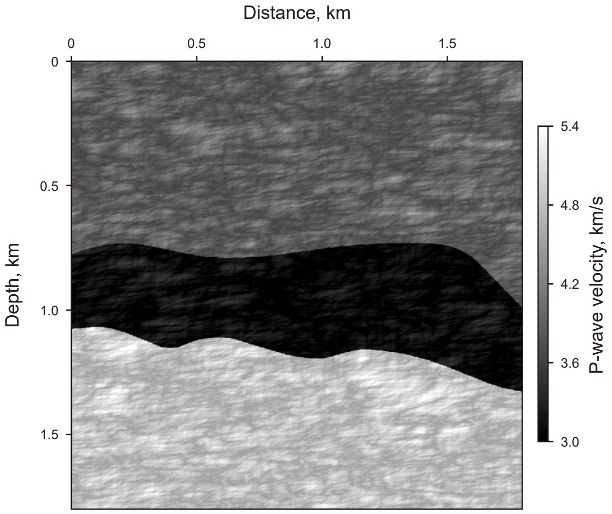

Fig. 23. P-wave velocity model of von Kármán correlation random medium.

HMM modeling. The seismograms in Fig. 26 are obtained by receivers with the same layout as the previous periodic example. FDFD-HMM reproduces the FDFD seismograms, demonstrating the decent accuracy of FDFD-HMM.

In addition, Table 3 shows the measured time and memory costs. Similar to the previous periodical case, FDFD-HMM results in higher offline time compared with the FDFD method (columns of T_{offline} in Table 3), yet it dramatically lowers the online time (column T_{online} in Table 3). As a result, the total computation time using the FDFD-HMM is essentially reduced (column T_{total} in Table 3). In the frequency domain, the online stage computation time usually matters most for practical applications (Fu et al., 2019). We just need to repeat the online stage computation for multisource wave modeling. Therefore, FDFD-HMM can be fairly efficient when we implement wave simulation for a set of sources. Regarding the memory cost, FDFD-HMM consumes approximately 56.8% of the memory resource required by the FDFD method (column M_{WSP} in Table 3). Without taking the memory cost (13763.82 MB) of dynamic model storage into account, the

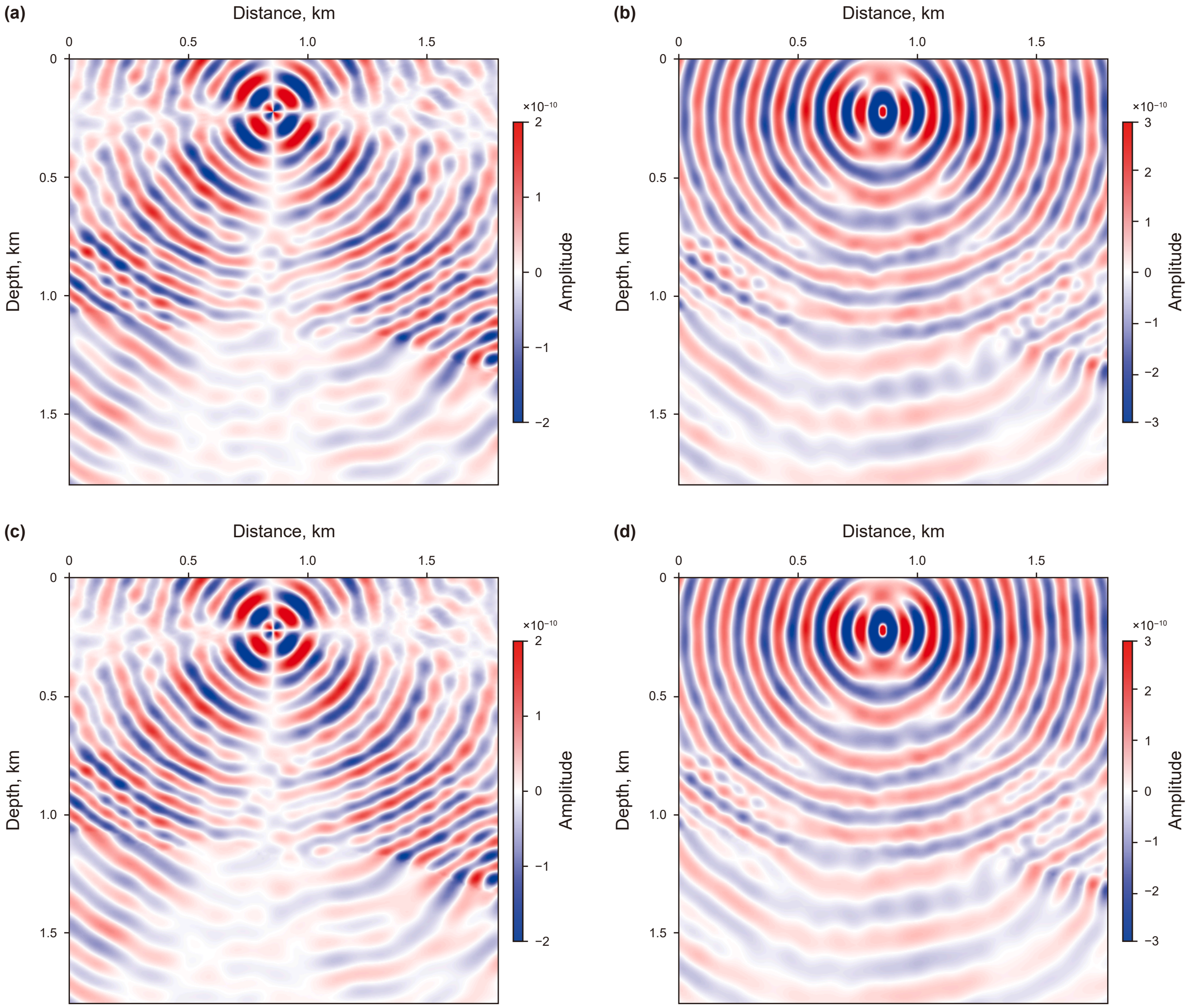

Fig. 24. The (**a** and **c**) *x*- and (**b** and **d**) *z*-component real-part wavefields of the (**a** and **b**) reference solution and (**c** and **d**) FDFD-HMM solution at 20 Hz in the random medium model.

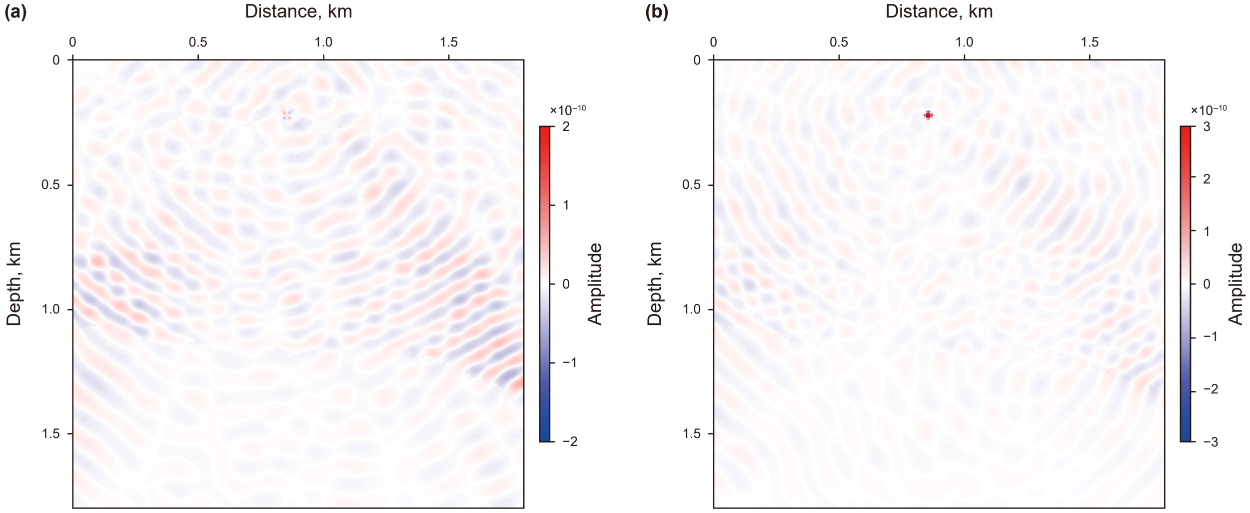

Fig. 25. Amplitude differences of the **(a)** x- and **(b)** z-component real-part wavefields between the FDFD-HMM solution and the reference FDFD solution in the random medium model.

Table 3
Performance comparisons between the FDFD method and FDFD-HMM for the random medium model.

Method	(N_x, N_z)	T_{offline}, s		T_{online}, s	T_{total}, s	M_{WSP}, MB	ℓ_{20}	
		T_{basis}	$T_{\mathbf{A}}$				$\Re[U_x]$	$\Re[U_z]$
FDFD	(1000, 1000)	–	20.41	4876.76	393140.36	28277.33	–	–
FDFD-HMM	(200, 200)	242.33	84.36	24.93	26425.10	16072.38	0.157	0.171

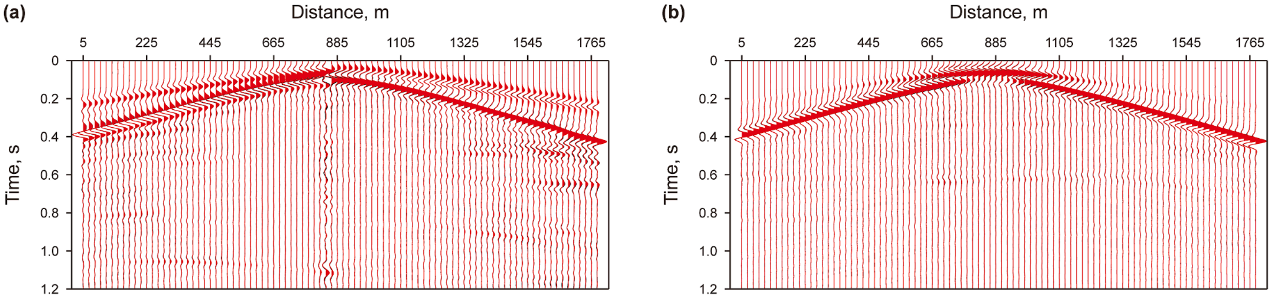

Fig. 26. Comparisons of the **(a)** x- and **(b)** z-component seismograms between the reference FDFD solution (black line) and FDFD-HMM solution (red line) for the random medium model.

required memory resources for FDFD-HMM are merely 15.9% of that for the FDFD method.

5. Conclusions

In the general framework of HMM, we have developed an FDFD-driven multiscale method to solve the elastic Helmholtz equation in isotropic media with fine-scale heterogeneities. The FDFD method is used as a numerical solver to solve the two-scale problems in the HMM framework. Constructed from the microscale problems, the multiscale basis functions capture the effect of fine-scale heterogeneity in medium properties. Based on the downscaling reconstruction operator and upscaling flux estimation, these multiscale basis functions are incorporated into the ultimate discrete macroscale problem system with a reduced degree of freedom. We use several numerical examples to certify the accuracy and computational complexities of our developed FDFD-HMM. The results of the homogeneous and heterogeneous models suggest significant impacts of the ε-cell size and coarse-mesh discretization on the accuracy, and conclude rules for determining the optimal ε-cell size and minimum coarse-element number per S-wave wavelength. The results of two highly heterogeneous models demonstrate that FDFD-HMM is capable of solving the elastic Helmholtz equation with decent accuracy and low computational burden compared with the conventional FDFD method. However, the reconstruction operator for downscaling coupling between the microscale and macroscale problems are complicated in the elastic case, which increases the computation time of the offline stage and introduces more potential errors. Some efforts are still necessary to further develop accurate and simple reconstruction operator in the future works.

CRediT authorship contribution statement

Wei Jiang: Writing – review & editing, Writing – original draft, Validation, Software, Methodology, Conceptualization. **Xue-Hua Chen:** Writing – review & editing, Validation, Supervision, Project administration, Methodology, Investigation, Funding acquisition, Formal analysis, Conceptualization. **Cong Wang:** Visualization, Data curation.

Declaration of interests

The authors declare that they have no known competing financial interests or personal relationships that could have appeared to influence the work reported in this paper.

Acknowledgements

The authors would like to acknowledge the financial support received from the National Natural Foundation of China (Grant No. 42374163), the Key Program of Natural Science Foundation of Sichuan Province (Grant No. 2023NSFSC0019), and the Open Fund of Key Laboratory of Earth Exploration and Information Techniques (Chengdu University of Technology), Ministry of Education (Grant No. EEME202505).

Appendix A. Wavefield solutions of microscale problems

The related H-cells of $I^{\varepsilon}_{i\pm1/2,j}$ are $I^{\mathrm{H}}_{i\pm1/2,j-1/2}$ and $I^{\mathrm{H}}_{i\pm1/2,j+1/2}$, and their coarse-scale boundary nodes include $\mathbf{x}_1=(x_{(i\pm1/2)-1/2},z_{j-1})$, $\mathbf{x}_2=(x_{(i\pm1/2)+1/2},z_{j-1})$, $\mathbf{x}_3=(x_{(i\pm1/2)-1/2},z_j)$, $\mathbf{x}_4=(x_{(i\pm1/2)+1/2},z_j)$, $\mathbf{x}_5=(x_{(i\pm1/2)-1/2},z_{j+1})$, and $\mathbf{x}_6=(x_{(i\pm1/2)+1/2},z_{j+1})$. The solutions of the local microscale problems over $I^{\varepsilon}_{i\pm1/2,j}$ are only constrained by the coarse-scale wavefields at these points. Thus, the specific form of the coupling expression in Eq. (17) for $I^{\varepsilon}_{i\pm1/2,j}$ is

$$\begin{aligned}\mathbf{u}(\boldsymbol{\xi},\omega)=&\,\mathbf{c}_1^{\pm}(\boldsymbol{\xi},\omega)\mathbf{U}\left(x_{(i\pm1/2)-1/2},z_{j-1},\omega\right)+\mathbf{c}_2^{\pm}(\boldsymbol{\xi},\omega)\mathbf{U}\left(x_{(i\pm1/2)+1/2},z_{j-1},\omega\right)\\&+\mathbf{c}_3^{\pm}(\boldsymbol{\xi},\omega)\mathbf{U}\left(x_{(i\pm1/2)-1/2},z_j,\omega\right)+\mathbf{c}_4^{\pm}(\boldsymbol{\xi},\omega)\mathbf{U}\left(x_{(i\pm1/2)+1/2},z_j,\omega\right)\\&+\mathbf{c}_5^{\pm}(\boldsymbol{\xi},\omega)\mathbf{U}\left(x_{(i\pm1/2)-1/2},z_{j+1},\omega\right)+\mathbf{c}_6^{\pm}(\boldsymbol{\xi},\omega)\mathbf{U}\left(x_{(i\pm1/2)+1/2},z_{j+1},\omega\right),\end{aligned}\tag{A.1}$$

where the coupling coefficient matrix $\mathbf{c}_n^{\pm}(\boldsymbol{\xi},\omega)$ with $n=1,\ldots,6$ is specifically defined as

$$\mathbf{c}_n^{\pm}(\boldsymbol{\xi},\omega)=\begin{bmatrix}\mathbf{c}_{n,x}^{\pm}(\boldsymbol{\xi},\omega)\\\mathbf{c}_{n,z}^{\pm}(\boldsymbol{\xi},\omega)\end{bmatrix}=\begin{bmatrix}c_{n,xx}^{\pm}(\boldsymbol{\xi},\omega)&c_{n,xz}^{\pm}(\boldsymbol{\xi},\omega)\\c_{n,zx}^{\pm}(\boldsymbol{\xi},\omega)&c_{n,zz}^{\pm}(\boldsymbol{\xi},\omega)\end{bmatrix}.\tag{A.2}$$

The H-cells associated with $I^{\varepsilon}_{i,j\pm1/2}$ are $I^{\mathrm{H}}_{i-1/2,j\pm1/2}$ and $I^{\mathrm{H}}_{i+1/2,j\pm1/2}$, and their coarse-scale boundary nodes include $\mathbf{x}_1=(x_{i-1},z_{(j\pm1/2)-1/2})$, $\mathbf{x}_2=(x_i,z_{(j\pm1/2)-1/2})$, $\mathbf{x}_3=(x_{i+1},z_{(j\pm1/2)-1/2})$, $\mathbf{x}_4=(x_{i-1},z_{(j\pm1/2)+1/2})$, $\mathbf{x}_5=(x_i,z_{(j\pm1/2)+1/2})$, and $\mathbf{x}_6=(x_{i+1},z_{(j\pm1/2)+1/2})$. As a consequence, the specific formulation of the local microscale problem solution in Eq. (17) for $I^{\varepsilon}_{i,j\pm1/2}$ is

$$\begin{aligned}\mathbf{u}(\boldsymbol{\xi},\omega)=&\,\mathbf{d}_1^{\pm}(\boldsymbol{\xi},\omega)\mathbf{U}\left(x_{i-1},z_{(j\pm1/2)-1/2},\omega\right)+\mathbf{d}_2^{\pm}(\boldsymbol{\xi},\omega)\mathbf{U}\left(x_i,z_{(j\pm1/2)-1/2},\omega\right)\\&+\mathbf{d}_3^{\pm}(\boldsymbol{\xi},\omega)\mathbf{U}\left(x_{i+1},z_{(j\pm1/2)-1/2},\omega\right)+\mathbf{d}_4^{\pm}(\boldsymbol{\xi},\omega)\mathbf{U}\left(x_{i-1},z_{(j\pm1/2)+1/2},\omega\right)\\&+\mathbf{d}_5^{\pm}(\boldsymbol{\xi},\omega)\mathbf{U}\left(x_i,z_{(j\pm1/2)+1/2},\omega\right)+\mathbf{d}_6^{\pm}(\boldsymbol{\xi},\omega)\mathbf{U}\left(x_{i+1},z_{(j\pm1/2)+1/2},\omega\right),\end{aligned}\tag{A.3}$$

where the coupling coefficient matrix $\mathbf{d}_n^{\pm}(\boldsymbol{\xi},\omega)$ with $n=1,\ldots,6$ is specifically defined as

$$\mathbf{d}_n^{\pm}(\boldsymbol{\xi},\omega)=\begin{bmatrix}\mathbf{d}_{n,x}^{\pm}(\boldsymbol{\xi},\omega)\\\mathbf{d}_{n,z}^{\pm}(\boldsymbol{\xi},\omega)\end{bmatrix}=\begin{bmatrix}d_{n,xx}^{\pm}(\boldsymbol{\xi},\omega)&d_{n,xz}^{\pm}(\boldsymbol{\xi},\omega)\\d_{n,zx}^{\pm}(\boldsymbol{\xi},\omega)&d_{n,zz}^{\pm}(\boldsymbol{\xi},\omega)\end{bmatrix}.\tag{A.4}$$

All elements in these two types of the coupling coefficient matrices can be summarized as a general form as follows:

$$\varpi_{n,\alpha\beta}(\boldsymbol{\xi},\omega)=\varpi^{\mathbf{x}_1}_{n,\alpha\beta}(\boldsymbol{\xi},\omega)+\varpi^{\mathbf{x}_2}_{n,\alpha\beta}(\boldsymbol{\xi},\omega)+\varpi^{\mathbf{x}_3}_{n,\alpha\beta}(\boldsymbol{\xi},\omega)+\varpi^{\mathbf{x}_4}_{n,\alpha\beta}(\boldsymbol{\xi},\omega), \tag{A.5}$$

with

$$\begin{aligned}\varpi^{\mathbf{x}_1}_{n,\alpha\beta}(\boldsymbol{\xi},\omega)=&\left(1-\frac{\xi^{[1]}-\chi_1^{[1]}}{\Delta\chi}\right)\left(1-\frac{\eta^{[1]}-\gamma_1^{[1]}}{\Delta\gamma}\right)\left[\varphi^{\mathrm{H}(\mathbf{x}_1)}_{x,M_1}\left(\chi_1^{[1]},\gamma_1^{[1]},\omega\right)\varphi^{\varepsilon}_{\alpha,1}(\boldsymbol{\xi},\omega)+\varphi^{\mathrm{H}(\mathbf{x}_1)}_{z,M_1}\left(\chi_1^{[1]},\gamma_1^{[1]},\omega\right)\varphi^{\varepsilon}_{\alpha,5}(\boldsymbol{\xi},\omega)\right]\\&+\frac{\xi^{[1]}-\chi_1^{[1]}}{\Delta\chi}\left(1-\frac{\eta^{[1]}-\gamma_1^{[1]}}{\Delta\gamma}\right)\left[\varphi^{\mathrm{H}(\mathbf{x}_1)}_{x,M_1}\left(\chi_2^{[1]},\gamma_2^{[1]},\omega\right)\varphi^{\varepsilon}_{\alpha,1}(\boldsymbol{\xi},\omega)+\varphi^{\mathrm{H}(\mathbf{x}_1)}_{z,M_1}\left(\chi_2^{[1]},\gamma_2^{[1]},\omega\right)\varphi^{\varepsilon}_{\alpha,5}(\boldsymbol{\xi},\omega)\right]\\&+\left(1-\frac{\xi^{[1]}-\chi_1^{[1]}}{\Delta\chi}\right)\frac{\eta^{[1]}-\gamma_1^{[1]}}{\Delta\gamma}\left[\varphi^{\mathrm{H}(\mathbf{x}_1)}_{x,M_1}\left(\chi_3^{[1]},\gamma_3^{[1]},\omega\right)\varphi^{\varepsilon}_{\alpha,1}(\boldsymbol{\xi},\omega)+\varphi^{\mathrm{H}(\mathbf{x}_1)}_{z,M_1}\left(\chi_3^{[1]},\gamma_3^{[1]},\omega\right)\varphi^{\varepsilon}_{\alpha,5}(\boldsymbol{\xi},\omega)\right]\\&+\frac{\xi^{[1]}-\chi_1^{[1]}}{\Delta\chi}\frac{\eta^{[1]}-\gamma_1^{[1]}}{\Delta\gamma}\left[\varphi^{\mathrm{H}(\mathbf{x}_1)}_{x,M_1}\left(\chi_4^{[1]},\gamma_4^{[1]},\omega\right)\varphi^{\varepsilon}_{\alpha,1}(\boldsymbol{\xi},\omega)+\varphi^{\mathrm{H}(\mathbf{x}_1)}_{z,M_1}\left(\chi_4^{[1]},\gamma_4^{[1]},\omega\right)\varphi^{\varepsilon}_{\alpha,5}(\boldsymbol{\xi},\omega)\right],\end{aligned} \tag{A.6}$$

$$\begin{aligned}\varpi^{\mathbf{x}_2}_{n,\alpha\beta}(\boldsymbol{\xi},\omega)=&\left(1-\frac{\xi^{[2]}-\chi_1^{[2]}}{\Delta\chi}\right)\left(1-\frac{\eta^{[2]}-\gamma_1^{[2]}}{\Delta\gamma}\right)\left[\varphi^{\mathrm{H}(\mathbf{x}_2)}_{x,M_2}\left(\chi_1^{[2]},\gamma_1^{[2]},\omega\right)\varphi^{\varepsilon}_{\alpha,2}(\boldsymbol{\xi},\omega)+\varphi^{\mathrm{H}(\mathbf{x}_2)}_{z,M_2}\left(\chi_1^{[2]},\gamma_1^{[2]},\omega\right)\varphi^{\varepsilon}_{\alpha,6}(\boldsymbol{\xi},\omega)\right]\\&+\frac{\xi^{[2]}-\chi_1^{[2]}}{\Delta\chi}\left(1-\frac{\eta^{[2]}-\gamma_1^{[2]}}{\Delta\gamma}\right)\left[\varphi^{\mathrm{H}(\mathbf{x}_2)}_{x,M_2}\left(\chi_2^{[2]},\gamma_2^{[2]},\omega\right)\varphi^{\varepsilon}_{\alpha,2}(\boldsymbol{\xi},\omega)+\varphi^{\mathrm{H}(\mathbf{x}_2)}_{z,M_2}\left(\chi_2^{[2]},\gamma_2^{[2]},\omega\right)\varphi^{\varepsilon}_{\alpha,6}(\boldsymbol{\xi},\omega)\right]\\&+\left(1-\frac{\xi^{[2]}-\chi_1^{[2]}}{\Delta\chi}\right)\frac{\eta^{[2]}-\gamma_1^{[2]}}{\Delta\gamma}\left[\varphi^{\mathrm{H}(\mathbf{x}_2)}_{x,M_2}\left(\chi_3^{[2]},\gamma_3^{[2]},\omega\right)\varphi^{\varepsilon}_{\alpha,2}(\boldsymbol{\xi},\omega)+\varphi^{\mathrm{H}(\mathbf{x}_2)}_{z,M_2}\left(\chi_3^{[2]},\gamma_3^{[2]},\omega\right)\varphi^{\varepsilon}_{\alpha,6}(\boldsymbol{\xi},\omega)\right]\\&+\frac{\xi^{[2]}-\chi_1^{[2]}}{\Delta\chi}\frac{\eta^{[2]}-\gamma_1^{[2]}}{\Delta\gamma}\left[\varphi^{\mathrm{H}(\mathbf{x}_2)}_{x,M_2}\left(\chi_4^{[2]},\gamma_4^{[2]},\omega\right)\varphi^{\varepsilon}_{\alpha,2}(\boldsymbol{\xi},\omega)+\varphi^{\mathrm{H}(\mathbf{x}_2)}_{z,M_2}\left(\chi_4^{[2]},\gamma_4^{[2]},\omega\right)\varphi^{\varepsilon}_{\alpha,6}(\boldsymbol{\xi},\omega)\right],\end{aligned} \tag{A.7}$$

$$\begin{aligned}\varpi^{\mathbf{x}_3}_{n,\alpha\beta}(\boldsymbol{\xi},\omega)=&\left(1-\frac{\xi^{[3]}-\chi_1^{[3]}}{\Delta\chi}\right)\left(1-\frac{\eta^{[3]}-\gamma_1^{[3]}}{\Delta\gamma}\right)\left[\varphi^{\mathrm{H}(\mathbf{x}_3)}_{x,M_3}\left(\chi_1^{[3]},\gamma_1^{[3]},\omega\right)\varphi^{\varepsilon}_{\alpha,3}(\boldsymbol{\xi},\omega)+\varphi^{\mathrm{H}(\mathbf{x}_3)}_{z,M_3}\left(\chi_1^{[3]},\gamma_1^{[3]},\omega\right)\varphi^{\varepsilon}_{\alpha,7}(\boldsymbol{\xi},\omega)\right]+\frac{\xi^{[3]}-\chi_1^{[3]}}{\Delta\chi}\Bigg(1\\&-\frac{\eta^{[3]}-\gamma_1^{[3]}}{\Delta\gamma}\Bigg)\left[\varphi^{\mathrm{H}(\mathbf{x}_3)}_{x,M_3}\left(\chi_2^{[3]},\gamma_2^{[3]},\omega\right)\varphi^{\varepsilon}_{\alpha,3}(\boldsymbol{\xi},\omega)+\varphi^{\mathrm{H}(\mathbf{x}_3)}_{z,M_3}\left(\chi_2^{[3]},\gamma_2^{[3]},\omega\right)\varphi^{\varepsilon}_{\alpha,7}(\boldsymbol{\xi},\omega)\right]+\Bigg(1\\&-\frac{\xi^{[3]}-\chi_1^{[3]}}{\Delta\chi}\Bigg)\frac{\eta^{[3]}-\gamma_1^{[3]}}{\Delta\gamma}\left[\varphi^{\mathrm{H}(\mathbf{x}_3)}_{x,M_3}\left(\chi_3^{[3]},\gamma_3^{[3]},\omega\right)\varphi^{\varepsilon}_{\alpha,3}(\boldsymbol{\xi},\omega)+\varphi^{\mathrm{H}(\mathbf{x}_3)}_{z,M_3}\left(\chi_3^{[3]},\gamma_3^{[3]},\omega\right)\varphi^{\varepsilon}_{\alpha,7}(\boldsymbol{\xi},\omega)\right]\\&+\frac{\xi^{[3]}-\chi_1^{[3]}}{\Delta\chi}\frac{\eta^{[3]}-\gamma_1^{[3]}}{\Delta\gamma}\left[\varphi^{\mathrm{H}(\mathbf{x}_3)}_{x,M_3}\left(\chi_4^{[3]},\gamma_4^{[3]},\omega\right)\varphi^{\varepsilon}_{\alpha,3}(\boldsymbol{\xi},\omega)+\varphi^{\mathrm{H}(\mathbf{x}_3)}_{z,M_3}\left(\chi_4^{[3]},\gamma_4^{[3]},\omega\right)\varphi^{\varepsilon}_{\alpha,7}(\boldsymbol{\xi},\omega)\right],\end{aligned} \tag{A.8}$$

$$\begin{aligned}\varpi^{\mathbf{x}_4}_{n,\alpha\beta}(\boldsymbol{\xi},\omega)=&\left(1-\frac{\xi^{[4]}-\chi_1^{[4]}}{\Delta\chi}\right)\left(1-\frac{\eta^{[4]}-\gamma_1^{[4]}}{\Delta\gamma}\right)\left[\varphi^{\mathrm{H}(\mathbf{x}_4)}_{x,M_4}\left(\chi_1^{[4]},\gamma_1^{[4]},\omega\right)\varphi^{\varepsilon}_{\alpha,4}(\boldsymbol{\xi},\omega)+\varphi^{\mathrm{H}(\mathbf{x}_4)}_{z,M_4}\left(\chi_1^{[4]},\gamma_1^{[4]},\omega\right)\varphi^{\varepsilon}_{\alpha,8}(\boldsymbol{\xi},\omega)\right]\\&+\frac{\xi^{[4]}-\chi_1^{[4]}}{\Delta\chi}\left(1-\frac{\eta^{[4]}-\gamma_1^{[4]}}{\Delta\gamma}\right)\left[\varphi^{\mathrm{H}(\mathbf{x}_4)}_{x,M_4}\left(\chi_2^{[4]},\gamma_2^{[4]},\omega\right)\varphi^{\varepsilon}_{\alpha,4}(\boldsymbol{\xi},\omega)+\varphi^{\mathrm{H}(\mathbf{x}_4)}_{z,M_4}\left(\chi_2^{[4]},\gamma_2^{[4]},\omega\right)\varphi^{\varepsilon}_{\alpha,8}(\boldsymbol{\xi},\omega)\right]\\&+\left(1-\frac{\xi^{[4]}-\chi_1^{[4]}}{\Delta\chi}\right)\frac{\eta^{[4]}-\gamma_1^{[4]}}{\Delta\gamma}\left[\varphi^{\mathrm{H}(\mathbf{x}_4)}_{x,M_4}\left(\chi_3^{[4]},\gamma_3^{[4]},\omega\right)\varphi^{\varepsilon}_{\alpha,4}(\boldsymbol{\xi},\omega)+\varphi^{\mathrm{H}(\mathbf{x}_4)}_{z,M_4}\left(\chi_3^{[4]},\gamma_3^{[4]},\omega\right)\varphi^{\varepsilon}_{\alpha,8}(\boldsymbol{\xi},\omega)\right]\\&+\frac{\xi^{[4]}-\chi_1^{[4]}}{\Delta\chi}\frac{\eta^{[4]}-\gamma_1^{[4]}}{\Delta\gamma}\left[\varphi^{\mathrm{H}(\mathbf{x}_4)}_{x,M_4}\left(\chi_4^{[4]},\gamma_4^{[4]},\omega\right)\varphi^{\varepsilon}_{\alpha,4}(\boldsymbol{\xi},\omega)+\varphi^{\mathrm{H}(\mathbf{x}_4)}_{z,M_4}\left(\chi_4^{[4]},\gamma_4^{[4]},\omega\right)\varphi^{\varepsilon}_{\alpha,8}(\boldsymbol{\xi},\omega)\right],\end{aligned} \tag{A.9}$$

where $n = 1, \ldots, 6$, and $\alpha, \beta = x, z$.

In Eq. (A.6)–(A.9), the multiscale basis functions $\boldsymbol{\varphi}^{\mathrm{H}(\mathbf{x}_h)}_{M_h}=\left(\varphi^{\mathrm{H}(\mathbf{x}_h)}_{x,M_h},\varphi^{\mathrm{H}(\mathbf{x}_h)}_{z,M_h}\right)^{\mathrm{T}}$ with $h = 1, \ldots, 4$ and $M_h = M_h(\beta, n)$ indicate that they are constructed over the H-cell in which the coarse-scale boundary node (vertex) $\mathbf{x}_h$ of an ε-cell locates, while $\varphi^{\varepsilon}_{\alpha,m}$

with $m = 1, \ldots, 8$ are constructed over $I^{\varepsilon}_{i\pm1/2,j}$ and $I^{\varepsilon}_{i,j\pm1/2}$ for computing $\mathbf{c}_n^{\pm}(\boldsymbol{\xi},\omega)$ and $\mathbf{d}_n^{\pm}(\boldsymbol{\xi},\omega)$, respectively. Using Eq. (A.5)–(A.9), we can obtain all coefficients in the coupling coefficient matrices by assigning different values for some parameters.

For $I^{\varepsilon}_{i\pm1/2,j}$, we have $\varpi_{n,\alpha\beta}(\boldsymbol{\xi},\omega) = c^{\pm}_{n,\alpha\beta}(\boldsymbol{\xi},\omega)$ with

$$\begin{cases} \varpi^{\mathbf{x}_1}_{n,\alpha\beta}(\boldsymbol{\xi},\omega) = \varpi^{\mathbf{x}_2}_{n,\alpha\beta}(\boldsymbol{\xi},\omega) = 0, & \text{if } n = 5,6, \\ \varpi^{\mathbf{x}_3}_{n,\alpha\beta}(\boldsymbol{\xi},\omega) = \varpi^{\mathbf{x}_4}_{n,\alpha\beta}(\boldsymbol{\xi},\omega) = 0, & \text{if } n = 1,2, \end{cases} \tag{A.10}$$

$$\begin{cases} M_1(\beta = x, n) = M_2(\beta = x, n) = n, & M_1(\beta = z, n) = M_2(\beta = z, n) = n + 4, & n = 1, \cdots, 4, \\ M_3(\beta = x, n) = M_4(\beta = x, n) = n - 2, & M_3(\beta = z, n) = M_4(\beta = z, n) = n + 2, & n = 3, \cdots, 6, \end{cases} \tag{A.11}$$

$$\boldsymbol{\varphi}^{\mathrm{H}(\mathbf{x}_1)}_{M_1} = \boldsymbol{\varphi}^{\mathrm{H}(\mathbf{x}_2)}_{M_2} = \left[\boldsymbol{\varphi}_{M_1}\right]_{I^{\mathrm{H}}_{i\pm1/2,j-1/2}}, \boldsymbol{\varphi}^{\mathrm{H}(\mathbf{x}_3)}_{M_3} = \boldsymbol{\varphi}^{\mathrm{H}(\mathbf{x}_4)}_{M_4} = \left[\boldsymbol{\varphi}_{M_3}\right]_{I^{\mathrm{H}}_{i\pm1/2,j+1/2}}, \tag{A.12}$$

where $[\cdot]_{I^{\mathrm{H}}_{i\pm1/2,j-1/2}}$ and $[\cdot]_{I^{\mathrm{H}}_{i\pm1/2,j+1/2}}$ indicate that the variables in the bracket are obtained within the H-cells of $I^{\mathrm{H}}_{i\pm1/2,j-1/2}$ and $I^{\mathrm{H}}_{i\pm1/2,j+1/2}$, respectively.

For $I^{\varepsilon}_{i,j\pm1/2}$, we have $\varpi_{n,\alpha\beta}(\boldsymbol{\xi},\omega) = d^{\pm}_{n,\alpha\beta}(\boldsymbol{\xi},\omega)$ with

$$\begin{cases} \varpi^{\mathbf{x}_1}_{n,\alpha\beta}(\boldsymbol{\xi},\omega) = \varpi^{\mathbf{x}_3}_{n,\alpha\beta}(\boldsymbol{\xi},\omega) = 0, & \text{if } n = 3,6, \\ \varpi^{\mathbf{x}_2}_{n,\alpha\beta}(\boldsymbol{\xi},\omega) = \varpi^{\mathbf{x}_4}_{n,\alpha\beta}(\boldsymbol{\xi},\omega) = 0, & \text{if } n = 1,4, \end{cases} \tag{A.13}$$

$$\begin{cases} M_1(\beta = x, n) = M_3(\beta = x, n) = n, & M_1(\beta = z, n) = M_3(\beta = z, n) = n + 4, & n = 1,2, \\ M_1(\beta = x, n) = M_3(\beta = x, n) = n - 1, & M_1(\beta = z, n) = M_3(\beta = z, n) = n + 3, & n = 4,5, \\ M_2(\beta = x, n) = M_4(\beta = x, n) = n - 1, & M_2(\beta = z, n) = M_4(\beta = z, n) = n + 3, & n = 2,3, \\ M_2(\beta = x, n) = M_4(\beta = x, n) = n - 2, & M_2(\beta = z, n) = M_4(\beta = z, n) = n + 2, & n = 5,6, \end{cases} \tag{A.14}$$

$$\boldsymbol{\varphi}^{\mathrm{H}(\mathbf{x}_1)}_{M_1} = \boldsymbol{\varphi}^{\mathrm{H}(\mathbf{x}_3)}_{M_3} = \left[\boldsymbol{\varphi}_{M_1}\right]_{I^{\mathrm{H}}_{i-1/2,j\pm1/2}}, \boldsymbol{\varphi}^{\mathrm{H}(\mathbf{x}_2)}_{M_2} = \boldsymbol{\varphi}^{\mathrm{H}(\mathbf{x}_4)}_{M_4} = \left[\boldsymbol{\varphi}_{M_2}\right]_{I^{\mathrm{H}}_{i+1/2,j\pm1/2}}. \tag{A.15}$$

Note that it is unnecessary to determine M_h with $h = 1, \ldots, 4$ in Eq. (A.11) and (A.14) when $\varpi^{\mathbf{x}_h}_{n,\alpha\beta}(\boldsymbol{\xi},\omega) = 0$.

Appendix B. Coefficient matrices of the coarse-scale FD stencil

We define the coefficient matrices in Eq. (22) as

$$\mathbf{A}^{i,j}_n = \begin{bmatrix} \mathbf{A}^{i,j}_{n,x} \\ \mathbf{A}^{i,j}_{n,z} \end{bmatrix} = \begin{bmatrix} A^{i,j}_{n,xx} & A^{i,j}_{n,xz} \\ A^{i,j}_{n,zx} & A^{i,j}_{n,zz} \end{bmatrix}, n = 1, \cdots, 21. \tag{B.1}$$

For the eight-flux-based fourth-order FD stencil, we define $\mathbf{c}_n^{(1)+}$, $\mathbf{c}_n^{(-1)-}$, $\mathbf{d}_n^{(1)+}$, and $\mathbf{d}_n^{(-1)-}$ with $n = 1, \ldots, 6$ as the coupling coefficient matrices of fine-scale wavefield solutions within $I^{\varepsilon}_{i+3/2,j}$, $I^{\varepsilon}_{i-3/2,j}$, $I^{\varepsilon}_{i,j+3/2}$, and $I^{\varepsilon}_{i,j-3/2}$, respectively. We can obtain $\mathbf{c}_n^{(\pm1)\pm}$ with $n = 1, \ldots, 6$ by replacing i with $i \pm 1$ in Appendix A during their computation. Similarly, $\mathbf{d}_n^{(\pm1)\pm}$ with $n = 1, \ldots, 6$ are computed by substituting $j\pm1$ for j in Appendix A. Therefore, the PML-related coefficient matrices in Eq. (22) are specifically given by

$$\mathbf{A}_{(n=1,2,3),x}^{i,j}=\frac{1}{24\Delta z(\zeta_z)^j\left|I_{i,j-3/2}^{\varepsilon}\right|}\iint_{I_{i,j-3/2}^{\varepsilon}}\left[\frac{C_{55}}{\zeta_z}\frac{\partial\mathbf{d}_{n,x}^{(-1)-}(\boldsymbol{\xi},\omega)}{\partial z}+\frac{C_{55}}{\zeta_x}\frac{\partial\mathbf{d}_{n,z}^{(-1)-}(\boldsymbol{\xi},\omega)}{\partial x}\right]\mathrm{d}x\mathrm{d}z, \tag{B.2a}$$

$$\mathbf{A}_{(n=1,2,3),z}^{i,j}=\frac{1}{24\Delta z(\zeta_z)^j\left|I_{i,j-3/2}^{\varepsilon}\right|}\iint_{I_{i,j-3/2}^{\varepsilon}}\left[\frac{C_{13}}{\zeta_x}\frac{\partial\mathbf{d}_{n,x}^{(-1)-}(\boldsymbol{\xi},\omega)}{\partial x}+\frac{C_{33}}{\zeta_z}\frac{\partial\mathbf{d}_{n,z}^{(-1)-}(\boldsymbol{\xi},\omega)}{\partial z}\right]\mathrm{d}x\mathrm{d}z, \tag{B.2b}$$

$$\mathbf{A}_{(n=4,9,14),x}^{i,j}=\frac{1}{24\Delta x(\zeta_x)^i\left|I_{i-3/2,j}^{\varepsilon}\right|}\iint_{I_{i-3/2,j}^{\varepsilon}}\left[\frac{C_{11}}{\zeta_x}\frac{\partial\mathbf{c}_{(2n-3)/5,x}^{(-1)-}(\boldsymbol{\xi},\omega)}{\partial x}+\frac{C_{13}}{\zeta_z}\frac{\partial\mathbf{c}_{(2n-3)/5,z}^{(-1)-}(\boldsymbol{\xi},\omega)}{\partial z}\right]\mathrm{d}x\mathrm{d}z, \tag{B.3a}$$

$$\mathbf{A}_{(n=4,9,14),z}^{i,j}=\frac{1}{24\Delta x(\zeta_x)^i\left|I_{i-3/2,j}^{\varepsilon}\right|}\iint_{I_{i-3/2,j}^{\varepsilon}}\left[\frac{C_{55}}{\zeta_z}\frac{\partial\mathbf{c}_{(2n-3)/5,x}^{(-1)-}(\boldsymbol{\xi},\omega)}{\partial z}+\frac{C_{55}}{\zeta_x}\frac{\partial\mathbf{c}_{(2n-3)/5,z}^{(-1)-}(\boldsymbol{\xi},\omega)}{\partial x}\right]\mathrm{d}x\mathrm{d}z, \tag{B.3b}$$

$$\begin{aligned}
\mathbf{A}_{5,x}^{i,j}=&-\frac{9}{8\Delta x(\zeta_x)^i\left|I_{i-1/2,j}^{\varepsilon}\right|}\iint_{I_{i-1/2,j}^{\varepsilon}}\left[\frac{C_{11}}{\zeta_x}\frac{\partial\mathbf{c}_{1,x}^{-}(\boldsymbol{\xi},\omega)}{\partial x}+\frac{C_{13}}{\zeta_z}\frac{\partial\mathbf{c}_{1,z}^{-}(\boldsymbol{\xi},\omega)}{\partial z}\right]\mathrm{d}x\mathrm{d}z\\
&+\frac{1}{24\Delta x(\zeta_x)^i\left|I_{i-3/2,j}^{\varepsilon}\right|}\iint_{I_{i-3/2,j}^{\varepsilon}}\left[\frac{C_{11}}{\zeta_x}\frac{\partial\mathbf{c}_{2,x}^{(-1)-}(\boldsymbol{\xi},\omega)}{\partial x}+\frac{C_{13}}{\zeta_z}\frac{\partial\mathbf{c}_{2,z}^{(-1)-}(\boldsymbol{\xi},\omega)}{\partial z}\right]\mathrm{d}x\mathrm{d}z\\
&-\frac{9}{8\Delta z(\zeta_z)^j\left|I_{i,j-1/2}^{\varepsilon}\right|}\iint_{I_{i,j-1/2}^{\varepsilon}}\left[\frac{C_{55}}{\zeta_z}\frac{\partial\mathbf{d}_{1,x}^{-}(\boldsymbol{\xi},\omega)}{\partial z}+\frac{C_{55}}{\zeta_x}\frac{\partial\mathbf{d}_{1,z}^{-}(\boldsymbol{\xi},\omega)}{\partial x}\right]\mathrm{d}x\mathrm{d}z\\
&+\frac{1}{24\Delta z(\zeta_z)^j\left|I_{i,j-3/2}^{\varepsilon}\right|}\iint_{I_{i,j-3/2}^{\varepsilon}}\left[\frac{C_{55}}{\zeta_z}\frac{\partial\mathbf{d}_{4,x}^{(-1)-}(\boldsymbol{\xi},\omega)}{\partial z}+\frac{C_{55}}{\zeta_x}\frac{\partial\mathbf{d}_{4,z}^{(-1)-}(\boldsymbol{\xi},\omega)}{\partial x}\right]\mathrm{d}x\mathrm{d}z,
\end{aligned} \tag{B.4a}$$

$$\begin{aligned}
\mathbf{A}_{5,z}^{i,j}=&-\frac{9}{8\Delta x(\zeta_x)^i\left|I_{i-1/2,j}^{\varepsilon}\right|}\iint_{I_{i-1/2,j}^{\varepsilon}}\left[\frac{C_{55}}{\zeta_z}\frac{\partial\mathbf{c}_{1,x}^{-}(\boldsymbol{\xi},\omega)}{\partial z}+\frac{C_{55}}{\zeta_x}\frac{\partial\mathbf{c}_{1,z}^{-}(\boldsymbol{\xi},\omega)}{\partial x}\right]\mathrm{d}x\mathrm{d}z\\
&+\frac{1}{24\Delta x(\zeta_x)^i\left|I_{i-3/2,j}^{\varepsilon}\right|}\iint_{I_{i-3/2,j}^{\varepsilon}}\left[\frac{C_{55}}{\zeta_z}\frac{\partial\mathbf{c}_{2,x}^{(-1)-}(\boldsymbol{\xi},\omega)}{\partial z}+\frac{C_{55}}{\zeta_x}\frac{\partial\mathbf{c}_{2,z}^{(-1)-}(\boldsymbol{\xi},\omega)}{\partial x}\right]\mathrm{d}x\mathrm{d}z\\
&-\frac{9}{8\Delta z(\zeta_z)^j\left|I_{i,j-1/2}^{\varepsilon}\right|}\iint_{I_{i,j-1/2}^{\varepsilon}}\left[\frac{C_{13}}{\zeta_x}\frac{\partial\mathbf{d}_{1,x}^{-}(\boldsymbol{\xi},\omega)}{\partial x}+\frac{C_{33}}{\zeta_z}\frac{\partial\mathbf{d}_{1,z}^{-}(\boldsymbol{\xi},\omega)}{\partial z}\right]\mathrm{d}x\mathrm{d}z\\
&+\frac{1}{24\Delta z(\zeta_z)^j\left|I_{i,j-3/2}^{\varepsilon}\right|}\iint_{I_{i,j-3/2}^{\varepsilon}}\left[\frac{C_{13}}{\zeta_x}\frac{\partial\mathbf{d}_{4,x}^{(-1)-}(\boldsymbol{\xi},\omega)}{\partial x}+\frac{C_{33}}{\zeta_z}\frac{\partial\mathbf{d}_{4,z}^{(-1)-}(\boldsymbol{\xi},\omega)}{\partial z}\right]\mathrm{d}x\mathrm{d}z,
\end{aligned} \tag{B.4b}$$

$$\begin{aligned}
\mathbf{A}_{6,x}^{i,j}=&\frac{9}{8\Delta x(\zeta_x)^i\left|I_{i+1/2,j}^{\varepsilon}\right|}\iint_{I_{i+1/2,j}^{\varepsilon}}\left[\frac{C_{11}}{\zeta_x}\frac{\partial\mathbf{c}_{1,x}^{+}(\boldsymbol{\xi},\omega)}{\partial x}+\frac{C_{13}}{\zeta_z}\frac{\partial\mathbf{c}_{1,z}^{+}(\boldsymbol{\xi},\omega)}{\partial z}\right]\mathrm{d}x\mathrm{d}z\\
&-\frac{9}{8\Delta x(\zeta_x)^i\left|I_{i-1/2,j}^{\varepsilon}\right|}\iint_{I_{i-1/2,j}^{\varepsilon}}\left[\frac{C_{11}}{\zeta_x}\frac{\partial\mathbf{c}_{2,x}^{-}(\boldsymbol{\xi},\omega)}{\partial x}+\frac{C_{13}}{\zeta_z}\frac{\partial\mathbf{c}_{2,z}^{-}(\boldsymbol{\xi},\omega)}{\partial z}\right]\mathrm{d}x\mathrm{d}z\\
&-\frac{9}{8\Delta z(\zeta_z)^j\left|I_{i,j-1/2}^{\varepsilon}\right|}\iint_{I_{i,j-1/2}^{\varepsilon}}\left[\frac{C_{55}}{\zeta_z}\frac{\partial\mathbf{d}_{2,x}^{-}(\boldsymbol{\xi},\omega)}{\partial z}+\frac{C_{55}}{\zeta_x}\frac{\partial\mathbf{d}_{2,z}^{-}(\boldsymbol{\xi},\omega)}{\partial x}\right]\mathrm{d}x\mathrm{d}z\\
&+\frac{1}{24\Delta z(\zeta_z)^j\left|I_{i,j-3/2}^{\varepsilon}\right|}\iint_{I_{i,j-3/2}^{\varepsilon}}\left[\frac{C_{55}}{\zeta_z}\frac{\partial\mathbf{d}_{5,x}^{(-1)-}(\boldsymbol{\xi},\omega)}{\partial z}+\frac{C_{55}}{\zeta_x}\frac{\partial\mathbf{d}_{5,z}^{(-1)-}(\boldsymbol{\xi},\omega)}{\partial x}\right]\mathrm{d}x\mathrm{d}z,
\end{aligned} \tag{B.5a}$$

$$\begin{aligned}
\mathbf{A}_{6,z}^{i,j} = & \frac{9}{8\Delta x(\zeta_x)^i \left| I_{i+1/2,j}^{\varepsilon} \right|} \iint_{I_{i+1/2,j}^{\varepsilon}} \left[\frac{C_{55}}{\zeta_z} \frac{\partial \mathbf{c}_{1,x}^{+}(\boldsymbol{\xi},\omega)}{\partial z} + \frac{C_{55}}{\zeta_x} \frac{\partial \mathbf{c}_{1,z}^{+}(\boldsymbol{\xi},\omega)}{\partial x} \right] \mathrm{d}x\mathrm{d}z \\
& - \frac{9}{8\Delta x(\zeta_x)^i \left| I_{i-1/2,j}^{\varepsilon} \right|} \iint_{I_{i-1/2,j}^{\varepsilon}} \left[\frac{C_{55}}{\zeta_z} \frac{\partial \mathbf{c}_{2,x}^{-}(\boldsymbol{\xi},\omega)}{\partial z} + \frac{C_{55}}{\zeta_x} \frac{\partial \mathbf{c}_{2,z}^{-}(\boldsymbol{\xi},\omega)}{\partial x} \right] \mathrm{d}x\mathrm{d}z \\
& - \frac{9}{8\Delta z(\zeta_z)^j \left| I_{i,j-1/2}^{\varepsilon} \right|} \iint_{I_{i,j-1/2}^{\varepsilon}} \left[\frac{C_{13}}{\zeta_x} \frac{\partial \mathbf{d}_{2,x}^{-}(\boldsymbol{\xi},\omega)}{\partial x} + \frac{C_{33}}{\zeta_z} \frac{\partial \mathbf{d}_{2,z}^{-}(\boldsymbol{\xi},\omega)}{\partial z} \right] \mathrm{d}x\mathrm{d}z \\
& + \frac{1}{24\Delta z(\zeta_z)^j \left| I_{i,j-3/2}^{\varepsilon} \right|} \iint_{I_{i,j-3/2}^{\varepsilon}} \left[\frac{C_{13}}{\zeta_x} \frac{\partial \mathbf{d}_{5,x}^{(-1)-}(\boldsymbol{\xi},\omega)}{\partial x} + \frac{C_{33}}{\zeta_z} \frac{\partial \mathbf{d}_{5,z}^{(-1)-}(\boldsymbol{\xi},\omega)}{\partial z} \right] \mathrm{d}x\mathrm{d}z,
\end{aligned} \tag{B.5b}$$

$$\begin{aligned}
\mathbf{A}_{7,x}^{i,j} = & \frac{9}{8\Delta x(\zeta_x)^i \left| I_{i+1/2,j}^{\varepsilon} \right|} \iint_{I_{i+1/2,j}^{\varepsilon}} \left[\frac{C_{11}}{\zeta_x} \frac{\partial \mathbf{c}_{2,x}^{+}(\boldsymbol{\xi},\omega)}{\partial x} + \frac{C_{13}}{\zeta_z} \frac{\partial \mathbf{c}_{2,z}^{+}(\boldsymbol{\xi},\omega)}{\partial z} \right] \mathrm{d}x\mathrm{d}z \\
& - \frac{1}{24\Delta x(\zeta_x)^i \left| I_{i+3/2,j}^{\varepsilon} \right|} \iint_{I_{i+3/2,j}^{\varepsilon}} \left[\frac{C_{11}}{\zeta_x} \frac{\partial \mathbf{c}_{1,x}^{(1)+}(\boldsymbol{\xi},\omega)}{\partial x} + \frac{C_{13}}{\zeta_z} \frac{\partial \mathbf{c}_{1,z}^{(1)+}(\boldsymbol{\xi},\omega)}{\partial z} \right] \mathrm{d}x\mathrm{d}z \\
& - \frac{9}{8\Delta z(\zeta_z)^j \left| I_{i,j-1/2}^{\varepsilon} \right|} \iint_{I_{i,j-1/2}^{\varepsilon}} \left[\frac{C_{55}}{\zeta_z} \frac{\partial \mathbf{d}_{3,x}^{-}(\boldsymbol{\xi},\omega)}{\partial z} + \frac{C_{55}}{\zeta_x} \frac{\partial \mathbf{d}_{3,z}^{-}(\boldsymbol{\xi},\omega)}{\partial x} \right] \mathrm{d}x\mathrm{d}z \\
& + \frac{1}{24\Delta z(\zeta_z)^j \left| I_{i,j-3/2}^{\varepsilon} \right|} \iint_{I_{i,j-3/2}^{\varepsilon}} \left[\frac{C_{55}}{\zeta_z} \frac{\partial \mathbf{d}_{6,x}^{(-1)-}(\boldsymbol{\xi},\omega)}{\partial z} + \frac{C_{55}}{\zeta_x} \frac{\partial \mathbf{d}_{6,z}^{(-1)-}(\boldsymbol{\xi},\omega)}{\partial x} \right] \mathrm{d}x\mathrm{d}z,
\end{aligned} \tag{B.6a}$$

$$\begin{aligned}
\mathbf{A}_{7,z}^{i,j} = & \frac{9}{8\Delta x(\zeta_x)^i \left| I_{i+1/2,j}^{\varepsilon} \right|} \iint_{I_{i+1/2,j}^{\varepsilon}} \left[\frac{C_{55}}{\zeta_z} \frac{\partial \mathbf{c}_{2,x}^{+}(\boldsymbol{\xi},\omega)}{\partial z} + \frac{C_{55}}{\zeta_x} \frac{\partial \mathbf{c}_{2,z}^{+}(\boldsymbol{\xi},\omega)}{\partial x} \right] \mathrm{d}x\mathrm{d}z \\
& - \frac{1}{24\Delta x(\zeta_x)^i \left| I_{i+3/2,j}^{\varepsilon} \right|} \iint_{I_{i+3/2,j}^{\varepsilon}} \left[\frac{C_{55}}{\zeta_z} \frac{\partial \mathbf{c}_{1,x}^{(1)+}(\boldsymbol{\xi},\omega)}{\partial z} + \frac{C_{55}}{\zeta_x} \frac{\partial \mathbf{c}_{1,z}^{(1)+}(\boldsymbol{\xi},\omega)}{\partial x} \right] \mathrm{d}x\mathrm{d}z \\
& - \frac{9}{8\Delta z(\zeta_z)^j \left| I_{i,j-1/2}^{\varepsilon} \right|} \iint_{I_{i,j-1/2}^{\varepsilon}} \left[\frac{C_{13}}{\zeta_x} \frac{\partial \mathbf{d}_{3,x}^{-}(\boldsymbol{\xi},\omega)}{\partial x} + \frac{C_{33}}{\zeta_z} \frac{\partial \mathbf{d}_{3,z}^{-}(\boldsymbol{\xi},\omega)}{\partial z} \right] \mathrm{d}x\mathrm{d}z \\
& + \frac{1}{24\Delta z(\zeta_z)^j \left| I_{i,j-3/2}^{\varepsilon} \right|} \iint_{I_{i,j-3/2}^{\varepsilon}} \left[\frac{C_{13}}{\zeta_x} \frac{\partial \mathbf{d}_{6,x}^{(-1)-}(\boldsymbol{\xi},\omega)}{\partial x} + \frac{C_{33}}{\zeta_z} \frac{\partial \mathbf{d}_{6,z}^{(-1)-}(\boldsymbol{\xi},\omega)}{\partial z} \right] \mathrm{d}x\mathrm{d}z,
\end{aligned} \tag{B.6b}$$

$$\begin{aligned}
\mathbf{A}_{10,x}^{i,j} = & -\frac{9}{8\Delta x(\zeta_x)^i \left| I_{i-1/2,j}^{\varepsilon} \right|} \iint_{I_{i-1/2,j}^{\varepsilon}} \left[\frac{C_{11}}{\zeta_x} \frac{\partial \mathbf{c}_{3,x}^{-}(\boldsymbol{\xi},\omega)}{\partial x} + \frac{C_{13}}{\zeta_z} \frac{\partial \mathbf{c}_{3,z}^{-}(\boldsymbol{\xi},\omega)}{\partial z} \right] \mathrm{d}x\mathrm{d}z \\
& + \frac{1}{24\Delta x(\zeta_x)^i \left| I_{i-3/2,j}^{\varepsilon} \right|} \iint_{I_{i-3/2,j}^{\varepsilon}} \left[\frac{C_{11}}{\zeta_x} \frac{\partial \mathbf{c}_{4,x}^{(-1)-}(\boldsymbol{\xi},\omega)}{\partial x} + \frac{C_{13}}{\zeta_z} \frac{\partial \mathbf{c}_{4,z}^{(-1)-}(\boldsymbol{\xi},\omega)}{\partial z} \right] \mathrm{d}x\mathrm{d}z \\
& + \frac{9}{8\Delta z(\zeta_z)^j \left| I_{i,j+1/2}^{\varepsilon} \right|} \iint_{I_{i,j+1/2}^{\varepsilon}} \left[\frac{C_{55}}{\zeta_z} \frac{\partial \mathbf{d}_{1,x}^{+}(\boldsymbol{\xi},\omega)}{\partial z} + \frac{C_{55}}{\zeta_x} \frac{\partial \mathbf{d}_{1,z}^{+}(\boldsymbol{\xi},\omega)}{\partial x} \right] \mathrm{d}x\mathrm{d}z \\
& - \frac{9}{8\Delta z(\zeta_z)^j \left| I_{i,j-1/2}^{\varepsilon} \right|} \iint_{I_{i,j-1/2}^{\varepsilon}} \left[\frac{C_{55}}{\zeta_z} \frac{\partial \mathbf{d}_{4,x}^{-}(\boldsymbol{\xi},\omega)}{\partial z} + \frac{C_{55}}{\zeta_x} \frac{\partial \mathbf{d}_{4,z}^{-}(\boldsymbol{\xi},\omega)}{\partial x} \right] \mathrm{d}x\mathrm{d}z,
\end{aligned} \tag{B.7a}$$

$$\begin{aligned}
\mathbf{A}_{10,z}^{i,j} = & -\frac{9}{8\Delta x(\zeta_x)^i \left| I_{i-1/2,j}^{\varepsilon} \right|} \iint_{I_{i-1/2,j}^{\varepsilon}} \left[\frac{C_{55}}{\zeta_z} \frac{\partial \mathbf{c}_{3,x}^{-}(\boldsymbol{\xi},\omega)}{\partial z} + \frac{C_{55}}{\zeta_x} \frac{\partial \mathbf{c}_{3,z}^{-}(\boldsymbol{\xi},\omega)}{\partial x} \right] \mathrm{d}x\mathrm{d}z \\
& + \frac{1}{24\Delta x(\zeta_x)^i \left| I_{i-3/2,j}^{\varepsilon} \right|} \iint_{I_{i-3/2,j}^{\varepsilon}} \left[\frac{C_{55}}{\zeta_z} \frac{\partial \mathbf{c}_{4,x}^{(-1)-}(\boldsymbol{\xi},\omega)}{\partial z} + \frac{C_{55}}{\zeta_x} \frac{\partial \mathbf{c}_{4,z}^{(-1)-}(\boldsymbol{\xi},\omega)}{\partial x} \right] \mathrm{d}x\mathrm{d}z \\
& + \frac{9}{8\Delta z(\zeta_z)^j \left| I_{i,j+1/2}^{\varepsilon} \right|} \iint_{I_{i,j+1/2}^{\varepsilon}} \left[\frac{C_{13}}{\zeta_x} \frac{\partial \mathbf{d}_{1,x}^{+}(\boldsymbol{\xi},\omega)}{\partial x} + \frac{C_{33}}{\zeta_z} \frac{\partial \mathbf{d}_{1,z}^{+}(\boldsymbol{\xi},\omega)}{\partial z} \right] \mathrm{d}x\mathrm{d}z \\
& - \frac{9}{8\Delta z(\zeta_z)^j \left| I_{i,j-1/2}^{\varepsilon} \right|} \iint_{I_{i,j-1/2}^{\varepsilon}} \left[\frac{C_{13}}{\zeta_x} \frac{\partial \mathbf{d}_{4,x}^{-}(\boldsymbol{\xi},\omega)}{\partial x} + \frac{C_{33}}{\zeta_z} \frac{\partial \mathbf{d}_{4,z}^{-}(\boldsymbol{\xi},\omega)}{\partial z} \right] \mathrm{d}x\mathrm{d}z,
\end{aligned} \tag{B.7b}$$

$$\begin{aligned}\mathbf{A}_{11,x}^{i,j}=\mathbf{D}_x&+\frac{9}{8\Delta x(\zeta_x)^i\left|I_{i+1/2,j}^{\varepsilon}\right|}\iint_{I_{i+1/2,j}^{\varepsilon}}\left[\frac{C_{11}}{\zeta_x}\frac{\partial\mathbf{c}_{3,x}^{+}(\boldsymbol{\xi},\omega)}{\partial x}+\frac{C_{13}}{\zeta_z}\frac{\partial\mathbf{c}_{3,z}^{+}(\boldsymbol{\xi},\omega)}{\partial z}\right]\mathrm{d}x\mathrm{d}z\\&-\frac{9}{8\Delta x(\zeta_x)^i\left|I_{i-1/2,j}^{\varepsilon}\right|}\iint_{I_{i-1/2,j}^{\varepsilon}}\left[\frac{C_{11}}{\zeta_x}\frac{\partial\mathbf{c}_{4,x}^{-}(\boldsymbol{\xi},\omega)}{\partial x}+\frac{C_{13}}{\zeta_z}\frac{\partial\mathbf{c}_{4,z}^{-}(\boldsymbol{\xi},\omega)}{\partial z}\right]\mathrm{d}x\mathrm{d}z\\&+\frac{9}{8\Delta z(\zeta_z)^j\left|I_{i,j+1/2}^{\varepsilon}\right|}\iint_{I_{i,j+1/2}^{\varepsilon}}\left[\frac{C_{55}}{\zeta_z}\frac{\partial\mathbf{d}_{2,x}^{+}(\boldsymbol{\xi},\omega)}{\partial z}+\frac{C_{55}}{\zeta_x}\frac{\partial\mathbf{d}_{2,z}^{+}(\boldsymbol{\xi},\omega)}{\partial x}\right]\mathrm{d}x\mathrm{d}z\\&-\frac{9}{8\Delta z(\zeta_z)^j\left|I_{i,j-1/2}^{\varepsilon}\right|}\iint_{I_{i,j-1/2}^{\varepsilon}}\left[\frac{C_{55}}{\zeta_z}\frac{\partial\mathbf{d}_{5,x}^{-}(\boldsymbol{\xi},\omega)}{\partial z}+\frac{C_{55}}{\zeta_x}\frac{\partial\mathbf{d}_{5,z}^{-}(\boldsymbol{\xi},\omega)}{\partial x}\right]\mathrm{d}x\mathrm{d}z,\end{aligned}\tag{B.8a}$$

$$\begin{aligned}\mathbf{A}_{11,z}^{i,j}=\mathbf{D}_z&+\frac{9}{8\Delta x(\zeta_x)^i\left|I_{i+1/2,j}^{\varepsilon}\right|}\iint_{I_{i+1/2,j}^{\varepsilon}}\left[\frac{C_{55}}{\zeta_z}\frac{\partial\mathbf{c}_{3,x}^{+}(\boldsymbol{\xi},\omega)}{\partial z}+\frac{C_{55}}{\zeta_x}\frac{\partial\mathbf{c}_{3,z}^{+}(\boldsymbol{\xi},\omega)}{\partial x}\right]\mathrm{d}x\mathrm{d}z\\&-\frac{9}{8\Delta x(\zeta_x)^i\left|I_{i-1/2,j}^{\varepsilon}\right|}\iint_{I_{i-1/2,j}^{\varepsilon}}\left[\frac{C_{55}}{\zeta_z}\frac{\partial\mathbf{c}_{4,x}^{-}(\boldsymbol{\xi},\omega)}{\partial z}+\frac{C_{55}}{\zeta_x}\frac{\partial\mathbf{c}_{4,z}^{-}(\boldsymbol{\xi},\omega)}{\partial x}\right]\mathrm{d}x\mathrm{d}z\\&+\frac{9}{8\Delta z(\zeta_z)^j\left|I_{i,j+1/2}^{\varepsilon}\right|}\iint_{I_{i,j+1/2}^{\varepsilon}}\left[\frac{C_{13}}{\zeta_x}\frac{\partial\mathbf{d}_{2,x}^{+}(\boldsymbol{\xi},\omega)}{\partial x}+\frac{C_{33}}{\zeta_z}\frac{\partial\mathbf{d}_{2,z}^{+}(\boldsymbol{\xi},\omega)}{\partial z}\right]\mathrm{d}x\mathrm{d}z\\&-\frac{9}{8\Delta z(\zeta_z)^j\left|I_{i,j-1/2}^{\varepsilon}\right|}\iint_{I_{i,j-1/2}^{\varepsilon}}\left[\frac{C_{13}}{\zeta_x}\frac{\partial\mathbf{d}_{5,x}^{-}(\boldsymbol{\xi},\omega)}{\partial x}+\frac{C_{33}}{\zeta_z}\frac{\partial\mathbf{d}_{5,z}^{-}(\boldsymbol{\xi},\omega)}{\partial z}\right]\mathrm{d}x\mathrm{d}z,\end{aligned}\tag{B.8b}$$

$$\begin{aligned}\mathbf{A}_{12,x}^{i,j}=&\frac{9}{8\Delta x(\zeta_x)^i\left|I_{i+1/2,j}^{\varepsilon}\right|}\iint_{I_{i+1/2,j}^{\varepsilon}}\left[\frac{C_{11}}{\zeta_x}\frac{\partial\mathbf{c}_{4,x}^{+}(\boldsymbol{\xi},\omega)}{\partial x}+\frac{C_{13}}{\zeta_z}\frac{\partial\mathbf{c}_{4,z}^{+}(\boldsymbol{\xi},\omega)}{\partial z}\right]\mathrm{d}x\mathrm{d}z\\&-\frac{1}{24\Delta x(\zeta_x)^i\left|I_{i+3/2,j}^{\varepsilon}\right|}\iint_{I_{i+3/2,j}^{\varepsilon}}\left[\frac{C_{11}}{\zeta_x}\frac{\partial\mathbf{c}_{3,x}^{(1)+}(\boldsymbol{\xi},\omega)}{\partial x}+\frac{C_{13}}{\zeta_z}\frac{\partial\mathbf{c}_{3,z}^{(1)+}(\boldsymbol{\xi},\omega)}{\partial z}\right]\mathrm{d}x\mathrm{d}z\\&+\frac{9}{8\Delta z(\zeta_z)^j\left|I_{i,j+1/2}^{\varepsilon}\right|}\iint_{I_{i,j+1/2}^{\varepsilon}}\left[\frac{C_{55}}{\zeta_z}\frac{\partial\mathbf{d}_{3,x}^{+}(\boldsymbol{\xi},\omega)}{\partial z}+\frac{C_{55}}{\zeta_x}\frac{\partial\mathbf{d}_{3,z}^{+}(\boldsymbol{\xi},\omega)}{\partial x}\right]\mathrm{d}x\mathrm{d}z\\&-\frac{9}{8\Delta z(\zeta_z)^j\left|I_{i,j-1/2}^{\varepsilon}\right|}\iint_{I_{i,j-1/2}^{\varepsilon}}\left[\frac{C_{55}}{\zeta_z}\frac{\partial\mathbf{d}_{6,x}^{-}(\boldsymbol{\xi},\omega)}{\partial z}+\frac{C_{55}}{\zeta_x}\frac{\partial\mathbf{d}_{6,z}^{-}(\boldsymbol{\xi},\omega)}{\partial x}\right]\mathrm{d}x\mathrm{d}z,\end{aligned}\tag{B.9a}$$

$$\begin{aligned}\mathbf{A}_{12,z}^{i,j}=&\frac{9}{8\Delta x(\zeta_x)^i\left|I_{i+1/2,j}^{\varepsilon}\right|}\iint_{I_{i+1/2,j}^{\varepsilon}}\left[\frac{C_{55}}{\zeta_z}\frac{\partial\mathbf{c}_{4,x}^{+}(\boldsymbol{\xi},\omega)}{\partial z}+\frac{C_{55}}{\zeta_x}\frac{\partial\mathbf{c}_{4,x}^{+}(\boldsymbol{\xi},\omega)}{\partial x}\right]\mathrm{d}x\mathrm{d}z\\&-\frac{1}{24\Delta x(\zeta_x)^i\left|I_{i+3/2,j}^{\varepsilon}\right|}\iint_{I_{i+3/2,j}^{\varepsilon}}\left[\frac{C_{55}}{\zeta_z}\frac{\partial\mathbf{c}_{3,x}^{(1)+}(\boldsymbol{\xi},\omega)}{\partial z}+\frac{C_{55}}{\zeta_x}\frac{\partial\mathbf{c}_{3,z}^{(1)+}(\boldsymbol{\xi},\omega)}{\partial x}\right]\mathrm{d}x\mathrm{d}z\\&+\frac{9}{8\Delta z(\zeta_z)^j\left|I_{i,j+1/2}^{\varepsilon}\right|}\iint_{I_{i,j+1/2}^{\varepsilon}}\left[\frac{C_{13}}{\zeta_x}\frac{\partial\mathbf{d}_{3,x}^{+}(\boldsymbol{\xi},\omega)}{\partial x}+\frac{C_{33}}{\zeta_z}\frac{\partial\mathbf{d}_{3,z}^{+}(\boldsymbol{\xi},\omega)}{\partial z}\right]\mathrm{d}x\mathrm{d}z\\&-\frac{9}{8\Delta z(\zeta_z)^j\left|I_{i,j-1/2}^{\varepsilon}\right|}\iint_{I_{i,j-1/2}^{\varepsilon}}\left[\frac{C_{13}}{\zeta_x}\frac{\partial\mathbf{d}_{6,x}^{-}(\boldsymbol{\xi},\omega)}{\partial x}+\frac{C_{33}}{\zeta_z}\frac{\partial\mathbf{d}_{6,z}^{-}(\boldsymbol{\xi},\omega)}{\partial z}\right]\mathrm{d}x\mathrm{d}z,\end{aligned}\tag{B.9b}$$

$$\begin{aligned}\mathbf{A}_{15,x}^{i,j}=&-\frac{9}{8\Delta x(\zeta_x)^i\left|I_{i-1/2,j}^{\varepsilon}\right|}\iint_{I_{i-1/2,j}^{\varepsilon}}\left[\frac{C_{11}}{\zeta_x}\frac{\partial\mathbf{c}_{5,x}^{-}(\boldsymbol{\xi},\omega)}{\partial x}+\frac{C_{13}}{\zeta_z}\frac{\partial\mathbf{c}_{5,z}^{-}(\boldsymbol{\xi},\omega)}{\partial z}\right]\mathrm{d}x\mathrm{d}z\\&+\frac{1}{24\Delta x(\zeta_x)^i\left|I_{i-3/2,j}^{\varepsilon}\right|}\iint_{I_{i-3/2,j}^{\varepsilon}}\left[\frac{C_{11}}{\zeta_x}\frac{\partial\mathbf{c}_{6,x}^{(-1)-}(\boldsymbol{\xi},\omega)}{\partial x}+\frac{C_{13}}{\zeta_z}\frac{\partial\mathbf{c}_{6,z}^{(-1)-}(\boldsymbol{\xi},\omega)}{\partial z}\right]\mathrm{d}x\mathrm{d}z\\&+\frac{9}{8\Delta z(\zeta_z)^j\left|I_{i,j+1/2}^{\varepsilon}\right|}\iint_{I_{i,j+1/2}^{\varepsilon}}\left[\frac{C_{55}}{\zeta_z}\frac{\partial\mathbf{d}_{4,x}^{+}(\boldsymbol{\xi},\omega)}{\partial z}+\frac{C_{55}}{\zeta_x}\frac{\partial\mathbf{d}_{4,z}^{+}(\boldsymbol{\xi},\omega)}{\partial x}\right]\mathrm{d}x\mathrm{d}z\\&-\frac{1}{24\Delta z(\zeta_z)^j\left|I_{i,j+3/2}^{\varepsilon}\right|}\iint_{I_{i,j+3/2}^{\varepsilon}}\left[\frac{C_{55}}{\zeta_z}\frac{\partial\mathbf{d}_{1,x}^{(1)+}(\boldsymbol{\xi},\omega)}{\partial z}+\frac{C_{55}}{\zeta_x}\frac{\partial\mathbf{d}_{1,z}^{(1)+}(\boldsymbol{\xi},\omega)}{\partial x}\right]\mathrm{d}x\mathrm{d}z,\end{aligned}\tag{B.10a}$$

$$
\begin{aligned}
\mathbf{A}^{i,j}_{15,z} = & -\frac{9}{8\Delta x(\zeta_x)^i\left|I^{\varepsilon}_{i-1/2,j}\right|}\iint_{I^{\varepsilon}_{i-1/2,j}}\left[\frac{C_{55}}{\zeta_z}\frac{\partial \mathbf{c}^{-}_{5,x}(\boldsymbol{\xi},\omega)}{\partial z}+\frac{C_{55}}{\zeta_x}\frac{\partial \mathbf{c}^{-}_{5,z}(\boldsymbol{\xi},\omega)}{\partial x}\right]\mathrm{d}x\mathrm{d}z \\
& +\frac{1}{24\Delta x(\zeta_x)^i\left|I^{\varepsilon}_{i-3/2,j}\right|}\iint_{I^{\varepsilon}_{i-3/2,j}}\left[\frac{C_{55}}{\zeta_z}\frac{\partial \mathbf{c}^{(-1)-}_{6,x}(\boldsymbol{\xi},\omega)}{\partial z}+\frac{C_{55}}{\zeta_x}\frac{\partial \mathbf{c}^{(-1)-}_{6,x}(\boldsymbol{\xi},\omega)}{\partial x}\right]\mathrm{d}x\mathrm{d}z \\
& +\frac{9}{8\Delta z(\zeta_z)^j\left|I^{\varepsilon}_{i,j+1/2}\right|}\iint_{I^{\varepsilon}_{i,j+1/2}}\left[\frac{C_{13}}{\zeta_x}\frac{\partial \mathbf{d}^{+}_{4,x}(\boldsymbol{\xi},\omega)}{\partial x}+\frac{C_{33}}{\zeta_z}\frac{\partial \mathbf{d}^{+}_{4,z}(\boldsymbol{\xi},\omega)}{\partial z}\right]\mathrm{d}x\mathrm{d}z \\
& -\frac{1}{24\Delta z(\zeta_z)^j\left|I^{\varepsilon}_{i,j+3/2}\right|}\iint_{I^{\varepsilon}_{i,j+3/2}}\left[\frac{C_{13}}{\zeta_x}\frac{\partial \mathbf{d}^{(1)+}_{1,x}(\boldsymbol{\xi},\omega)}{\partial x}+\frac{C_{33}}{\zeta_z}\frac{\partial \mathbf{d}^{(1)+}_{1,z}(\boldsymbol{\xi},\omega)}{\partial z}\right]\mathrm{d}x\mathrm{d}z,
\end{aligned}
\tag{B.10b}
$$

$$
\begin{aligned}
\mathbf{A}^{i,j}_{16,x} = & \frac{9}{8\Delta x(\zeta_x)^i\left|I^{\varepsilon}_{i+1/2,j}\right|}\iint_{I^{\varepsilon}_{i+1/2,j}}\left[\frac{C_{11}}{\zeta_x}\frac{\partial \mathbf{c}^{+}_{5,x}(\boldsymbol{\xi},\omega)}{\partial x}+\frac{C_{13}}{\zeta_z}\frac{\partial \mathbf{c}^{+}_{5,z}(\boldsymbol{\xi},\omega)}{\partial z}\right]\mathrm{d}x\mathrm{d}z \\
& -\frac{9}{8\Delta x(\zeta_x)^i\left|I^{\varepsilon}_{i-1/2,j}\right|}\iint_{I^{\varepsilon}_{i-1/2,j}}\left[\frac{C_{11}}{\zeta_x}\frac{\partial \mathbf{c}^{-}_{6,x}(\boldsymbol{\xi},\omega)}{\partial x}+\frac{C_{13}}{\zeta_z}\frac{\partial \mathbf{c}^{-}_{6,z}(\boldsymbol{\xi},\omega)}{\partial z}\right]\mathrm{d}x\mathrm{d}z \\
& +\frac{9}{8\Delta z(\zeta_z)^j\left|I^{\varepsilon}_{i,j+1/2}\right|}\iint_{I^{\varepsilon}_{i,j+1/2}}\left[\frac{C_{55}}{\zeta_z}\frac{\partial \mathbf{d}^{+}_{5,x}(\boldsymbol{\xi},\omega)}{\partial z}+\frac{C_{55}}{\zeta_x}\frac{\partial \mathbf{d}^{+}_{5,z}(\boldsymbol{\xi},\omega)}{\partial x}\right]\mathrm{d}x\mathrm{d}z \\
& -\frac{1}{24\Delta z(\zeta_z)^j\left|I^{\varepsilon}_{i,j+3/2}\right|}\iint_{I^{\varepsilon}_{i,j+3/2}}\left[\frac{C_{55}}{\zeta_z}\frac{\partial \mathbf{d}^{(1)+}_{2,x}(\boldsymbol{\xi},\omega)}{\partial z}+\frac{C_{55}}{\zeta_x}\frac{\partial \mathbf{d}^{(1)+}_{2,x}(\boldsymbol{\xi},\omega)}{\partial x}\right]\mathrm{d}x\mathrm{d}z,
\end{aligned}
\tag{B.11a}
$$

$$
\begin{aligned}
\mathbf{A}^{i,j}_{16,z} = & \frac{9}{8\Delta x(\zeta_x)^i\left|I^{\varepsilon}_{i+1/2,j}\right|}\iint_{I^{\varepsilon}_{i+1/2,j}}\left[\frac{C_{55}}{\zeta_z}\frac{\partial \mathbf{c}^{+}_{5,x}(\boldsymbol{\xi},\omega)}{\partial z}+\frac{C_{55}}{\zeta_x}\frac{\partial \mathbf{c}^{+}_{5,z}(\boldsymbol{\xi},\omega)}{\partial x}\right]\mathrm{d}x\mathrm{d}z \\
& -\frac{9}{8\Delta x(\zeta_x)^i\left|I^{\varepsilon}_{i-1/2,j}\right|}\iint_{I^{\varepsilon}_{i-1/2,j}}\left[\frac{C_{55}}{\zeta_z}\frac{\partial \mathbf{c}^{-}_{6,x}(\boldsymbol{\xi},\omega)}{\partial z}+\frac{C_{55}}{\zeta_x}\frac{\partial \mathbf{c}^{-}_{6,z}(\boldsymbol{\xi},\omega)}{\partial x}\right]\mathrm{d}x\mathrm{d}z \\
& +\frac{9}{8\Delta z(\zeta_z)^j\left|I^{\varepsilon}_{i,j+1/2}\right|}\iint_{I^{\varepsilon}_{i,j+1/2}}\left[\frac{C_{13}}{\zeta_x}\frac{\partial \mathbf{d}^{+}_{5,x}(\boldsymbol{\xi},\omega)}{\partial x}+\frac{C_{33}}{\zeta_z}\frac{\partial \mathbf{d}^{+}_{5,z}(\boldsymbol{\xi},\omega)}{\partial z}\right]\mathrm{d}x\mathrm{d}z \\
& -\frac{1}{24\Delta z(\zeta_z)^j\left|I^{\varepsilon}_{i,j+3/2}\right|}\iint_{I^{\varepsilon}_{i,j+3/2}}\left[\frac{C_{13}}{\zeta_x}\frac{\partial \mathbf{d}^{(1)+}_{2,x}(\boldsymbol{\xi},\omega)}{\partial x}+\frac{C_{33}}{\zeta_z}\frac{\partial \mathbf{d}^{(1)+}_{2,x}(\boldsymbol{\xi},\omega)}{\partial z}\right]\mathrm{d}x\mathrm{d}z,
\end{aligned}
\tag{B.11b}
$$

$$
\begin{aligned}
\mathbf{A}^{i,j}_{17,x} = & \frac{9}{8\Delta x(\zeta_x)^i\left|I^{\varepsilon}_{i+1/2,j}\right|}\iint_{I^{\varepsilon}_{i+1/2,j}}\left[\frac{C_{11}}{\zeta_x}\frac{\partial \mathbf{c}^{+}_{6,x}(\boldsymbol{\xi},\omega)}{\partial x}+\frac{C_{13}}{\zeta_z}\frac{\partial \mathbf{c}^{+}_{6,z}(\boldsymbol{\xi},\omega)}{\partial z}\right]\mathrm{d}x\mathrm{d}z \\
& -\frac{1}{24\Delta x(\zeta_x)^i\left|I^{\varepsilon}_{i+3/2,j}\right|}\iint_{I^{\varepsilon}_{i+3/2,j}}\left[\frac{C_{11}}{\zeta_x}\frac{\partial \mathbf{c}^{(1)+}_{5,x}(\boldsymbol{\xi},\omega)}{\partial x}+\frac{C_{13}}{\zeta_z}\frac{\partial \mathbf{c}^{(1)+}_{5,z}(\boldsymbol{\xi},\omega)}{\partial z}\right]\mathrm{d}x\mathrm{d}z \\
& +\frac{9}{8\Delta z(\zeta_z)^j\left|I^{\varepsilon}_{i,j+1/2}\right|}\iint_{I^{\varepsilon}_{i,j+1/2}}\left[\frac{C_{55}}{\zeta_z}\frac{\partial \mathbf{d}^{+}_{6,x}(\boldsymbol{\xi},\omega)}{\partial z}+\frac{C_{55}}{\zeta_x}\frac{\partial \mathbf{d}^{+}_{6,z}(\boldsymbol{\xi},\omega)}{\partial x}\right]\mathrm{d}x\mathrm{d}z \\
& -\frac{1}{24\Delta z(\zeta_z)^j\left|I^{\varepsilon}_{i,j+3/2}\right|}\iint_{I^{\varepsilon}_{i,j+3/2}}\left[\frac{C_{55}}{\zeta_z}\frac{\partial \mathbf{d}^{(1)+}_{3,x}(\boldsymbol{\xi},\omega)}{\partial z}+\frac{C_{55}}{\zeta_x}\frac{\partial \mathbf{d}^{(1)+}_{3,z}(\boldsymbol{\xi},\omega)}{\partial x}\right]\mathrm{d}x\mathrm{d}z,
\end{aligned}
\tag{B.12a}
$$

$$
\begin{aligned}
\mathbf{A}^{i,j}_{17,z} = & \frac{9}{8\Delta x(\zeta_x)^i\left|I^{\varepsilon}_{i+1/2,j}\right|}\iint_{I^{\varepsilon}_{i+1/2,j}}\left[\frac{C_{55}}{\zeta_z}\frac{\partial \mathbf{c}^{+}_{6,x}(\boldsymbol{\xi},\omega)}{\partial z}+\frac{C_{55}}{\zeta_x}\frac{\partial \mathbf{c}^{+}_{6,z}(\boldsymbol{\xi},\omega)}{\partial x}\right]\mathrm{d}x\mathrm{d}z \\
& -\frac{1}{24\Delta x(\zeta_x)^i\left|I^{\varepsilon}_{i+3/2,j}\right|}\iint_{I^{\varepsilon}_{i+3/2,j}}\left[\frac{C_{55}}{\zeta_z}\frac{\partial \mathbf{c}^{(1)+}_{5,x}(\boldsymbol{\xi},\omega)}{\partial z}+\frac{C_{55}}{\zeta_x}\frac{\partial \mathbf{c}^{(1)+}_{5,z}(\boldsymbol{\xi},\omega)}{\partial x}\right]\mathrm{d}x\mathrm{d}z \\
& +\frac{9}{8\Delta z(\zeta_z)^j\left|I^{\varepsilon}_{i,j+1/2}\right|}\iint_{I^{\varepsilon}_{i,j+1/2}}\left[\frac{C_{13}}{\zeta_x}\frac{\partial \mathbf{d}^{+}_{6,x}(\boldsymbol{\xi},\omega)}{\partial x}+\frac{C_{33}}{\zeta_z}\frac{\partial \mathbf{d}^{+}_{6,z}(\boldsymbol{\xi},\omega)}{\partial z}\right]\mathrm{d}x\mathrm{d}z \\
& -\frac{1}{24\Delta z(\zeta_z)^j\left|I^{\varepsilon}_{i,j+3/2}\right|}\iint_{I^{\varepsilon}_{i,j+3/2}}\left[\frac{C_{13}}{\zeta_x}\frac{\partial \mathbf{d}^{(1)+}_{3,x}(\boldsymbol{\xi},\omega)}{\partial x}+\frac{C_{33}}{\zeta_z}\frac{\partial \mathbf{d}^{(1)+}_{3,x}(\boldsymbol{\xi},\omega)}{\partial z}\right]\mathrm{d}x\mathrm{d}z,
\end{aligned}
\tag{B.12b}
$$

$$\mathbf{A}^{i,j}_{(n=8,13,18),x} = -\frac{1}{24\Delta x(\zeta_x)^i\left|I^{\varepsilon}_{i+3/2,j}\right|}\iint_{I^{\varepsilon}_{i+3/2,j}}\left[\frac{C_{11}}{\zeta_x}\frac{\partial \mathbf{c}^{(1)+}_{(2n-6)/5,x}(\boldsymbol{\xi},\omega)}{\partial x}+\frac{C_{13}}{\zeta_z}\frac{\partial \mathbf{c}^{(1)+}_{(2n-6)/5,z}(\boldsymbol{\xi},\omega)}{\partial z}\right]\mathrm{d}x\mathrm{d}z, \tag{B.13a}$$

$$\mathbf{A}^{i,j}_{(n=8,13,18),z} = -\frac{1}{24\Delta x(\zeta_x)^i\left|I^{\varepsilon}_{i+3/2,j}\right|}\iint_{I^{\varepsilon}_{i+3/2,j}}\left[\frac{C_{55}}{\zeta_z}\frac{\partial \mathbf{c}^{(1)+}_{(2n-6)/5,x}(\boldsymbol{\xi},\omega)}{\partial z}+\frac{C_{55}}{\zeta_x}\frac{\partial \mathbf{c}^{(1)+}_{(2n-6)/5,z}(\boldsymbol{\xi},\omega)}{\partial x}\right]\mathrm{d}x\mathrm{d}z, \tag{B.13b}$$

$$\mathbf{A}^{i,j}_{(n=19,20,21),x} = -\frac{1}{24\Delta z(\zeta_z)^j\left|I^{\varepsilon}_{i,j+3/2}\right|}\iint_{I^{\varepsilon}_{i,j+3/2}}\left[\frac{C_{55}}{\zeta_z}\frac{\partial \mathbf{d}^{(1)+}_{n-15,x}(\boldsymbol{\xi},\omega)}{\partial z}+\frac{C_{55}}{\zeta_x}\frac{\partial \mathbf{d}^{(1)+}_{n-15,z}(\boldsymbol{\xi},\omega)}{\partial x}\right]\mathrm{d}x\mathrm{d}z, \tag{B.14a}$$

$$\mathbf{A}^{i,j}_{(n=19,20,21),z} = -\frac{1}{24\Delta z(\zeta_z)^j\left|I^{\varepsilon}_{i,j+3/2}\right|}\iint_{I^{\varepsilon}_{i,j+3/2}}\left[\frac{C_{13}}{\zeta_x}\frac{\partial \mathbf{d}^{(1)+}_{n-15,x}(\boldsymbol{\xi},\omega)}{\partial x}+\frac{C_{33}}{\zeta_z}\frac{\partial \mathbf{d}^{(1)+}_{n-15,z}(\boldsymbol{\xi},\omega)}{\partial z}\right]\mathrm{d}x\mathrm{d}z, \tag{B.14b}$$

with

$$\mathbf{D}_x = \left(\omega^2\overline{D}_{i,j},0\right), \mathbf{D}_z = \left(0,\omega^2\overline{D}_{i,j}\right), \tag{B.15}$$

$$\zeta_{\alpha=x,z} = \begin{cases} 1+i\dfrac{a_0\omega_0(D_\alpha/L_{\mathrm{PML}})^2}{\omega}, & \text{inside PML,} \\ 1, & \text{outside PML,} \end{cases} \tag{B.16}$$

where $i=\sqrt{-1}$, a_0 is a constant, D_α denotes the distance from a point, which is indicated by the superscripts of $\zeta_{\alpha=x,z}$, to the boundary of the bounded computational domain in the α direction, L_{PML} denotes the PML width; Δx and Δz are the x- and z-direction sizes of coarse elements in $\mathrm{Q_H}$, respectively; $(\zeta_x)^i = \zeta_x(x_i) = \zeta_x(i\Delta x)$ and $(\zeta_z)^j = \zeta_z\left(z_j\right) = \zeta_z(j\Delta z)$ represent the PML damping values at the x-coordinate x_i in the x direction and the z-coordinate z_j in the z direction, respectively.

An example is presented to exemplify the finite-difference approximation of an integral term. For the integral term in Eq. (B.2a), its finite-difference approximation is

$$\begin{aligned}&\frac{1}{\left|I^{\varepsilon}_{i,j-3/2}\right|}\iint_{I^{\varepsilon}_{i,j-3/2}}\left[\frac{C_{55}}{\zeta_z}\frac{\partial \mathbf{d}^{(-1)-}_{n,x}(\boldsymbol{\xi},\omega)}{\partial z}+\frac{C_{55}}{\zeta_x}\frac{\partial \mathbf{d}^{(-1)-}_{n,z}(\boldsymbol{\xi},\omega)}{\partial x}\right]\mathrm{d}x\mathrm{d}z \\ &\approx \frac{1}{N^{\varepsilon}_x(N^{\varepsilon}_z-1)}\sum_{k=1}^{N^{\varepsilon}_x}\sum_{l=1}^{N^{\varepsilon}_z-1}\frac{(C_{55})^{i,j-3/2}_{k,l+1/2}\left[\mathbf{d}^{(-1)-}_{n,x}(\xi_k,\eta_{l+1},\omega)-\mathbf{d}^{(-1)-}_{n,x}(\xi_k,\eta_l,\omega)\right]}{\Delta\eta(\zeta_z)^{j-3/2}_{l+1/2}} \\ &+\frac{1}{(N^{\varepsilon}_x-1)N^{\varepsilon}_z}\sum_{k=1}^{N^{\varepsilon}_x-1}\sum_{l=1}^{N^{\varepsilon}_z}\frac{(C_{55})^{i,j-3/2}_{k+1/2,l}\left[\mathbf{d}^{(-1)-}_{n,z}(\xi_{k+1},\eta_l,\omega)-\mathbf{d}^{(-1)-}_{n,z}(\xi_k,\eta_l,\omega)\right]}{\Delta\xi(\zeta_x)^{i}_{k+1/2}},\end{aligned} \tag{B.17}$$

where $(\xi_k,\eta_l) = (k\Delta\xi, l\Delta\eta)$ is the discrete sampling point of the local Cartesian coordinate $\boldsymbol{\xi} = (\xi,\eta)$ in the ε-cells, $\xi_k = \xi_k(x) = x+\left[k-(1+N^{\varepsilon}_x)/2\right]\Delta\xi$, $\eta_l = \eta_l(z) = z+\left[l-(1+N^{\varepsilon}_z)/2\right]\Delta\eta$, and (x, z) refers to the center point of an ε-cell, $(x,z) = (x_i, z_{j-3/2})$, for instance; the superscripts and subscripts of C_{55} and $\zeta_{\alpha=x,z}$ provide their coordinates, $(C_{55})^{i,j-3/2}_{k,l+1/2} = C_{55}\left(\xi_k(x_i),\eta_{l+1/2}\left(z_{j-3/2}\right)\right)$ and $(\zeta_x)^i_{k+1/2} = \zeta_x\left(\xi_{k+1/2}(x_i)\right)$, for instance. The finite-difference approximations of other integral terms in Eq. (B.2)–(B.14) can be formulated similarly.

Appendix C. Discrete linear system of the macroscale problem

With the coefficient matrices in Appendix B, we assemble the impedance matrix $\tilde{\mathbf{A}}$ in Eq. (23). If we define the two column vectors in Eq. (23) as the following forms:

$$\tilde{\mathbf{U}} = \left(\mathbf{U}_{0,0},\cdots,\mathbf{U}_{N^{\mathrm{H}}_x-1,0},\cdots,\mathbf{U}_{0,N^{\mathrm{H}}_z-1},\cdots,\mathbf{U}_{N^{\mathrm{H}}_x-1,N^{\mathrm{H}}_z-1}\right)^{\mathrm{T}}, \tag{C.1}$$

$$\tilde{\mathbf{F}} = \left(\mathbf{F}_{0,0},\cdots,\mathbf{F}_{N^{\mathrm{H}}_x-1,0},\cdots,\mathbf{F}_{0,N^{\mathrm{H}}_z-1},\cdots,\mathbf{F}_{N^{\mathrm{H}}_x-1,N^{\mathrm{H}}_z-1}\right)^{\mathrm{T}}, \tag{C.2}$$

in which $\mathbf{U}_{i,j} = (U_{x,i,j}, U_{z,i,j})^{\mathrm{T}}$ and $\mathbf{F}_{i,j} = (F_{x,i,j}, F_{z,i,j})^{\mathrm{T}}$ with $i = 0,\cdots,N^{\mathrm{H}}_x-1$ and $j = 0,\cdots,N^{\mathrm{H}}_z-1$, the corresponding impedance matrix is

$$\tilde{\mathbf{A}} = \begin{pmatrix} \mathbf{M}_3^0 & \mathbf{M}_4^0 & \mathbf{M}_5^0 & 0 & 0 & 0 & 0 \\ \mathbf{M}_2^1 & \mathbf{M}_3^1 & \mathbf{M}_4^1 & \mathbf{M}_5^1 & 0 & 0 & 0 \\ \mathbf{M}_1^2 & \mathbf{M}_2^2 & \mathbf{M}_3^2 & \mathbf{M}_4^2 & \mathbf{M}_5^2 & 0 & 0 \\ 0 & \ddots & \ddots & \ddots & \ddots & \ddots & 0 \\ 0 & 0 & \mathbf{M}_1^{N_z^{\mathrm{H}}-3} & \mathbf{M}_2^{N_z^{\mathrm{H}}-3} & \mathbf{M}_3^{N_z^{\mathrm{H}}-3} & \mathbf{M}_4^{N_z^{\mathrm{H}}-3} & \mathbf{M}_5^{N_z^{\mathrm{H}}-3} \\ 0 & 0 & 0 & \mathbf{M}_1^{N_z^{\mathrm{H}}-2} & \mathbf{M}_2^{N_z^{\mathrm{H}}-2} & \mathbf{M}_3^{N_z^{\mathrm{H}}-2} & \mathbf{M}_4^{N_z^{\mathrm{H}}-2} \\ 0 & 0 & 0 & 0 & \mathbf{M}_1^{N_z^{\mathrm{H}}-1} & \mathbf{M}_2^{N_z^{\mathrm{H}}-1} & \mathbf{M}_3^{N_z^{\mathrm{H}}-1} \end{pmatrix}, \tag{C.3}$$

with

$$\mathbf{M}_1^j = \begin{pmatrix} \mathbf{A}_2^{0,j} & \mathbf{A}_3^{0,j} & 0 & 0 & 0 & 0 & 0 \\ \mathbf{A}_1^{1,j} & \mathbf{A}_2^{1,j} & \mathbf{A}_3^{1,j} & 0 & 0 & 0 & 0 \\ 0 & \mathbf{A}_1^{2,j} & \mathbf{A}_2^{2,j} & \mathbf{A}_3^{2,j} & 0 & 0 & 0 \\ 0 & 0 & \ddots & \ddots & \ddots & 0 & 0 \\ 0 & 0 & 0 & \mathbf{A}_1^{N_x^{\mathrm{H}}-3,j} & \mathbf{A}_2^{N_x^{\mathrm{H}}-3,j} & \mathbf{A}_3^{N_x^{\mathrm{H}}-3,j} & 0 \\ 0 & 0 & 0 & 0 & \mathbf{A}_1^{N_x^{\mathrm{H}}-2,j} & \mathbf{A}_2^{N_x^{\mathrm{H}}-2,j} & \mathbf{A}_3^{N_x^{\mathrm{H}}-2,j} \\ 0 & 0 & 0 & 0 & 0 & \mathbf{A}_1^{N_x^{\mathrm{H}}-1,j} & \mathbf{A}_2^{N_x^{\mathrm{H}}-1,j} \end{pmatrix}, \tag{C.4}$$

$$\mathbf{M}_2^j = \begin{pmatrix} \mathbf{A}_6^{0,j} & \mathbf{A}_7^{0,j} & \mathbf{A}_8^{0,j} & 0 & 0 & 0 & 0 \\ \mathbf{A}_5^{1,j} & \mathbf{A}_6^{1,j} & \mathbf{A}_7^{1,j} & \mathbf{A}_8^{1,j} & 0 & 0 & 0 \\ \mathbf{A}_4^{2,j} & \mathbf{A}_5^{2,j} & \mathbf{A}_6^{2,j} & \mathbf{A}_7^{2,j} & \mathbf{A}_8^{2,j} & 0 & 0 \\ 0 & \ddots & \ddots & \ddots & \ddots & \ddots & 0 \\ 0 & 0 & \mathbf{A}_4^{N_x^{\mathrm{H}}-3,j} & \mathbf{A}_5^{N_x^{\mathrm{H}}-3,j} & \mathbf{A}_6^{N_x^{\mathrm{H}}-3,j} & \mathbf{A}_7^{N_x^{\mathrm{H}}-3,j} & \mathbf{A}_8^{N_x^{\mathrm{H}}-3,j} \\ 0 & 0 & 0 & \mathbf{A}_4^{N_x^{\mathrm{H}}-2,j} & \mathbf{A}_5^{N_x^{\mathrm{H}}-2,j} & \mathbf{A}_6^{N_x^{\mathrm{H}}-2,j} & \mathbf{A}_7^{N_x^{\mathrm{H}}-2,j} \\ 0 & 0 & 0 & 0 & \mathbf{A}_4^{N_x^{\mathrm{H}}-1,j} & \mathbf{A}_5^{N_x^{\mathrm{H}}-1,j} & \mathbf{A}_6^{N_x^{\mathrm{H}}-1,j} \end{pmatrix}, \tag{C.5}$$

$$\mathbf{M}_3^j = \begin{pmatrix} \mathbf{A}_{11}^{0,j} & \mathbf{A}_{12}^{0,j} & \mathbf{A}_{13}^{0,j} & 0 & 0 & 0 & 0 \\ \mathbf{A}_{10}^{1,j} & \mathbf{A}_{11}^{1,j} & \mathbf{A}_{12}^{1,j} & \mathbf{A}_{13}^{1,j} & 0 & 0 & 0 \\ \mathbf{A}_9^{2,j} & \mathbf{A}_{10}^{2,j} & \mathbf{A}_{11}^{2,j} & \mathbf{A}_{12}^{2,j} & \mathbf{A}_{13}^{2,j} & 0 & 0 \\ 0 & \ddots & \ddots & \ddots & \ddots & \ddots & 0 \\ 0 & 0 & \mathbf{A}_9^{N_x^{\mathrm{H}}-3,j} & \mathbf{A}_{10}^{N_x^{\mathrm{H}}-3,j} & \mathbf{A}_{11}^{N_x^{\mathrm{H}}-3,j} & \mathbf{A}_{12}^{N_x^{\mathrm{H}}-3,j} & \mathbf{A}_{13}^{N_x^{\mathrm{H}}-3,j} \\ 0 & 0 & 0 & \mathbf{A}_9^{N_x^{\mathrm{H}}-2,j} & \mathbf{A}_{10}^{N_x^{\mathrm{H}}-2,j} & \mathbf{A}_{11}^{N_x^{\mathrm{H}}-2,j} & \mathbf{A}_{12}^{N_x^{\mathrm{H}}-2,j} \\ 0 & 0 & 0 & 0 & \mathbf{A}_9^{N_x^{\mathrm{H}}-1,j} & \mathbf{A}_{10}^{N_x^{\mathrm{H}}-1,j} & \mathbf{A}_{11}^{N_x^{\mathrm{H}}-1,j} \end{pmatrix}, \tag{C.6}$$

$$\mathbf{M}_4^j = \begin{pmatrix} \mathbf{A}_{16}^{0,j} & \mathbf{A}_{17}^{0,j} & \mathbf{A}_{18}^{0,j} & 0 & 0 & 0 & 0 \\ \mathbf{A}_{15}^{1,j} & \mathbf{A}_{16}^{1,j} & \mathbf{A}_{17}^{1,j} & \mathbf{A}_{18}^{1,j} & 0 & 0 & 0 \\ \mathbf{A}_{14}^{2,j} & \mathbf{A}_{15}^{2,j} & \mathbf{A}_{16}^{2,j} & \mathbf{A}_{17}^{2,j} & \mathbf{A}_{18}^{2,j} & 0 & 0 \\ 0 & \ddots & \ddots & \ddots & \ddots & \ddots & 0 \\ 0 & 0 & \mathbf{A}_{14}^{N_x^{\mathrm{H}}-3,j} & \mathbf{A}_{15}^{N_x^{\mathrm{H}}-3,j} & \mathbf{A}_{16}^{N_x^{\mathrm{H}}-3,j} & \mathbf{A}_{17}^{N_x^{\mathrm{H}}-3,j} & \mathbf{A}_{18}^{N_x^{\mathrm{H}}-3,j} \\ 0 & 0 & 0 & \mathbf{A}_{14}^{N_x^{\mathrm{H}}-2,j} & \mathbf{A}_{15}^{N_x^{\mathrm{H}}-2,j} & \mathbf{A}_{16}^{N_x^{\mathrm{H}}-2,j} & \mathbf{A}_{17}^{N_x^{\mathrm{H}}-2,j} \\ 0 & 0 & 0 & 0 & \mathbf{A}_{14}^{N_x^{\mathrm{H}}-1,j} & \mathbf{A}_{15}^{N_x^{\mathrm{H}}-1,j} & \mathbf{A}_{16}^{N_x^{\mathrm{H}}-1,j} \end{pmatrix}, \tag{C.7}$$

$$\mathbf{M}_5^j = \begin{pmatrix} \mathbf{A}_{20}^{0,j} & \mathbf{A}_{21}^{0,j} & 0 & 0 & 0 & 0 & 0 \\ \mathbf{A}_{19}^{1,j} & \mathbf{A}_{20}^{1,j} & \mathbf{A}_{21}^{1,j} & 0 & 0 & 0 & 0 \\ 0 & \mathbf{A}_{19}^{2,j} & \mathbf{A}_{20}^{2,j} & \mathbf{A}_{21}^{2,j} & 0 & 0 & 0 \\ 0 & 0 & \ddots & \ddots & \ddots & 0 & 0 \\ 0 & 0 & 0 & \mathbf{A}_{19}^{N_x^{\mathrm{H}}-3,j} & \mathbf{A}_{20}^{N_x^{\mathrm{H}}-3,j} & \mathbf{A}_{21}^{N_x^{\mathrm{H}}-3,j} & 0 \\ 0 & 0 & 0 & 0 & \mathbf{A}_{19}^{N_x^{\mathrm{H}}-2,j} & \mathbf{A}_{20}^{N_x^{\mathrm{H}}-2,j} & \mathbf{A}_{21}^{N_x^{\mathrm{H}}-2,j} \\ 0 & 0 & 0 & 0 & 0 & \mathbf{A}_{19}^{N_x^{\mathrm{H}}-1,j} & \mathbf{A}_{20}^{N_x^{\mathrm{H}}-1,j} \end{pmatrix}. \tag{C.8}$$

References

Abdulle, A., E, W., 2003. Finite difference heterogeneous multi-scale method for homogenization problems. J. Comput. Phys. 191 (1), 18–39. https://doi.org/10.1016/S0021-9991(03)00303-6.

Amestoy, P., Ashcraft, C., Boiteau, O., Buttari, A., L'Excellent, J.Y., Weisbecker, C., 2015. Improving multifrontal methods by means of block low-rank representation. SIAM J. Sci. Comput. 37 (3), A1451–A1474. https://doi.org/10.1137/120903476.

Arjmand, D., Runborg, O., 2017. Estimates for the upscaling error in heterogeneous multiscale methods for wave propagation problems in locally periodic media. Multiscale Model. Simul. 15 (2), 948–976. https://doi.org/10.1137/16M1074436.

Bohlen, T., 2002. Parallel 3-D viscoelastic finite difference seismic modelling. Comput. Geosci. 28 (8), 887–899. https://doi.org/10.1016/S0098-3004(02)00006-7.

Capdeville, Y., Marigo, J.J., 2007. Second order homogenization of the elastic wave equation for non-periodic layered media. Geophys. J. Int. 170 (2), 823–838. https://doi.org/10.1111/j.1365-246X.2007.03462.x.

Chen, Z., 2009. On the heterogeneous multiscale method with various macroscopic solvers. Nonlin. Analy. 71 (7–8), 3267–3282. https://doi.org/10.1016/j.na.2009.01.229.

Chen, J.B., Cao, J., 2016. Modeling of frequency-domain elastic-wave equation with an average-derivative optimal method. Geophysics 81 (6), T339–T356. https://doi.org/10.1190/GEO2016-0041.1.

Chen, F., Ren, L., 2008. Application of the finite difference heterogeneous multiscale method to the Richards' equation. Water Resour. Res. 44, W07413. https://doi.org/10.1029/2007WR006275.

Chen, K., Liu, L., Xu, L.N., Hu, F., Yang, Y., Zuo, J.H., Zhang, L.L., Zhao, Y., 2024. Linearized waveform inversion for vertical transversely isotropic elastic media: methodology and multi-parameter crosstalk analysis. Pet. Sci. 21 (1), 252–271. https://doi.org/10.1016/j.petsci.2024.01.002.

E, W., Engquist, B., 2003. The heterogeneous multiscale methods. Commun. Math. Sci. 1 (1), 87–132. https://doi.org/10.4310/CMS.2003.v1.n1.a8.

Efendiev, Y., Galvis, J., Hou, T.Y., 2013. Generalized multiscale finite element methods (GMsFEM). J. Comput. Phys. 251 (22), 116–135. https://doi.org/10.1016/j.jcp.2013.04.045.

El Kacimi, A., Laghrouche, O., 2009. Numerical modelling of elastic wave scattering in frequency domain by the partition of unity finite element method. Int. J. Numer. Methods Eng. 77 (12), 1646–1669. https://doi.org/10.1002/nme.2471.

Engquist, B., Ying, L., 2011. Sweeping preconditioner for the Helmholtz equation: hierarchical matrix representation. Commun. Pure Appl. Math. 64 (5), 697–735. https://doi.org/10.1002/cpa.20358.

Engquist, B., Holst, H., Runborg, O., 2011. Multi-scale methods for wave propagation in heterogeneous media. Commun. Math. Sci. 9 (1), 33–56. https://doi.org/10.4310/CMS.2011.v9.n1.a2.

Erlangga, Y.A., Vuik, C., Oosterlee, C.W., 2004. On a class of preconditioners for the Helmholtz equation. Appl. Numer. Math. 50 (4), 409–425. https://doi.org/10.1016/j.apnum.2004.01.009.

Erlangga, Y.A., Oosterlee, C.W., Vuik, C., 2006. A novel multigrid based preconditioner for heterogeneous Helmholtz problems. SIAM J. Sci. Comput. 27 (4), 1471–1492. https://doi.org/10.1137/040615195.

Fan, N., Zhao, L.F., Xie, X.B., Yao, Z.X., 2018. A discontinuous-grid finite-difference scheme for frequency-domain 2D scalar wave modeling. Geophysics 83 (4), T235–T244. https://doi.org/10.1190/geo2017-0535.1.

Fu, S., Gao, K., 2017. A fast solver for the Helmholtz equation based on the generalized multiscale finite-element method. Geophys. J. Int. 211 (2), 797–813. https://doi.org/10.1093/gji/ggx343.

Fu, S., Gibson, Jr., R.L., Chung, E.T., 2019. An efficient high-order multiscale finite element method for frequency-domain elastic wave modeling. Comput. Geosci. 23 (5), 997–1010. https://doi.org/10.1007/s10596-019-09865-0.

Gao, K., Chung, E.T., Gibson, Jr., R.L., Fu, S., Efendiev, Y., 2015. A numerical homogenization method for heterogeneous, anisotropic elastic media based on multiscale theory. Geophysics 80 (4), D385–D401. https://doi.org/10.1190/geo2014-0363.1.

Gao, K., Fu, S., Chung, E.T., 2018. An efficient multiscale finite-element method for frequency-domain seismic wave propagation. Bull. Seismol. Soc. Am. 108 (2), 966–982. https://doi.org/10.1785/0120170268.

Gosselin-Cliche, B., Giroux, B., 2014. 3D frequency-domain finite-difference viscoelastic-wave modeling using weighted average 27-point operators with optimal coefficients. Geophysics 79 (3), T169–T188. https://doi.org/10.1190/GEO2013-0368.1.

He, X.J., Li, J.S., Huang, X.Y., Zhou, Y.J., 2023. Solving elastic wave equations in 2D transversely isotropic media by a weighted Runge-Kutta discontinuous Galerkin method. Pet. Sci. 20 (2), 827–839. https://doi.org/10.1016/j.petsci.2022.10.007.

Hou, T.Y., Wu, X.H., 1997. A multiscale finite element method for elliptic problems in composite materials and porous media. J. Comput. Phys. 134 (1), 169–189. https://doi.org/10.1006/jcph.1997.5682.

Hong, T.K., Kennett, B.L.N., 2003. Scattering attenuation of 2D elastic waves: Theory and numerical modeling using a wavelet-based method. Bull. Seismol. Soc. Am. 93 (2), 922–938. https://doi.org/10.1785/0120020059.

Hustedt, B., Operto, S., Virieux, J., 2004. Mixed-grid and staggered-grid finite-difference methods for frequency-domain acoustic wave modelling. Geophys. J. Int. 157 (3), 1269–1296. https://doi.org/10.1111/j.1365-246X.2004.02289.x.

Jiang, W., Chen, X., Jiang, S., Zhang, J., 2021. Multiscale finite-difference method for frequency-domain acoustic wave modeling. Geophysics 86 (4), T193–T210. https://doi.org/10.1190/geo2020-0517.1.

Jiang, W., Chen, X., Lv, B., Jiang, S., 2022. An accurate and efficient multiscale finite-difference frequency-domain method for the scalar Helmholtz equation. Geophysics 87 (1), T43–T60. https://doi.org/10.1190/geo2021-0217.1.

Klimeš, L., 2002. Correlation functions of random media. Pure Appl. Geophys. 159 (7–8), 1811–1831. https://doi.org/10.1007/s00024-002-8710-2.

Köhn, D., Hellwig, O., De Nil, D., Rabbel, W., 2015. Waveform inversion in triclinic anisotropic media—A resolution study. Geophys. J. Int. 201, 1642–1656. https://doi.org/10.1093/gji/ggv097.

Levander, A.R., 1988. Fourth-order finite-difference P-SV seismograms. Geophysics 53 (11), 1425–1436. https://doi.org/10.1190/1.1442422.

Li, X.S., 2005. An overview of SuperLU: Algorithms, implementation, and user interface. ACM Trans. Math Software 31 (3), 302–325. https://doi.org/10.1145/1089014.1089017.

Li, Y., Métivier, L., Brossier, R., Han, B., Virieux, J., 2015. 2D and 3D frequency-domain elastic wave modeling in complex media with a parallel iterative solver. Geophysics 80 (3), T101–T118. https://doi.org/10.1190/GEO2014-0480.1.

Mavko, G., Mukerji, T., Dvorkin, J., 2009. In: The Rock Physics Handbook, third ed. Cambridge University Press, Cambridge.

Min, D.J., Shin, C., Kwon, B.D., Chung, S., 2000. Improved frequency-domain elastic wave modeling using weighted-averaging difference operators. Geophysics 65 (3), 884–895. https://doi.org/10.1190/1.1444785.

Poulson, J., Engquist, B., Li, S., Ying, L., 2013. A parallel sweeping preconditioner for heterogeneous 3D Helmholtz equations. SIAM J. Sci. Comput. 35 (3), C194–C212. https://doi.org/10.1137/120871985.

Pratt, R.G., 1990. Frequency-domain elastic wave modeling by finite differences: A tool for crosshole seismic imaging. Geophysics 55 (5), 626–632. https://doi.org/10.1190/1.1442874.

Sanderson, C., Curtin, R., 2016. Armadillo: A template-based C++ library for linear algebra. J. Open Source Softw. 1 (2), 26. https://doi.org/10.21105/joss.00026.

Štekl, I., Pratt, R.G., 1998. Accurate viscoelastic modeling by frequency-domain finite differences using rotated operators. Geophysics 63 (5), 1779–1794. https://doi.org/10.1190/1.1444472.

Thompson, L.L., Pinsky, P.M., 1995. A Galerkin least-squares finite element method for the two-dimensional Helmholtz equation. Int. J. Numer. Methods Eng. 38 (3), 371–397. https://doi.org/10.1002/nme.1620380303.

Wang, Y., 2015. Frequencies of the Ricker wavelet. Geophysics 80 (2), A31–A37. https://doi.org/10.1190/GEO2014-0441.1.

Wang, S., de Hoop, M.V., Xia, J., 2010. Acoustic inverse scattering via Helmholtz operator factorization and optimization. J. Comput. Phys. 229 (22), 8445–8462. https://doi.org/10.1016/j.jcp.2010.07.027.

Wang, S., de Hoop, M.V., Xia, J., 2011. On 3D modeling of seismic wave propagation via a structured parallel multifrontal direct Helmholtz solver. Geophys. Prospect. 59 (5), 857–873. https://doi.org/10.1111/j.1365-2478.2011.00982.x.

Wang, S., Xia, J., de Hoop, M.V., Li, X.S., 2012. Massively parallel structured direct solver for equations describing time-harmonic qP-polarized waves in TTI media. Geophysics 77 (3), T69–T82. https://doi.org/10.1190/GEO2011-0163.1.

Wu, H., Sun, C., Deng, X., 2023. Seismic migration in viscoacoustic vertical transversely isotropic media using a pure qP wave equation. Geophys. Prospect. 71, 539–554. https://doi.org/10.1111/1365-2478.13328.

Xia, J., Chandrasekaran, S., Gu, M., Li, X.S., 2010. Fast algorithms for hierarchically semiseparable matrices. Numer. Lin. Algebra Appl. 17 (6), 953–976. https://doi.org/10.1002/nla.691.

Xu, J.Y., Liu, Y., 2024. A stable staggered-grid finite-difference scheme for acoustic modeling beyond conventional stability limit. Pet. Sci. 21 (1), 182–194. https://doi.org/10.1016/j.petsci.2023.09.009.

Yang, Q., Mao, W., 2017. Simulation of seismic wave propagation in 2-D poroelastic media using weighted-averaging finite difference stencils in the frequency-space domain. Geophys. J. Int. 208 (1), 148–161. https://doi.org/10.1093/gji/ggw380.

Zeng, Y.Q., He, J.Q., Liu, Q.H., 2001. The application of the perfectly matched layer in numerical modeling of wave propagation in poroelastic media. Geophysics 66 (4), 1258–1266. https://doi.org/10.1190/1.1487073.

Zhang, H.W., Wu, J.K., Fu, Z.D., 2010a. Extended multiscale finite element method for mechanical analysis of periodic lattice truss materials. Int. J. Multiscale Comput. Eng. 8 (6), 597–613. https://doi.org/10.1615/IntJMultCompEng.v8.i6.40.

Zhang, H.W., Wu, J.K., Lü, J., Fu, Z.D., 2010b. Extended multiscale finite element method for mechanical analysis of heterogeneous materials. Acta Mech. Sin. 26 (6), 899–920. https://doi.org/10.1007/s10409-010-0393-9.

Zhao, J., Huang, X., Liu, W., Zhao, W., Song, J., Xiong, B., Wang, S., 2017. 2.5-D frequency-domain viscoelastic wave modelling using finite-element method. Geophys. J. Int. 211 (1), 164–187. https://doi.org/10.1093/gji/ggx273.

Zhou, X.Y., Chang, X., Wang, Y.B., Wen, X.T., You, J.C., Sun, C., 2022. Non-artifact vector P- and S-wave separation for elastic reverse time migration. Pet. Sci. 19 (6), 2695–2710. https://doi.org/10.1016/j.petsci.2022.08.006.